Title
Numerical Analysis of Slender Vortex Motion

Author
Zhou, H.

Publication Date
1996-02-01

LBL-38265
UC-405

Lawrence Berkeley Laboratory
UNIVERSITY OF CALIFORNIA

Physics Division

Mathematics Department

Numerical Analysis of Slender Vortex Motion

H. Zhou
(Ph.D. Thesis)

February 1996

Prepared for the U.S. Department of Energy under Contract Number DE-AC03-76SF00098

DISCLAIMER

LBL-38265

NUMERICAL ANALYSIS OF SLENDER VORTEX MOTION *

Hong Zhou

Department of Mathematics
and
Lawrence Berkeley National Laboratory
University of California
Berkeley, CA 94720, USA

Ph.D. Thesis

February 1996

* This work was supported in part by the Applied Mathematical Sciences subprogram of the Office of Energy Research, U.S. Department of Energy, under Contract Number DE-AC03-76SF00098.

Numerical Analysis of Slender Vortex Motion

by

Hong Zhou

Abstract

Numerical Analysis of Slender Vortex Motion

by

Hong Zhou
Doctor of Philosophy in Applied Mathematics

University of California at Berkeley

Professor Alexandre J. Chorin, Chair

Several numerical methods for slender vortex motion (the local induction equation, the Klein-Majda equation, and the Klein-Knio equation) are compared on the specific example of sideband instability of Kelvin waves on a vortex. Numerical experiments on this model problem indicate that all these methods yield qualitatively similar behavior, and this behavior is different from the behavior of a non-slender vortex with variable cross-section. It is found that the boundaries between stable, recurrent, and chaotic regimes in the parameter space of the model problem depend on the method used. The boundaries of these domains in the parameter space for the Klein-Majda equation and for the Klein-Knio equation are closely related to the core size. When the core size is large enough, the Klein-Majda equation always exhibits stable solutions for our model problem.

Various conclusions are drawn; in particular, the behavior of turbulent vortices cannot be captured by these local approximations, and probably cannot be captured by any slender vortex model with constant vortex cross-section. Speculations about the differences between classical and superfluid hydrodynamics are also offered.

Acknowledgements

I wish to thank Professor Alexandre Chorin for his encouragement and help during my years as a graduate student at UC Berkeley. I am also grateful to Professor James Sethian and Professor Phillip Colella for taking the time to read this thesis.

Many thanks to all members of the mathematics and numerical analysis group at LBNL for friendly help.

Contents

List of Figures

Chapter 1

Introduction

Fluid vorticity is often concentrated in small regions. The special case where vorticity is concentrated on a single slender filament is of great importance in many problems (e.g. turbulence, superfluidity). The study of the motion of slender vortices has received a lot of attention. The local induction equation [9], the Klein-Majda equation [59], and the Klein-Knio equation [58] are three different approximations for the motion of slender vortices. The comparison of these methods and the study of differences between the results and what we expect in turbulence theory are the main goals of this thesis.

The thesis is organized as follows: Chapter 2 gives a brief introduction to vortex dynamics, to the equilibrium theory for vortex system, and to superfluid vortices. Chapter 3 presents equations of motion for slender vortices, namely, the self-induction equation, the Klein-Majda equation and the Klein-Knio equation. Conservation laws for special periodic boundary conditions are discussed. In Chapter 4 a model problem which comes from the theory of vortex wave motion in superfluid helium is introduced. Following the work of Klein and Majda, linear stability analysis is performed for both the self-induction equation and the Klein-Majda equation. The numerical methods for solving the self-induction equation, the Klein-Majda equation and the Klein-Knio equation are presented in Chapter 5, as well as the numerical results for the model problem. The application of the standard vortex method to a vortex filament with thicker core is discussed in Chapter 6. Finally, Chapter 7 contains conclusions and suggestions for future work. The main conclusion is that the three approximate methods yield qualitatively similar results for the motion of a single thin vortex filament, and that these results are at sharp variance from what we expect for a thicker vortex with variable cross-section. Speculations about the significance of these

results for turbulence theory and for the dynamics of superfluid vortices are offered in a concluding section. In particular, the fact that superfluid vortices are extremely slender may be more important in accounting for their non-classical dynamics than the fact that they are quantized.

Chapter 2

Vortices, Thick And Thin

We begin with a brief overview of vortex dynamics. We focus on inviscid incompressible fluids and those aspects of fluid motion which are primarily controlled by the vorticity, and introduce some basic notions (circulation, vortex tube, vortex filament, etc.) and equations (the Euler equations in different forms, the Biot-Savart law, the Lamb integral, etc.). The equilibrium statistics of classical vortices are quickly reviewed. The discussion of the equilibrium theory is restricted to a vortex system consisting of a single vortex filament. The main point is that vortex stretching is closely related to temperature. We then take a look at some important aspects of superfluid vortices: the two-fluid model, the quantization of superfluid circulation and Hall-Vinen friction. Finally, we highlight the differences between classical and superfluid vortices.

2.1 Euler Equations

Consider unbounded, inviscid, incompressible flows. In the absence of external force, the motion of such fluid with unit density is described by the Euler equations:

$$\frac{D\mathbf{u}}{Dt} = -\nabla \mathrm{p} \tag{2.1}$$

$$\nabla \cdot \mathbf{u} = 0 \tag{2.2}$$

where $\mathbf{u}(\mathbf{x}, t)$ is the velocity, $\mathbf{x} = (x_1, x_2, x_3)$ is the position, p is the pressure, $\nabla = (\frac{\partial}{\partial x_1}, \frac{\partial}{\partial x_2}, \frac{\partial}{\partial x_3})$ is the differentiation vector, t is the time, and $\frac{D}{Dt} \equiv \partial_t + \mathbf{u} \cdot \nabla$ is the material derivative.

The curl of the velocity field,

$$\omega = \nabla \times \mathbf{u} \tag{2.3}$$

is the vorticity. The Euler equations can be written in terms of the vorticity by taking the curl of (2.1) and can be reduced to

$$\frac{D\omega}{Dt} = (\omega \cdot \nabla)\mathbf{u}. \tag{2.4}$$

Let C be a smooth closed curve immersed in the fluid. The circulation Γ along C is

$$\Gamma = \int_C \mathbf{u}(\mathbf{x}, t) \cdot d\mathbf{l}. \tag{2.5}$$

The quantity (2.5) is invariant in time [35]. This is Kelvin's circulation theorem, or the law of conservation of circulation. If S is a surface that spans C, then by Stokes' theorem

$$\Gamma = \int_S \omega \cdot d\mathbf{s} \tag{2.6}$$

So the vorticity can be thought of as the circulation per area.

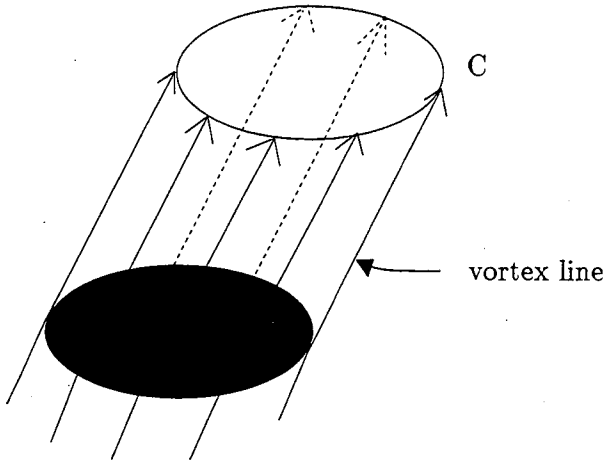

Figure 2.1: Vortex tube

A curve in the fluid whose tangent is everywhere parallel to the vorticity ω is called a vortex line. If we draw a small closed curve C nowhere tangent to ω in the fluid and look at every vortex line passing through C, we obtain a two-dimensional surface. The object bounded by this surface is called a vortex tube (see Figure 2.1). Helmholtz's theorem states that the circulation is the same for any curve encircling the vortex tube and is constant

in time as the tube moves with the fluid [35]. We call this circulation the strength of the vortex tube.

The Kelvin's circulation theorem and the Helmholtz's theorem imply that vortex tubes are interesting entities in incompressible inviscid flows: they move as material volumes and their strength is a conserved quantity. These facts form the basis for vortex methods which will be introduced later.

If the domain occupied by the fluid is simply connected and if $\mathbf{u}$ satisfies $\nabla \cdot \mathbf{u} = 0$, there is a vector potential $\mathbf{A}$ such that $\mathbf{u} = \nabla \times \mathbf{A}$. Therefore

$$\omega = \nabla \times \mathbf{u} = \nabla \times (\nabla \times \mathbf{A}) = \nabla(\nabla \cdot \mathbf{A}) - \triangle \mathbf{A} \tag{2.7}$$

where $\triangle = \nabla^2 = \sum \partial_i^2$ is the Laplace operator. If $\mathbf{A}$ is chosen so that $\nabla \cdot \mathbf{A} = 0$, then

$$\triangle \mathbf{A} = -\omega. \tag{2.8}$$

Using the Green's function for the Laplacian, we can represent $\mathbf{A}$ in terms of ω. In three-dimensional space

$$\mathbf{A} = -G * \omega = \frac{1}{4\pi} \int \frac{1}{\mid \mathbf{x} - \mathbf{x}' \mid} \omega(\mathbf{x}') d\mathbf{x}' \tag{2.9}$$

where the integration is over the region occupied by the fluid, $d\mathbf{x}' = dx_1' dx_2' dx_3'$, and the Green's function $G(\mathbf{x}) = -(4\pi \mid \mathbf{x} \mid)^{-1}$ is the fundamental solution of the $\triangle$ operator. Taking the curl of (2.9), one finds

$$\mathbf{u} = \mathbf{K} * \omega \tag{2.10}$$

where $\mathbf{K} = -(4\pi \mid \mathbf{x} \mid^3)^{-1} \mathbf{x} \times$, $\times$ denoting a cross-product, and $*$ is a convolution. In other notations,

$$\mathbf{u}(\mathbf{x}) = -\frac{1}{4\pi} \int \frac{(\mathbf{x} - \mathbf{x}') \times \omega(\mathbf{x}')}{\mid \mathbf{x} - \mathbf{x}' \mid^3} d\mathbf{x}'. \tag{2.11}$$

This is the well-known Biot-Savart law, which has an analogy in the theory of magneto-statics. In this analogy the fluid velocity corresponds to the magnetic field intensity and vorticity to the current density.

Formula (2.9) also allows one to describe the kinetic energy of the flow in terms of the vorticity. Writing again $\mathbf{u} = \nabla \times \mathbf{A}$ as before, one obtains

$$E = \frac{1}{2} \int \mathbf{A} \cdot \omega d\mathbf{x} - \frac{1}{2} \int \nabla \cdot (\mathbf{u} \times \mathbf{A}) d\mathbf{x}. \tag{2.12}$$

The second term can be transformed into a surface integral that vanishes at infinity; thus the kinetic energy of a three-dimensional incompressible fluid in an unbounded region can be rewritten as the Lamb integral [65]:

$$E = \frac{1}{8\pi} \int d\mathbf{x} \int d\mathbf{x}' \frac{\boldsymbol{\omega}(\mathbf{x}) \cdot \boldsymbol{\omega}(\mathbf{x}')}{|\mathbf{x} - \mathbf{x}'|}, \tag{2.13}$$

which is a key formula in the statistics of vortex filaments in three dimensions.

2.2 Vortex Filaments

When the vortex tube is immediately surrounded by irrotational fluid and the cross section of the tube is small and finite, it will be referred to as a *vortex filament.* A vortex filament is often just called a *vortex.* The cross section of the vortex filament is the *vortex core.* A vortex ring is a special case of a vortex filament of circular shape (see Figure 2.2).

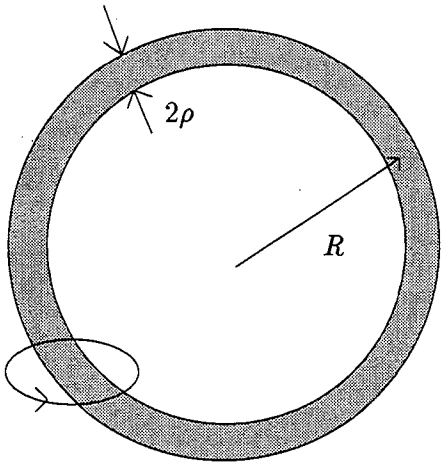

Figure 2.2: A vortex ring.

A vortex filament is usually represented by its centerline C. The vorticity $\boldsymbol{\omega}$ associated with a vortex filament points in the direction of the tangent to the curve C and its magnitude is characterized by the fact that

$$\int_S \boldsymbol{\omega} \cdot d\mathbf{A} = \Gamma, \tag{2.14}$$

where S is any surface which intersects the curve C transversally at only one point. Γ is called the strength of the vortex filament.

If the vorticity is concentrated on a single thin filament of circulation Γ, we have

$$\int_{\delta V} \omega dV \approx \Gamma \delta \mathbf{l} \tag{2.15}$$

where $\delta \mathbf{l}$ denotes a line element, δV a nearly cylindrical piece of element on the filament. Hence equation (2.11) reduces to

$$\mathbf{u}(\mathbf{x}) = -\frac{\Gamma}{4\pi} \int_C \frac{(\mathbf{x} - \mathbf{x}') \times d\mathbf{l}(\mathbf{x}')}{|\mathbf{x} - \mathbf{x}'|^3}. \tag{2.16}$$

It is well known that if self-induced motion of the line filament is calculated by evaluating the velocity from (2.16) on the filament itself, the result will be logarithmically infinite if the filament is curved and zero if it is straight. Thus, self-induced motion occurs only for curved filaments. But to obtain the correct value for the velocity, further considerations of the finite size of the vortex core as well as the vorticity distribution are required.

In this thesis we focus our attention on very thin vortex filaments. We shall use the term *thin* or *slender* to describe any vortex filament with a typical radius of the vortex core that is small compared to a characteristic radius of curvature. Thin vortices are very important in many respects. The discovery of coherent structures in turbulence has brought the hope that the study of vortices will lead to models and an understanding of turbulent flows, thereby solving or at least making less mysterious one of the great unsolved problems of classical physics. It has been suggested that thin vortices play an important role in the structure of turbulent flows [31]. Another suggestion is that the interaction of thin vortices may lead to the collapse of solutions to the three-dimensional Euler equations [84]. Thin vortices also play a dominant role in superfluid mechanics. The theory of line vortices and vortex rings is a part of modern macroscopic treatments of liquid helium II [90].

2.3 Vortex Folding, Equilibrium Theory

Vortex motion in three-dimensional space differs from vortex motion in two dimensions in several ways; the most significant result from vortex stretching. Vortex stretching causes vortex folding. An quantitative explanation is given in this section.

By avoiding the expensive and complicated process of calculating the evolution of vortex lines as it is determined by their own velocity field, stochastic dynamics has been proved to be simple and powerful in studying the three-dimensional vortex motion. To

appreciate the beauty of this approach, we provide an introduction to equilibrium statistical theory of vortex filaments.

2.3.1 Vortex Folding

The numerical experiments in [21], [102] show that vortex lines stretch very rapidly and vortex stretching is accompanied by vortex folding. The explanation of this folding is given by Chorin [22], [29] with the use of statistical theories. The analyses presented here are based on the energy arguments. Energy arguments are commonly used in the stability analysis. A system with no external forces cannot move from a low-energy state to a high-energy state; whereas it can move to a lower-energy state. Widnall and Sullivan [114] have investigated the stability of vortex rings by a different method. Their analysis is very subtle but is limited to small-amplitude perturbations. As we shall see below, the energy arguments are not limited by the topology of the perturbations.

If vortex filaments stretch, they must fold. To see this, consider a vortex ring with outer radius R and inner radius ρ (Figure 2.2). When the ring stretches, its length increases from R to αR, $\alpha > 1$. The conservation of volume yields that the radius of the arms ρ is reduced to $\rho/\sqrt{\alpha}$. Then $|\omega|$ in the arms increases to $\alpha|\omega|$ as a consequence of the conservation of circulation, and the energy $E = \frac{1}{2}\mathbf{M}\cdot\mathbf{u}$ ($\mathbf{M}$ = magnetization) increases from $E \sim \pi^2\rho^2|\omega|^2R$ to $\sim \pi^2\rho^2\alpha^2R|\omega|^2 = \alpha^2E$ [29]. According to the energy arguments, the loop must change its shape so that the velocity fields produced by the vorticity in its several parts cancel to a large extent (Figure 2.3). We now proceed to give this observation a more quantitative form.

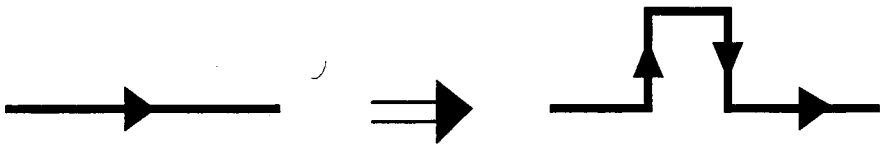

Figure 2.3: An elementary stretching.

Consider the vorticity in a vertical cylinder I of height l and a cross-section radius σ. The energy associated with the vorticity in I is given by the integral

$$E_I = \frac{1}{8\pi}\int_I d\mathbf{x}\int_I d\mathbf{x}'\frac{\omega(\mathbf{x})\cdot\omega(\mathbf{x}')}{|\mathbf{x}-\mathbf{x}'|}. \tag{2.17}$$

Assume the vorticity ω is parallel to the z-axis inside I, $\omega = (0, 0, \omega)$, and $\omega = \omega_0(x/\sigma, y/\sigma)$, with $\omega = 0$ when $\sqrt{x^2 + y^2} > \sigma$. E_I depends on σ, l, ω_0 and the circulation. We wish to know the dependence of E_I on σ, l when the circulation is fixed and ω keeps the form ω_0.

Let $\alpha > 0$ be a real parameter. Suppose all coordinate axes are stretched by a factor α,

$$\mathbf{x} \to \alpha \mathbf{x}, \tag{2.18}$$

$$\mathbf{x}' \to \alpha \mathbf{x}', \tag{2.19}$$

then

$$d\mathbf{x} \to \alpha^3 d\mathbf{x}, \tag{2.20}$$

$$d\mathbf{x}' \to \alpha^3 d\mathbf{x}', \tag{2.21}$$

$$\omega \to \alpha^{-2}\omega, \text{ (by conservation of circulation).} \tag{2.22}$$

Consequently,

$$E_I(\alpha\sigma, \alpha l) = \alpha E_I(\sigma, l). \tag{2.23}$$

Pick $\alpha = \frac{1}{\sigma}$, then

$$E_I(\sigma, l) = \sigma E_I(1, l/\sigma) = \sigma\phi(l/\sigma), \tag{2.24}$$

where ϕ is a function of one variable that depends on the vorticity distribution ω_0 in I. The asymptotic behaviors of ϕ for small or large arguments are [86]

$$\phi(r) \sim \begin{cases} r^2 & \text{for } r \to 0, \\ r \ln r & \text{for } r \to \infty. \end{cases} \tag{2.25}$$

Consider now a closed vortex filament V with a small, approximately circular cross-section of small but positive area. Suppose V can be approximated by N circular cylinders I_i, $i = 1, 2, ..., N$, of equal lengths h and of radii σ_i, $i = 1, 2, ..., N$. The energy of the velocity field associated with the filament V is

$$E = \frac{1}{8\pi} \int d\mathbf{x} \int d\mathbf{x}' \frac{\boldsymbol{\omega}(\mathbf{x}) \cdot \boldsymbol{\omega}(\mathbf{x}')}{|\mathbf{x} - \mathbf{x}'|} \tag{2.26}$$

$$= \sum_{i=1}^{N} \sum_{j \neq i} E_{ij} + \sum_{i=1}^{N} E_{ii}, \tag{2.27}$$

where

$$E_{ij} = \frac{1}{8\pi} \int_{I_i} d\mathbf{x} \int_{I_j} d\mathbf{x}' \frac{\boldsymbol{\omega}(\mathbf{x}) \cdot \boldsymbol{\omega}(\mathbf{x}')}{|\mathbf{x} - \mathbf{x}'|}. \tag{2.28}$$

In equation (2.27), the first sum is the *interaction energy* and the second term is the *self-energy.*

Let $\mathbf{t}_i$ be a vector of length h originating at the center of I_i and pointing in the direction of ω in I_i, $|i-j|$ the distance between I_i and I_j, and Γ_i the circulation of I_i. If the distances $|i-j|$ are large compared to h,

$$E_{ij} \approx \frac{\Gamma_i \Gamma_j}{8\pi} \frac{\mathbf{t}_i \cdot \mathbf{t}_j}{|i-j|}. \tag{2.29}$$

To evaluate the self-energy, we need to use the scaling property (2.24). One can evaluate E_{ii} through the relations

$$E_{ii}(h, \sigma_i) = \sigma_i E_{ii}(\frac{h}{\sigma_i}) = \sigma_i \phi(\frac{h}{\sigma_i}). \tag{2.30}$$

Suppose the vortex filament is stretched and the stretched vortex filament can be covered by $N' > N$ cylinders of length h. The self-energy $\sum_i E_{ii}$ associated with the new filament will increase because it will have more elements. If the energy is preserved, the interaction energy has to decrease which implies the inner products $\mathbf{t}_i \cdot \mathbf{t}_j$ must decrease,i.e., the filament must fold.

2.3.2 Equilibria of Vortex Filaments

In three dimensions, as time $t \to \infty$, a statistically steady state can be expected for a vortex filament system. Numerical studies of the equilibria of many-vortex systems have been carried out by many authors [2], [30], [64], and analytical studies via a Kosterlitz-Thouless theory can be found in the recent work of Chorin and Hald [32], [33]. For simplicity, we only consider a single vortex filament in a dilute suspension of such filaments [25].

The filament has an energy E given by the integral (2.26) which is approximated by (2.27). The limit $N \to \infty$ will be taken after the finite N case is discussed.

The vortex filament has many configurations. Assign to each configuration C the probability

$$P(C) = \frac{1}{Z} \exp(-\beta E), \tag{2.31}$$

where $Z = \sum_C P(C)$ is the partition function, $\beta = \frac{1}{T}$, and T is the temperature that can be positive or negative. A body with negative temperature is "hotter" than a body with positive temperature, and $|T| = \infty$ is the boundary between $T > 0$ and $T < 0$. The

temperature T introduced here has no connection with the molecular temperature of the underlying fluid. It is defined by

$$\frac{1}{T} = \frac{\partial S}{\partial < E >} \tag{2.32}$$

where S is the entropy, and the angular brackets $<>$ symbolize an average with respect to the Gibbs weight (2.31). Numerical calculations in [25] show that the average energy $< E >$ is an increasing function of both the temperature T and the length $L = Nh$ of the filament.

Define the quantity

$$\mu_{N,T} = \frac{\log < r_N >}{\log N} \tag{2.33}$$

where r_N is the end-to-end straight-line distance between the beginning and the end of the vortex filament. If $\lim_{N\to\infty}\mu_{N,T}$ exists and equals μ_T, for large N, $r \equiv < r_N > \sim N^{\mu_T}$, and thus $N \sim r^{1/\mu_T}$. It follows that $D = 1/\mu_T$ is the fractal dimension of the filament. A graph [25] of $\mu_{N,T}$ as a function of N and β shows that for fixed, finite N, $\frac{\partial \mu_{N,T}}{\partial T} > 0$, i.e., as T decreases, the vortex becomes an increasingly folded object.

As long as N is finite, strong vortices are less folded. Furthermore, a collection of vortex filaments with finite N looks multifractal [29].

As $N \to \infty$, the conclusion one reaches is

$$\mu_T = \begin{cases} 1 & \text{for } T < 0 \\ \mu & \text{for } |T| = \infty \\ 1/3 & \text{for } T > 0 \end{cases} \tag{2.34}$$

where $\mu \approx 0.588$ is the Flory exponent. Therefore, in the limit $N \to \infty$, the vortex filament is in one of three states: for $T < 0$, it is a smooth line; for $|T| = \infty$, the Gibbs factors $\exp(-E/T)$ are all unity, all configurations occur with equal probability and the vortex filament is a "polymer" — a self-avoiding equal probability random walk (SAW) — with fractal dimension $\approx 5/3$. Furthermore, the relation (2.32) shows that the entropy S has a maximum at $|T| = \infty$; and for $T > 0$, the vortex filament has dimension three and it is balled-up as the space available would allow. A heuristic explanation of this situation is simple: if $T < 0$, the Gibbs factor $\exp(-E/T)$ gives a high probability to high-energy states which are produced by bunching vortices together, forming large, concentrated vortex structures; if $T > 0$, low-energy states are favored and vortex filaments collapse into tightly folded structures, and they break down into small loops if reconnection is allowed.

At the boundary $|T| = \infty$, the energy spectrum has the universal form $E(k) \sim k^{-\gamma}$ for large k, where k is a wave number, γ the characteristic exponent (the Kolmogorov exponent). For an infinitely thin vortex $\gamma = \hat{D}$, the vector-vector correlation exponent for a polymer, and the most recent value generated by the Akao's scaling conjecture [3] yields $\hat{D} = 0.30$. For a filament with a finite, nontrivial cross-section, a heuristic analysis [31] gives $\gamma \approx 5/3$, the Kolmogorov value.

Consider now a smooth physical vortex and suppose that the vortex is embedded in a random classical (non-quantum) flow. The vortex will presumably stretch [29]. Conservation of energy and the increase in vortex length will cause the temperature T to decrease until $|T| = \infty$ is reached, assuming one can represent the evolution of the vortex as a succession of equilibrium states. Energy conservation and vortex connection forbid the crossing of the boundary $|T| = \infty$ [30]. Hence, the point $|T| = \infty$ is uncrossable barrier for a continuum Euler system, and that is where such a system will remain. A vortex filament system near an infinite temperature transition resembles a vortex system near the superfluid/normal fluid quantum transition [29].

In conclusion, as vortex lines stretch they fold and the temperature is decreased; a classical vortex system embedded in a three-dimensional incompressible flow is attracted to a stable equilibrium.

2.4 Superfluid Vortices, Hall-Vinen Friction

In this section we introduce a number of ideas without much detail. We first give a minimum background on superfluid helium, then describe the two-fluid model of superfluid helium, followed by an account on quantized vortices and Hall-Vinen friction.

2.4.1 The Two Fluid Model

The following discussion is largely based on Tilley & Tilley [107].

Of all known substances the two isotopes of helium have the lowest normal boiling points, 4.215K for ^{4}He and 3.19K for ^{3}He. Immediately below its boiling point, ^{4}He behaves as an ordinary classical fluid with non-zero viscosity and energy dissipation. As liquid ^{4}He is cooled further, at the critical temperature $T_\lambda = 2.172K$ it undergoes a phase transition at which non-dissipative superfluid currents begin to appear. This transition is named the

lambda transition because of the λ-like shape of the specific heat as a function of temperature; it is also known as the superfluid transition. The phase transition is a second-order transition, since at T_λ energy is continuous but the specific heat has a cusp. Conventionally liquid ^{4}He is denoted as helium I above T_λ and helium II below it.

Liquid ^{3}He also suffers a phase transition when the temperature is reduced to about $3 \times 10^{-3} K$. Superfluid ^{3}He has many of analogous properties as helium II. However, due to the experimental difficulties at these ultralow temperatures there is not as much experimental data available as there is for ^{4}He. In the following we confine ourselves to a description of ^{4}He. For more information about superfluid ^{3}He, see [36], [71], [112].

Many physical experiments indicate that helium II has the properties of both a normal fluid and a superfluid. In order to explain this behavior, Tisza [108] suggested the two-fluid model. According to this model, helium II is regarded as a mixture of normal fluid and superfluid. Each fluid has its own local velocity, respectively $\mathbf{v}_n$ for the normal fluid and $\mathbf{v}_s$ for the superfluid; likewise each has its own mass density, ρ_n and ρ_s. Therefore the total mass density ρ of the helium II is given by

$$\rho = \rho_n + \rho_s, \tag{2.35}$$

and the total mass current density by

$$\mathbf{J} = \rho_n \mathbf{v}_n + \rho_s \mathbf{v}_s. \tag{2.36}$$

When the fluid velocities are sufficiently small, the superfluid is expected to move as an ideal fluid obeying equations of the Euler type, and the normal fluid as a viscous fluid with viscosity ν obeying equations of the Navier-Stokes type. The peculiar thermal properties of helium II, characterized by the total entropy per unit mass S and temperature gradients ∇T, add a thermodynamic term to the equations of motion. When the velocities are higher, various additional terms are needed due to the fact that the relative velocity between the two fluids $(\mathbf{v}_n - \mathbf{v}_s)$ is a thermodynamic parameter of helium II. The simplest form of the two-fluid equations for the superfluid and normal fluid velocities $\mathbf{v}_s$ and $\mathbf{v}_n$ can be written (ignoring both bulk viscosity and thermal conductivity)

$$\rho_s \frac{D_s \mathbf{v}_s}{Dt} = -\frac{\rho_s}{\rho} \nabla P + \rho_s S \nabla T - \mathbf{F}_{sn}, \tag{2.37}$$

$$\rho_n \frac{D_n \mathbf{v}_n}{Dt} = -\frac{\rho_n}{\rho} \nabla P - \rho_s S \nabla T + \mathbf{F}_{sn} + \nu \nabla^2 \mathbf{v}_n, \tag{2.38}$$

where $\frac{D_s}{Dt} \equiv \frac{\partial}{\partial t} + \mathbf{v}_s \cdot \nabla$, $\frac{D_n}{Dt} \equiv \frac{\partial}{\partial t} + \mathbf{v}_n \cdot \nabla$, P is the pressure, and $\mathbf{F}_{sn}$ is the mutual friction force per unit volume between the normal fluid and superfluid. Viscosity and mutual friction can sometimes be neglected for slow flows.

The two-fluid equations have been validated through the prediction [6], [7], [115] and observation [53], [55], [72], [81], [100] of different sound modes present in superfluid helium, and through the quantitative and qualitative agreement between the experimental results and theoretical predictions in nonlinear properties of superfluid helium [70], [75], [109].

2.4.2 Quantized Vortices

When the two-fluid model was originally introduced it was assumed that the superfluid component was a classically inviscid fluid and for such an ideal fluid, the curl of the velocity was taken to be zero:

$$\nabla \times \mathbf{v}_s = 0. \tag{2.39}$$

In a simply connected region, (2.39) implies $\mathbf{v}_s = 0$ at every point throughout the superfluid. In particular, if a cylindrical bucket containing helium II is rotated, then the superfluid should remain at rest and the configuration of the free surface of rotating helium II should be a paraboloid of the form [79]

$$z = \frac{\rho_n}{\rho} \frac{\Omega^2 r^2}{2g}, \tag{2.40}$$

where z is the height of the surface along the axis of rotation, Ω is the angular velocity of rotation, r is the perpendicular distance from the axis of rotation, and g is the acceleration due to gravity. In contrast, the experiment done by Osborne [79] in 1950 showed that the surface shape was

$$z = \frac{\Omega^2 r^2}{2g}, \tag{2.41}$$

indicating that the entire fluid was undergoing rotation and not just the normal fluid. It became clear that the condition (2.39) could not hold everywhere in the fluid. Vorticity has to be allowed in the superfluid velocity field.

To explain the rotation of the superfluid, following Onsager [78] and Feynman [42], we amend the constraint (2.39) on the superfluid velocity field so that $\nabla \times \mathbf{v}_s = 0$ almost everywhere on the fluid except on isolated singular lines which form an array in the fluid. These isolated singular lines are "vortex filaments".

In a cylindrical container, a vortex filament has a velocity

$$\mathbf{v}_s = \frac{A}{r}\mathbf{e}_\theta, \tag{2.42}$$

where A is some constant. The constant A is determined by assuming the action of a single helium atom in the fluid to be quantized in units of h, the Planck's constant, so that

$$\int_C \mathbf{P}_s \cdot d\mathbf{l} = nh, \tag{2.43}$$

where C is a contour enclosing the vortex core, $\mathbf{P}_s$ is the momentum of the superfluid, and n is any integer. From (2.43) we see that the circulation of the vortices is quantized:

$$\Gamma = \int_C \mathbf{v}_s \cdot d\mathbf{l} = \frac{nh}{m_4}, \ n = 1, 2, 3, ... \tag{2.44}$$

where m_4 is the mass of a ^{4}He atom. The constant h/m_4 is called the quantum of circulation, and it has the value 9.98×10^{-4} cm^2/sec.

The first experimental evidence for quantized vortices was given by Vinen [111]. Later Rayfield and Reif [88] also provided excellent experimental confirmation of the quantization of circulation in helium II.

It is found theoretically [8], [43], [45], [91] and experimentally [44], [88] that the core radius of superfluid vortices is on the order of 1Å, so the core is very thin. In the next section we will give a brief introduction into what is known as Hall-Vinen friction in helium II.

2.4.3 Hall-Vinen Friction

Because of the presence of quantized vortices in superfluid helium, the force $\mathbf{F}_{sn}$ is interpretted as a drag force exerted on the quantized vortices. This force is the means whereby the rotation of the vessel and the normal fluid can be communicated to the superfluid to bring about the simulation of rigid-body rotation. In order to study this force, Hall and Vinen [50] performed an experiment on a sample of helium II rotating uniformly at angular velocity $\mathbf{w}$. In their experiment they assumed that the quantized vortices were straight and parallel to the rotation axis. Under the conditions of their experiment, Hall and Vinen [51] proposed the following relation for $\mathbf{F}_{sn}$:

$$\mathbf{F}_{sn} = -\frac{B\rho_s\rho_n}{\rho}\hat{\mathbf{w}} \times [\mathbf{w} \times (\bar{\mathbf{v}}_s - \bar{\mathbf{v}}_n)] - \frac{B'\rho_s\rho_n}{\rho}\hat{\mathbf{w}} \times (\bar{\mathbf{v}}_s - \bar{\mathbf{v}}_n). \tag{2.45}$$

Here $\hat{\mathbf{w}}$ is the unit vector $\mathbf{w}/|\mathbf{w}|$ which defines the rotation axis. The two fluid velocities $\bar{\mathbf{v}}_s$ and $\bar{\mathbf{v}}_n$ are averages taken over a region containing many vortex lines. The dimensionless coefficients B and B' describe the dissipative and nondissipative contributions to $\mathbf{F}_{sn}$. In the experiments, it is the parameters B and B' that are measured.

Hall-Vinen friction reveals that the motion of quantized vortices undergoes frictional dissipation. Hall-Vinen friction probably results from the interaction between the vortices and sound waves in the fluid [76]; and represents a coupling between the molecular degrees of freedom and the vortex degrees of freedom. Hence it is very likely that the molecular temperature of the fluid is identical to the superfluid vortices temperature.

2.5 Differences Between Classical Vortices and Superfluid Vortices

At the end of this chapter we wish to emphasize some important differences between classical (i.e., non quantum) vortices and superfluid vortices.

From the two fluid model, we have seen that the equations describing the superfluid component are the same as the Euler equations describing an ideal fluid. The paradox is that vortices described by the same equations behave very differently in many important aspects. Classical vortices have a non-trivial cross-section, and they stretch and fold in a very complicated manner. The rate at which classical vortex length per unit volume L varies is proportional to L [29]. Numerical and physical experiment, as well as some theory [26], show that vortex lines stretch monotonically and violently, possibly to infinity in a finite time [13], [21], [46]. By contrast, superfluid vortices are nearly true lines, and with some exceptions (i.e., near the critical temperature) they generally look smoother than classical vortices and remain relatively ordered. At the critical temperature theoretical and numerical results show that superfluid vortices are fractal objects [2], [33], [39], [101]. By a dimensional argument Vinen [110] showed that for superfluid vortices $\frac{dL}{dt}$ should be proportional to $L^{3/2}|\mathbf{w}|$, where $\mathbf{w} = \mathbf{v}_n - \mathbf{v}_s$ is a quantum "counterflow" (i.e., $\mathbf{v}_s$ and $\mathbf{v}_n$ are in opposite direction) velocity. As $\mathbf{w}$ tends to zero, L is finite.

A qualitative explanation can be given with the use of the equilibrium theory. The rate of change of L is connected with the rate of change of the temperature T. A classical fluid has a self-adjusting temperature T such that $|T| \to \infty$, and there are no bounds on

L. Hence classical vortices may stretch violently. In superfluid, wave/vortex interactions control T and T is fixed. Therefore L is a finite constant and there is no stretching for superfluid vortices. According to our work, these differences may be accounted for by the fact that superfluid vortices are extremely slender, if they are in addition forbidden to fold on scales comparable to their very small radius.

Chapter 3

Equations of Motion for Thin Vortices

Three modeling approaches are adopted in this chapter to analyze the motion of slender vortex filaments. The first approach is the local induction approximation, which is equivalent to a cubic nonlinear Schrödinger equation. The second approach is due to Klein and Majda, who derived a simplified asymptotic equation for the motion of thin vortex filaments. The third approach, given by Klein and Knio, is a three-dimensional simulation based on a vortex element method.

Section 3.1 gives a derivation of the local induction equation. It points out some properties of the local induction equation, including alternate forms, exact solutions and arc length conservation. Section 3.2 briefly reviews the formulation and mathematical features of the Klein-Majda equation. Section 3.3 introduces the standard thin-tube model and outlines how the Klein-Knio equation is derived. Section 3.4 summarizes the three different kinds of equations of motion. Section 3.5 reviews the conservation laws in three-dimensional free space, and studys the conservation laws in the special case of flows which are periodic in the x direction and unbounded in the y and z directions.

3.1 The Local Induction Approximation (LIA)

The local induction approximation (also called the self-induction approximation) replaces the velocity given by the Biot-Savart law (2.16) by a different velocity that depends only on a local curvature of the vortex filament. It is an approximation applicable to the

limiting case of a vortex filament of infinitesimal core size with negligible long-distance effects, and is commonly utilized in the investigations of the motion of superfluid vortices.

3.1.1 The Local Induction Equation

To derive the local induction approximation [5], we follow closely the discussion presented in Batchelor [9].

Consider the velocity induced by a filament itself near a point P on the filament. Describe the vortex filament by $\mathbf{r}(s)$, where s is an arc length parameter measured along the filament and $\mathbf{r}(s)$ is the position vector. The unit tangent vector $\mathbf{t}$ to the filament is given by

$$\mathbf{t} = \frac{d\mathbf{r}}{ds} \tag{3.1}$$

and the curvature κ of the filament by

$$\frac{d\mathbf{t}}{ds} = \kappa\mathbf{n} \tag{3.2}$$

where $\mathbf{n}$ is the unit normal vector. The curvature of a curve at a given point measures how quickly the curve changes direction at that point. The unit vector

$$\mathbf{b} = \mathbf{t} \times \mathbf{n} \tag{3.3}$$

is the binormal vector. The vectors $\mathbf{t}$, $\mathbf{n}$, $\mathbf{b}$ form an orthonormal coordinate system at all points along the curve $\mathbf{r}(s)$. The variation of the intrinsic basis $\mathbf{t}$, $\mathbf{n}$, $\mathbf{b}$ along $\mathbf{r}(s)$ is described by the Serret-Frenet equations:

$$\mathbf{b}' = -\tau\mathbf{n}, \tag{3.4}$$

$$\mathbf{n}' = -\kappa\mathbf{t} + \tau\mathbf{b}, \tag{3.5}$$

$$\mathbf{t}' = \kappa\mathbf{n}, \tag{3.6}$$

where a prime denotes differentiation with respect to s. τ defined by (3.4) is the torsion of the curve. The torsion is a measure of the degree of twisting of a curve. A curve is determined by its curvature and torsion up to rotation and translation [106].

Without loss of generality, assume $s = 0$ at the point P. If we denote the coordinate vectors at $s = 0$ as $\mathbf{t}_0$, $\mathbf{n}_0$, $\mathbf{b}_0$, expansion of $\mathbf{r}(s)$ in a Taylor series at $s = 0$ gives

$$\begin{aligned}\mathbf{r}(s) &= \mathbf{r}(0) + s\frac{d\mathbf{r}(0)}{ds} + \frac{s^2}{2!}\frac{d^2\mathbf{r}(0)}{ds^2} + \frac{s^3}{3!}\frac{d^3\mathbf{r}(0)}{ds^3} + O(s^4) \\ &= \mathbf{r}(0) + s\mathbf{t}_0 + \frac{\kappa s^2}{2!}\mathbf{n}_0 + \frac{s^3}{3!}\mathbf{t}_0'' + O(s^4).\end{aligned} \tag{3.7}$$

Here the smoothness of the curve is assumed so that the derivatives exist.

Similarly,

$$\mathbf{t}(s) = \mathbf{t}_0 + \kappa s \mathbf{n}_0 + \frac{s^2}{2!}\mathbf{t}_0'' + O(s^3). \tag{3.8}$$

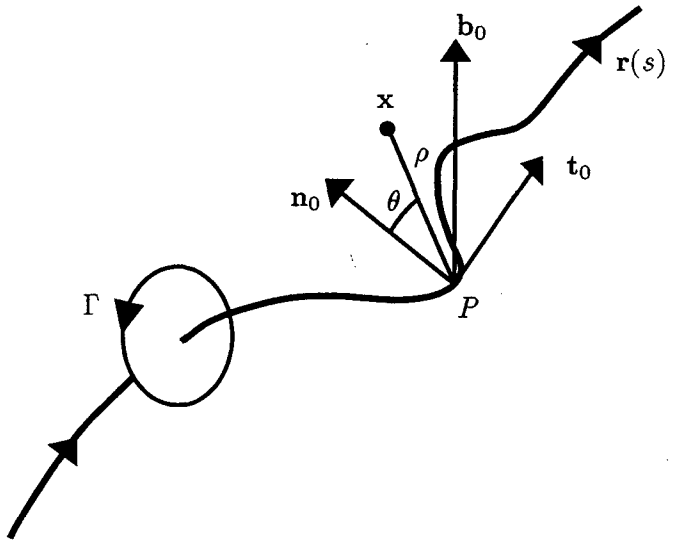

Figure 3.1: A portion of vortex filament $\mathbf{r}(s)$ near point P.

Let $\mathbf{x} = y\mathbf{n}_0 + z\mathbf{b}_0$ be a point close to the point P, where $y = \rho cos\theta$, $z = \rho sin\theta$ (see Figure 3.1). Substitute the expansions for $\mathbf{r}(s)$ and $\mathbf{t}(s)$ into the integral in equation (2.16). Ignore the contribution to the integral from points such that $\mid s \mid > L$, where L is some small but fixed limit of integration. The choice of L to best approximate (2.16) depends on the details of the vortex configuration. After some elementary algebra and keeping the leading order terms, we find

$$\mathbf{u}(\mathbf{x}) = \frac{\Gamma}{2\pi L}(\mathbf{b}_0 cos\theta - \mathbf{n}_0 sin\theta) + \frac{\Gamma\kappa}{4\pi} ln\frac{L}{\rho}\mathbf{b}_0 + O(1). \tag{3.9}$$

If $\rho << L$, i.e. the limiting case of a vortex filament, the term which is order unity in (3.9) can be neglected, corresponding to an omission of long-distance effects.

The first term in the expression (3.9) represents the circular motion around a straight filament. The second term is an unbounded contribution, due to the curvature κ, in the direction of the binormal. An infinite long straight filament would produce a velocity identical to the first term in (3.9), but it remains stationary in its own velocity; thus we assume that the second term gives an approximation of the velocity on the filament itself:

$$\mathbf{u}(\mathbf{x}) = \mathbf{b}_0 \frac{\Gamma\kappa}{4\pi} ln\frac{L}{\rho}. \tag{3.10}$$

This is called the *local induction equation* or the *self-induction equation.* An immediate consequence of the local induction equation is an intuitive understanding of how a vortex ring moves through a fluid: if L is replaced by the radius of curvature, we have an approximation to (3.10). A vortex ring moves through the fluid principally because of its curvature.

Generally ρ is taken as the true finite radius of the vortex filament. Assuming that the logarithmic term $\frac{\Gamma}{4\pi}\ln\frac{L}{\rho}$ is a constant, one can eliminate this constant by scaling time and obtain an equation for the motion of a vortex filament

$$\frac{\partial \mathbf{x}}{\partial t} = \mathbf{t} \times \frac{\partial \mathbf{t}}{\partial s} = \kappa \mathbf{b}. \tag{3.11}$$

Differentiation of both sides of (3.11) with respect to s gives the local induction equation in terms of the tangent vector:

$$\frac{\partial \mathbf{t}}{\partial t} = \mathbf{t} \times \frac{\partial^2 \mathbf{t}}{\partial s^2}. \tag{3.12}$$

3.1.2 Alternate Forms and Exact Solutions

Equation (3.11) has two alternate forms. The first form is due to Betchov [15]. He derived a pair of intrinsic equations describing the evolution of the curvature κ and torsion τ of a filament which evolves according to the local induction equation (3.11):

$$\frac{\partial \kappa}{\partial t} = -2\kappa'\tau - \kappa\tau', \tag{3.13}$$

$$\frac{\partial \tau}{\partial t} = (\frac{1}{\kappa}\kappa'' - \tau^2 + \frac{1}{2}\kappa^2)', \tag{3.14}$$

where $' \equiv \frac{\partial}{\partial s}$. (3.13) is called the *first intrinsic equation* and (3.14) the *second intrinsic equation.* The second form is credited to Hasimoto [52]. He elegantly demonstrated that equation (3.11) can be reduced to a nonlinear Schrödinger equation (NLSE)

$$\frac{1}{i}\frac{\partial \phi}{\partial t} = \frac{\partial^2 \phi}{\partial s^2} + \frac{1}{2}\phi \mid \phi \mid^2 \tag{3.15}$$

where t is the time, s is the length measured along the filament, ϕ is the complex function defined in terms of the filament curvature κ and torsion τ:

$$\phi = \kappa \ \exp(i \int_0^s \tau ds). \tag{3.16}$$

The NLSE possesses solutions that are solitons, i.e., nonlinear solitary waves that preserve their identity even after a collision of two waves. We call (3.16) the *Hasimoto transformation* and ϕ the *filament function* which contains all the geometrical information for the filament.

A variety of exact solutions of equation (3.11) are known. The simplest solutions are those with constant curvature and torsion, for example, straight lines or circles. A more complicated solution is the curve with constant torsion τ described by [52]:

$$\mathbf{r}(s,t) = (s - \frac{2\mu}{\beta}\tanh(\beta\xi), \frac{2\mu}{\beta}\mathrm{sech}(\beta\xi)\cos\theta, \frac{2\mu}{\beta}\mathrm{sech}(\beta\xi)\sin\theta), \tag{3.17}$$

where β is a constant, $\mu = (1+(\frac{\tau}{\beta})^2)^{-1}$, $\xi = s - 2\tau t$, $\theta = \tau\xi + (\beta^2 - \tau^2)t$. The solution (3.17) describes the propagation of a hump of helical shape along a vortex line with a constant velocity 2τ. Additional exact solutions can be found in [16].

A characteristic property of the local induction approximation is that it preserves the length of the vortex filament. This can be seen from the fact that vortex stretching is associated with a velocity component along the **n** direction and there is no such velocity contribution in (3.11) since **b** is orthogonal to **n**. Besides conserving length, the local induction approximation keeps the linear and angular impulses constant [92].

3.2 The Klein-Majda (KM) Equation

While the local induction approximation does not allow for any vortex stretching, numerical simulations indicate that vortex stretching occurs for moderately thin vortex filaments in incompressible fluids. To retain vortex stretching, Klein and Majda [59] developed an asymptotic theory for slender vortex filaments.

The slender vortices in Klein-Majda regime are to leading order straight vortex filaments that are subject to small amplitude displacements. The displacement of the vortex filament centerlines away from the straight reference lines may be, but is not necessarily, large in comparison with a typical core size of the filament but it must be small compared to a typical perturbation wave length. In turn, the perturbation wavelengths are small compared to a characteristic radius of curvature of the filament. Thus with lengths measured on the curvature scale, the slender vortices in Klein-Majda regime are characterized by *small amplitude - short wavelength* distortions of a slender columnar vortex.

3.2.1 Formulation

To make the presentation easy, we consider a single isolated vortex filament in a quiescent environment; more general situations (e.g. filaments embedded in a background flow; interaction of parallel/antiparallel pairs of slender vortices) are studied in [62], [61].

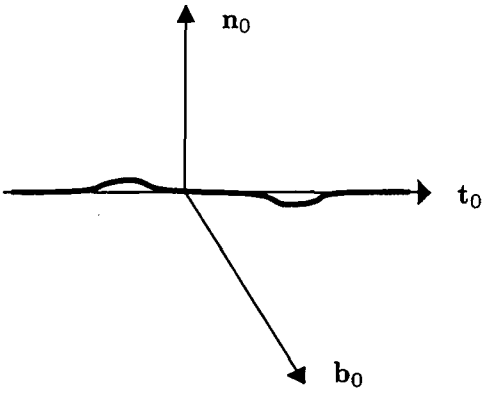

Figure 3.2: A special perturbation of the straight reference filament: ($\mathbf{t}_0$,$\mathbf{n}_0$,$\mathbf{b}_0$) form a right-handed orthonormal basis, $\mathbf{x}^{(2)} = \alpha(\sigma)\mathbf{n}_0 + \beta(\sigma)\mathbf{b}_0$.

Consider small amplitude short wavelength perturbations of a straight vortex filament (Figure3.2). Assume the filament centerline is described by

$$\mathbf{x}(s,t;\varepsilon) = \varepsilon\sigma\mathbf{t}_0 + \varepsilon^2\mathbf{x}^{(2)}(\sigma,\tau) + o(\varepsilon^2) \tag{3.18}$$

where $\mathbf{x}$ is the position vector, s is the arc length along the curve, t is the time, $\sigma = s/\varepsilon$ and $\tau = t/\varepsilon^2$ are the scaled space and time coordinates, $\mathbf{t}_0$ is a constant unit vector, ε is a perturbation scaling parameter and $\varepsilon << 1$. The vortex core size δ and ε are linked through the distinguished limit

$$\varepsilon^2 = \frac{1}{\ln\frac{2\varepsilon}{\delta} + C} \tag{3.19}$$

where C is some constant.

When the far-field flow surrounding the filament is at rest, the filament motion obeys the perturbed binormal law

$$\frac{\partial\mathbf{x}(s,t)}{\partial t} = \kappa\mathbf{b}(s,t) + \varepsilon^2\mathbf{v}(s,t) \tag{3.20}$$

where $\varepsilon^2\mathbf{v}(s,t)$ is a small perturbation velocity. Using the curve representation (3.18) and by the method of asymptotic expansions, one finds

$$\mathbf{v} = I[\mathbf{x}^{(2)}] \times \mathbf{t}_0. \tag{3.21}$$

Here $I[\cdot]$ is the linear nonlocal operator

$$I[w](\sigma) = \int_{-\infty}^{\infty} \frac{1}{|h^3|} \left[w(\sigma+h) - w(\sigma) - hw'(\sigma+h) + \frac{h^2}{2} H(1-|h|) w''(\sigma) \right] dh \qquad (3.22)$$

with the notation $' = \frac{\partial}{\partial \sigma}$ and H is the Heaviside function:

$$H(y) = \begin{cases} 1 & \text{if } y \geq 0, \\ 0 & \text{otherwise.} \end{cases} \qquad (3.23)$$

The nonlocal contribution of the filament is replaced by I whose effect can be understood by considering its Fourier symbol:

$$\begin{aligned} \hat{I}(\xi) &= \int_{\mathbf{R}} e^{-i\sigma\xi} I(\sigma) d\sigma \\ &= |\xi|^2 (-\ln|\xi| + C_0) \end{aligned} \qquad (3.24)$$

where $C_0 = \frac{1}{2} - \gamma$, and γ is Euler's constant.

Klein and Majda showed that Hasimoto's transformation (3.16) turns the evolution equation (3.20) with $\mathbf{v}$ from (3.21) into the perturbed nonlinear-nonlocal Schrödinger equation

$$\frac{1}{i} \frac{\partial \phi}{\partial \tau} = \frac{\partial^2 \phi}{\partial \tilde{\sigma}^2} + \varepsilon^2 \left(\frac{1}{2} \phi |\phi|^2 - I[\phi] \right) \qquad (3.25)$$

with $\tau = t/\varepsilon^2$ and $\tilde{\sigma} = s/\varepsilon$. We call (3.25) the *Klein-Majda equation.* In this equation, the nonlocal effect $I[\phi]$ directly competes with the cubic nonlinearity. Thus, the nonlocal contributions become as important as the nonlinear local induction effects. Furthermore, it is shown that the nonlocal term $-\varepsilon^2 I[\phi]$ is responsible for filament local self-stretching.

Klein and Majda also proved the global existence and uniqueness of solutions of equation (3.25) for any initial data in the Hilbert space $\tilde{H}$ defined by

$$\tilde{H} = \{\phi : (1 + \ln^+(|\xi|))^{1/2} |\xi| \, |\, \hat{\phi}(\xi) \in L^2(\mathbf{R})\} \qquad (3.26)$$

with

$$\ln^+(s) = \begin{cases} \ln(s) & \text{for } s \geq 1, \\ 0 & \text{for } s < 1. \end{cases} \qquad (3.27)$$

It is shown in [59] that the nonlocal operator generates a highly singular perturbation of the NLSE (3.15). According to the numerical calculations presented in [60], the filament function ϕ develops higher and much narrower peaks as time evolves when compared with the corresponding solutions of NLSE; and these curvature peaks correspond to the birth of small scale "hairpins" or kinks along the actual vortex filament.

3.3 The Klein-Knio (KK) Equation

Neither the local induction equation nor the Klein-Majda equation provides a good approximation to the nonlocal contribution. The local induction equation simply ignores it while the Klein-Majda equation approximates it by a linear operator with errors of order $O(\varepsilon)$. In this section we discuss a method due to Klein and Knio [58], which yields an asymptotically correct representation of the nonlocal induction effects. This method allows us to accurately represent the influence of the vortex core structure on the vortex filament motion including a nontrivial axial flow.

3.3.1 The Standard Thin-tube Model

The standard thin-tube model [63] is a simplified version of general vortex element method [12] for three-dimensional incompressible flows. The model represents a slender vortex as a single chain of overlapping vortex elements. Each element is a circular cylinder characterized by a circulation Γ_i equal to the flux of vorticity across its cross section and by two Lagrangian variables which describe the endpoints of the associated line segment. The Lagrangian variables are moving with the fluid and can be denoted by χ_i, $i = 1, 2, ..., N$. The vortex elements are ordered so that the indices increase in the direction of the vorticity. Therefore, the vorticity can be discretized as

$$\omega(\mathbf{x}, t) = \sum_{i=1}^{N} \Gamma_i \delta\chi_i(t) f_\delta(\mathbf{x} - \chi_i^c(t)). \tag{3.28}$$

In this expression, f_δ is a smooth approximation to the Dirac delta function with a cutoff radius δ and obeys the relationship:

$$f_\delta(\mathbf{x}) = \frac{1}{\delta^3} f(\frac{|\mathbf{x}|}{\delta}), \tag{3.29}$$

and

$$\delta\chi_i(t) = \chi_{i+1}(t) - \chi_i(t), \tag{3.30}$$

$$\chi_i^c(t) = \frac{\chi_{i+1}(t) + \chi_i(t)}{2}, \tag{3.31}$$

denote respectively the length and center of the i-th vortex element. To enhance accuracy, the smoothing function $f(\mathbf{x})$ is chosen subject to the conditions [12]:

1. $f(\mathbf{x})$ is smooth and rapidly decreasing, i.e.,

$$|D^{\alpha} f(\mathbf{x})| \leq C_{\alpha i}(1+|\mathbf{x}|^2)^{-i} \tag{3.32}$$

for every multi-index α and every integer i;

2. $\int f(\mathbf{x})d\mathbf{x} = 1$;

3. $\int \mathbf{x}^{\alpha} f(\mathbf{x})d\mathbf{x} = 0$, for $1 \leq |\alpha| \leq m-1$, for some integer m.

The velocity at a point $\mathbf{x}$ can be obtained by inserting (3.28) into (2.16) and performing the integration. The result is the following desingularized version of the Biot-Savart law:

$$\mathbf{u}^{\mathrm{ttm}}(\mathbf{x},t) = -\frac{1}{4\pi}\sum_{i=1}^{N}\Gamma_i \frac{(\mathbf{x}-\chi_i^c(t))\times\delta\chi_i^c(t)}{|\,\mathbf{x}-\chi_i^c(t)\,|^3} K_{\delta}(\mathbf{x}-\chi_i^c(t)) \tag{3.33}$$

where

$$K_{\delta}(\mathbf{x}) \equiv K(\frac{|\mathbf{x}|}{\delta}) \tag{3.34}$$

and $K(r)$ is the velocity smoothing kernel corresponding to the vorticity smoothing kernel:

$$K(r) = 4\pi\int_0^r \bar{r}^2 f(\bar{r})d\bar{r}. \tag{3.35}$$

The calculated velocity $\mathbf{u}^{\mathrm{ttm}}(\chi_i)$ is used to advance χ_i.

In the above standard thin-tube approach the cutoff radius is implicitly assumed to be the physical characteristic vortex core radius. This assumption turns out to be wrong because of the differences between the physical and numerical core structures [58]. To modify the standard thin-tube model, Klein and Knio derive a new asymptotic expression for the induced velocity.

3.3.2 The Klein-Knio Equation: Modification of Thin-tube Model

First we introduce a time-dependent, orthogonal curvilinear coordinate system attached to a slender vortex filament with diameter d of the vortex core and a characteristic radius R ($d << R$). Suppose the vortex filament reference curve is given parametrically at time t by $\mathbf{X}(s,t)$, where s is the arc length along the curve at $t=0$, and P is any point not on $\mathbf{X}$ with corresponding position vector $\mathbf{P}$. Let $\mathbf{X}(s,t)$ be the point on the reference curve which has the shortest distance from the reference curve to the point P. Denote the unit tangential, normal, and binormal vectors associated with the reference curve at the

point $\mathbf{X}(s,t)$ respectively as $\mathbf{t}$, $\mathbf{n}$, and $\mathbf{b}$. A schematic representation of a vortex filament in curvilinear coordinate system is shown in Figure 3.3.

The position vector $\mathbf{P}$ can be written as

$$\mathbf{P}(x,y,z) = \mathbf{X}(s,t) + r\mathbf{e}_r \tag{3.36}$$

where $\mathbf{e}_r$ is a unit vector in the $\mathbf{n}$-$\mathbf{b}$ plane. Introduce the unit vector $\mathbf{e}_\theta$ orthogonal to $\mathbf{e}_r$ in the $\mathbf{n}$-$\mathbf{b}$ plane. Define

$$\theta = \varphi - \int_0^{\tilde{s}} \tau(\tilde{s})d\tilde{s} \tag{3.37}$$

where φ is the angle between the radial vector $\mathbf{e}_r$ and the normal vector $\mathbf{n}$, $\tilde{s}(s,t)$ is the arc length of the reference curve at time t, and $\tau(\tilde{s})$ is the torsion of the curve. The radial,circumferential and tangential coordinates (r,θ,s) form an orthogonal system [19]. Any point in the fluid can be represented in curvilinear coordinates (r,θ,s) associated with some point on the vortex filament reference curve.

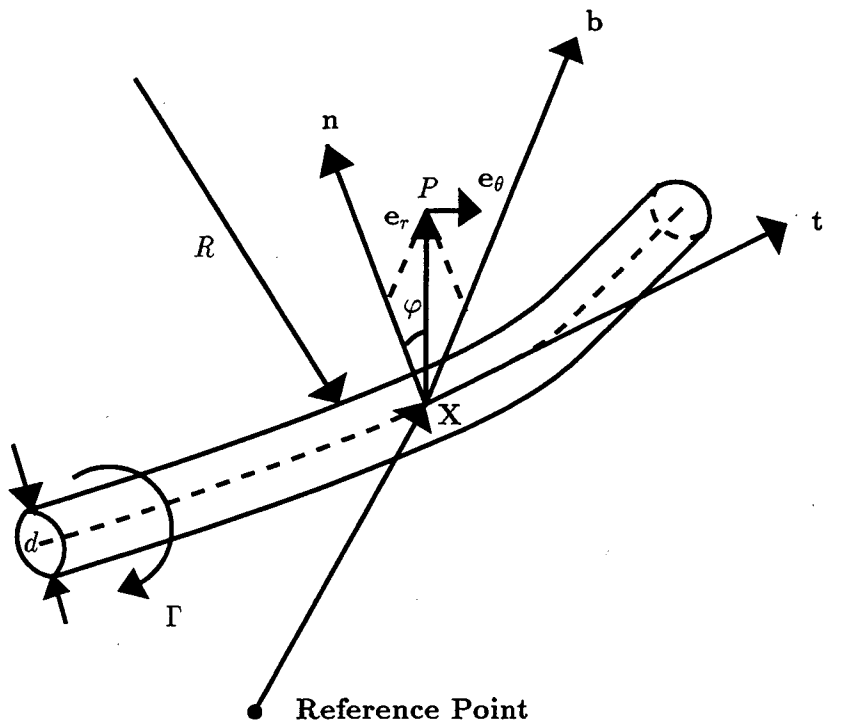

Figure 3.3: Representation of a vortex filament in curvilinear coordinate system

In the derivation of the Klein-Knio equation, the principal assumption is that the slender vortex filament has the following core vorticity distribution in curvilinear coordinate

system:

$$\begin{aligned}\omega(\mathbf{x},t;\delta) &= \frac{1}{\delta^2}\left(\eta^{(0)}(\frac{r}{\delta},s,t)\mathbf{e}_\theta+\zeta^{(0)}(\frac{r}{\delta},s,t)\mathbf{t}\right)\\ &+ \frac{1}{\delta}\left(\xi^{(1)}(\frac{r}{\delta},\theta,s,t)\mathbf{e}_r+\eta^{(1)}(\frac{r}{\delta},\theta,s,t)\mathbf{e}_\theta+\zeta^{(1)}(\frac{r}{\delta},\theta,s,t)\mathbf{t}\right)\\ &+ O(1)\end{aligned} \tag{3.38}$$

where $\delta = d/R$ is a dimensionless parameter, $\xi^{(i)}$, $\eta^{(i)}$, $\zeta^{(i)}$ are asymptotic expansion functions for the radial, circumferential and axial vorticity components in the vortex core. Notice that the leading order terms $\eta^{(0)}, \zeta^{(0)}$ are assumed to be independent of θ so that the leading order core structure is axisymmetric.

Denote the core radius by δ. Pick a parameter δ_B satisfying

$$\delta^{1/2} << \delta_B << 1 \tag{3.39}$$

and split the integration in (2.16) into a local and a nonlocal contribution:

$$\mathbf{u}(\mathbf{x_1}) = -\frac{1}{4\pi}\left[\int_{\mathbf{R}^3\setminus B_{\delta_B}} F(\mathbf{x},\mathbf{x_1})d\mathbf{x} + \int_{B_{\delta_B}} F(\mathbf{x},\mathbf{x_1})d\mathbf{x}\right]. \tag{3.40}$$

Here $F(\mathbf{x},\mathbf{x_1})$ abbreviates the integrand from (2.16) and B_{δ_B} is a ball of radius δ_B around the point $\mathbf{x_1}$ (see Figure 3.4).

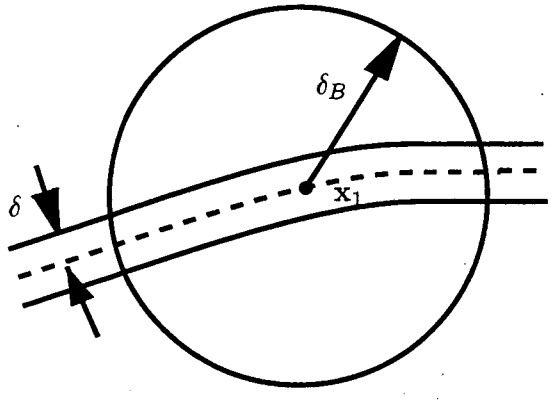

Figure 3.4: Local part around a point $\mathbf{x_1}$.

After lengthy manipulations one obtains

$$\mathbf{u} = \frac{\Gamma}{4\pi}\left[\ln(\frac{2\delta_B}{\delta}) - C\right]\kappa\mathbf{b} + \mathbf{Q}^{f,\perp} \tag{3.41}$$

with the use of (3.38). In equation (3.41), κ is the curvature of the filament, $\mathbf{Q}^{f,\perp}$ is the nonlocal contribution, and C is the core structure coefficient which can be evaluated with the physical vorticity components $\zeta^{(0)}$ and $\zeta_{11}^{(1)}$:

$$C = \frac{1}{2} + \frac{2\pi}{\Gamma}\int_0^\infty \left[\frac{1}{\kappa}\zeta_{11}^{(1)} + \bar{r}\ln\bar{r}\zeta^{(0)}\right] d\bar{r}. \tag{3.42}$$

Here $\zeta_{11}^{(1)}$ is the first cosine Fourier mode of $\zeta^{(1)}$ with respect to θ:

$$\zeta_{11}^{(1)} = \frac{1}{2\pi}\int_0^{2\pi} \zeta^{(1)}(\bar{r},\theta,s,t)\cos\theta d\theta. \tag{3.43}$$

In particular, C can be calculated by

$$C = -\lim_{r\to\infty}\left(\frac{4\pi^2}{\Gamma^2}\int_0^r r'\nu^{(0)^2}dr' - \ln r\right) + \frac{1}{2} \tag{3.44}$$

and the circumferential velocity $\nu^{(0)}$ is related to the leading order axial vorticity via $\bar{r}\zeta^{(0)} = (\bar{r}\nu^{(0)})_{\bar{r}}$.

Similarly,

$$\mathbf{u}^{\mathrm{ttm}} = \frac{\Gamma}{4\pi}\left(\ln\frac{2\delta_B}{\delta^{\mathrm{ttm}}} - C^{\mathrm{ttm}}\right)\kappa\mathbf{b} + \mathbf{Q}^{f,\perp} \tag{3.45}$$

where the superscripts "ttm" stands for *thin tube model*, δ^{ttm} is the numerical cutoff radius, and C^{ttm} is the numerical core structure coefficient which can be evaluated from (3.42) with the numerical vorticity components $\zeta^{(0),\mathrm{ttm}}$ and $\zeta_{11}^{(1),\mathrm{ttm}}$. Based on the numerical approximate vorticity distribution (3.28), one can derive explicit expressions for the numerical vorticity components $\zeta^{(0),\mathrm{ttm}}$ and $\zeta_{11}^{(1),\mathrm{ttm}}$, which are determined completely by the core smoothing function $f(r)$:

$$\zeta^{(0),\mathrm{ttm}}(\bar{r}) = \Gamma\int_{-\infty}^{\infty} f(\sqrt{\bar{r}^2+z^2})dz \tag{3.46}$$

$$\zeta_{11}^{(1),\mathrm{ttm}}(\bar{r}) = \frac{\Gamma\kappa}{2}\int_{-\infty}^{\infty}\frac{\bar{r}z^2}{\sqrt{\bar{r}^2+z^2}}f'(\sqrt{\bar{r}^2+z^2})dz. \tag{3.47}$$

Combining (3.41) and (3.45), one finds

$$\mathbf{u} = \mathbf{u}^{\mathrm{ttm}} + \frac{\Gamma}{4\pi}\left(C^{\mathrm{ttm}} - C + \ln\frac{\delta^{\mathrm{ttm}}}{\delta}\right)\kappa\mathbf{b} \tag{3.48}$$

which we shall call the *Klein-Knio equation.*

If δ^{ttm} is chosen to be δ, then

$$\mathbf{u} = \mathbf{u}^{\mathrm{ttm}} + \frac{\Gamma}{4\pi}\left(C^{\mathrm{ttm}} - C\right)\kappa\mathbf{b}. \tag{3.49}$$

Therefore, when we use the standard thin-tube model with $\delta^{\mathrm{ttm}} = \delta$, we have to add an explicit correction velocity to the numerical velocity $\mathbf{u}^{\mathrm{ttm}}$.

If δ^{ttm} is chosen so that $C^{\mathrm{ttm}} - C + \ln \frac{\delta^{\mathrm{ttm}}}{\delta} = 0$, then $\mathbf{u} = \mathbf{u}^{\mathrm{ttm}}$. In other words, if we use a rescaled numerical core radius $\delta^{\mathrm{ttm}} = \delta \exp(C - C^{\mathrm{ttm}})$, the standard thin-tube model can be applied directly without correction. This method is very attractive when δ is small and $\exp(C - C^{\mathrm{ttm}})$ is large. However, (3.48) is more general and is preferred when δ is extremely small.

3.4 Summary

We have introduced three different kinds of equations of motion for slender vortices: the local induction approximation, the Klein-Majda equation and the Klein-Knio equation.

The local induction approximation leads to elegant mathematics and its importance lies in making possible approximate calculations of the motion of arbitrary configurations of very thin vortex lines. However, it has serious flaws. First, it is a crude approximation, ignoring the nonlocal contribution. Second, it keeps the vortex length constant. Third, it allows unphysical behavior, such as vortex filaments passing through one another.

The Klein-Majda equation improves the local induction approximation in the sense that it takes vortex stretching into account. It uses a linear operator to approximate the nonlocal contribution. But the regime of applicability of the Klein-Majda equation is restricted to the small amplitude - short wavelength perturbations of a slender straight vortex filament. The vortex core structure is assumed to be frozen on the relevant time scales.

The Klein-Knio equation, based on the standard thin-tube model, may be better than the Klein-Majda equation since it approximates the nonlocal part accurately. It is applied to a slender vortex with leading order axisymmetric core structure.

It should be pointed out that all these three equations have assumed that the core size is very small in comparison with the radius of curvature. This assumption implies no folding. It may be that there is no folding for constant cross-section vortices.

To analyze these approximations, we will apply all of them to the same problem and see how they behave.

In the remainder of this chapter, we want to investigate the conservation laws for periodic flows and derive an expression for "energy" which can be used as a diagnostic in

our numerical experiments.

3.5 Conservation Laws for Periodic Boundary Conditions

Conservation laws are very useful in assessing the accuracy and consistency of numerical computations. We first review the conservation laws for three-dimensional unbounded flows, and after careful analysis we derive a new form of "energy" which is both conserved and finite for the unbounded flows with period L along the x-direction.

3.5.1 Conservation Laws for 3D Incompressible, Inviscid, Unbounded Flows

In what follows, the density is taken as one. In this subsection only three-dimensional unbounded flows with zero velocity and zero vorticity at infinity are considered. The total vorticity is therefore zero.

If the velocity field $\mathbf{u}$ is smooth, the Euler equations (2.1) and (2.2) have three linear invariants: the total vorticity $\mathbf{\Omega}$, linear impulse $\mathbf{I}$ and angular impulse $\mathbf{A}$ [9]

$$\mathbf{\Omega} = \int \omega d\mathbf{x} = 0, \tag{3.50}$$

$$\mathbf{I} = \frac{1}{2}\int \mathbf{x} \times \omega d\mathbf{x}, \tag{3.51}$$

$$\mathbf{A} = \frac{1}{3}\int \mathbf{x} \times (\mathbf{x} \times \omega) d\mathbf{x}, \tag{3.52}$$

as well as two quadratic invariants: kinetic energy E and helicity $\mathcal{H}$

$$E = \frac{1}{2}\int \mathbf{u} \cdot \mathbf{u} d\mathbf{x}, \tag{3.53}$$

$$\mathcal{H} = \int \omega \cdot \mathbf{u} d\mathbf{x}. \tag{3.54}$$

The conservation of helicity can be interpreted as the conservation of net linkage of vortex lines which move with the fluid [73].

3.5.2 Conservation Laws for Periodic Boundary Conditions

Sometimes we have to deal with flows which are periodic in the x-direction with period L and unbounded in the y and z directions (PBC for short).

In this case it is natural to consider a portion of space confined in one period of x:

$$W = \{(x, y, z) : 0 \leq x \leq L, -\infty < y, z < \infty\}. \tag{3.55}$$

The total vorticity in the given portion W does not vanish but is conserved in time.

$$\begin{aligned} \frac{d}{dt}\int_W \omega d\mathbf{x} &= \int_W \frac{\partial \omega}{\partial t} d\mathbf{x} \\ &= \int_W [(\omega \cdot \nabla)\mathbf{u} - (\mathbf{u} \cdot \nabla)\omega]\, d\mathbf{x} \end{aligned} \tag{3.56}$$

where the last equality has been obtained from the Euler equations (2.4). The following two facts are used repeatedly:

$$\int_W (\omega \cdot \nabla)\mathbf{a} = 0, \tag{3.57}$$

$$\int_W (\mathbf{u} \cdot \nabla)\mathbf{a} = 0, \tag{3.58}$$

for any vector $\mathbf{a}$ which is periodic with respect to x with period L.

The verification of (3.57) and (3.58) is straightforward. The j-th component of vector $(\omega \cdot \nabla)\mathbf{a}$ is

$$\omega_i \partial_i a_j = \partial_i(\omega_i a_j) \tag{3.59}$$

since $\partial_i \omega_i = 0$, where ω_i, a_j are components of ω and $\mathbf{a}$ respectively and there is summation over repeated indices. The integration of the j-th component of $(\omega \cdot \nabla)\mathbf{a}$ becomes

$$\begin{aligned} \int_W \partial_i(\omega_i a_j) d\mathbf{x} &= \int_W \nabla \cdot (\omega a_j) d\mathbf{x} \\ &= \int_{\mathbf{R}^2} \omega \cdot \mathbf{n} a_j |_{x=0}^{x=L} dA(y, z) \\ &= 0 \end{aligned} \tag{3.60}$$

using the periodicity of the integrand along x-direction. Therefore (3.57) holds. (3.58) can be proved in a similar way, noting that $\mathbf{u}$ is also divergence-free.

Selecting $\mathbf{a} = \mathbf{u}$ in (3.57) and $\mathbf{a} = \omega$ in (3.58) leads to

$$\frac{d}{dt}\int_W \omega d\mathbf{x} = 0. \tag{3.61}$$

So the total vorticity in the region W is conserved.

Proceeding now to the investigation of the linear impulse,

$$\frac{1}{2}\int_W \mathbf{x} \times \omega d\mathbf{x}, \tag{3.62}$$

one obtains

$$\begin{aligned}\frac{d}{dt}\int_W \mathbf{x}\times\omega d\mathbf{x} &= \int_W \mathbf{x}\times\frac{\partial\omega}{\partial t}d\mathbf{x}\\ &= \int_W \mathbf{x}\times[(\omega\cdot\nabla)\mathbf{u}-(\mathbf{u}\cdot\nabla)\omega]\,d\mathbf{x}. \end{aligned} \tag{3.63}$$

A simple computation shows that

$$\begin{aligned}\mathbf{x}\times[(\omega\cdot\nabla)\mathbf{u}] &= (\omega\cdot\nabla)(\mathbf{x}\times\mathbf{u})-(\omega\cdot\nabla)\mathbf{x}\times\mathbf{u}\\ &= (\omega\cdot\nabla)(\mathbf{x}\times\mathbf{u})-\omega\times\mathbf{u}. \end{aligned} \tag{3.64}$$

Employing the identity

$$\mathbf{u}\times\omega = \nabla(\frac{1}{2}\mathbf{u}^2)-(\mathbf{u}\cdot\nabla)\mathbf{u} \tag{3.65}$$

and applying (3.58) with $\mathbf{a}=\mathbf{u}$, we obtain

$$\int_W \mathbf{u}\times\omega d\mathbf{x} = 0. \tag{3.66}$$

Thus,

$$\int_W \mathbf{x}\times[(\omega\cdot\nabla)\mathbf{u}]\,d\mathbf{x} = \int_W(\omega\cdot\nabla)(\mathbf{x}\times\mathbf{u})d\mathbf{x}. \tag{3.67}$$

Similarly, we have

$$\int_W \mathbf{x}\times[(\mathbf{u}\cdot\nabla)\omega]\,d\mathbf{x} = \int_W(\mathbf{u}\cdot\nabla)(\mathbf{x}\times\omega)d\mathbf{x}. \tag{3.68}$$

Hence,

$$\frac{d}{dt}\int_W \mathbf{x}\times\omega d\mathbf{x} = \int_W[(\omega\cdot\nabla)(\mathbf{x}\times\mathbf{u})-(\mathbf{u}\cdot\nabla)(\mathbf{x}\times\omega)]\,d\mathbf{x}. \tag{3.69}$$

Using the summation convention and the divergence theorem, we find that the j-th component of the first integral is

$$\begin{aligned}\int_W \omega_i\partial_i(\mathbf{x}\times\mathbf{u})_j d\mathbf{x} &= \int_W \partial_i[\omega_i(\mathbf{x}\times\mathbf{u})_j]\,d\mathbf{x} \quad \text{since } \partial_i\omega_i = 0\\ &= \int_{\mathbf{R}^2}\omega\cdot\mathbf{n}(\mathbf{x}\times\mathbf{u})_j|_{x=0}^{x=L}dA(y,z), \end{aligned} \tag{3.70}$$

which does not vanish except when $\omega\cdot\mathbf{n}=0$ at the surfaces $x=0$ and $x=L$. Similarly, the j-th component of the second integral in (3.69) is

$$\int_{\mathbf{R}^2}\mathbf{u}\cdot\mathbf{n}(\mathbf{x}\times\omega)_j|_{x=0}^{x=L}dA(y,z), \tag{3.71}$$

which is non-zero except when $\mathbf{u}\cdot\mathbf{n}=0$ at the surfaces $x=0$ and $x=L$. Generally (3.70) and (3.71) cannot cancel each other. Hence the conditions

$$\omega\cdot\mathbf{n}=0 \text{ and } \mathbf{u}\cdot\mathbf{n}=0 \text{ at } x=0 \text{ and } x=L \tag{3.72}$$

are sufficient to ensure that the linear impulse is conserved. If the conditions (3.72) are not satisfied, the linear impulse in W can change according to (3.69).

The angular impulse is in general not invariant. From the vector identity

$$\mathbf{F} \times (\mathbf{G} \times \mathbf{H}) = (\mathbf{F} \cdot \mathbf{H})\mathbf{G} - \mathbf{H}(\mathbf{F} \cdot \mathbf{G}), \tag{3.73}$$

it is easy to show that

$$\begin{aligned}
&\frac{d}{dt}\int_W \mathbf{x} \times (\mathbf{x} \times \boldsymbol{\omega}) d\mathbf{x} = \int_W \mathbf{x} \times (\mathbf{x} \times \frac{\partial \boldsymbol{\omega}}{\partial t}) d\mathbf{x} \\
&= \int_W \mathbf{x} \times \{\mathbf{x} \times [(\boldsymbol{\omega} \cdot \bigtriangledown)\mathbf{u} - (\mathbf{u} \cdot \bigtriangledown)\boldsymbol{\omega}]\}\, d\mathbf{x} \\
&= \int_W [\mathbf{x} \cdot (\boldsymbol{\omega} \cdot \bigtriangledown)\mathbf{u} - \mathbf{x} \cdot (\mathbf{u} \cdot \bigtriangledown)\boldsymbol{\omega}]\, \mathbf{x} d\mathbf{x} + \int_W |\mathbf{x}|^2 [(\mathbf{u} \cdot \bigtriangledown)\boldsymbol{\omega} - (\boldsymbol{\omega} \cdot \bigtriangledown)\mathbf{u}]\, d\mathbf{x},
\end{aligned} \tag{3.74}$$

which is generally nonzero due to the appearance of $\mathbf{x}$ in the integrand.

The conservation of the helicity in W is now examined. We have

$$\begin{aligned}
&\frac{d}{dt}\int_W \boldsymbol{\omega} \cdot \mathbf{u} d\mathbf{x} = \int_W \left(\frac{\partial \boldsymbol{\omega}}{\partial t} \cdot \mathbf{u} + \boldsymbol{\omega} \cdot \frac{\partial \mathbf{u}}{\partial t}\right) d\mathbf{x} \\
&= \int_W \{[(\boldsymbol{\omega} \cdot \bigtriangledown)\mathbf{u} - (\mathbf{u} \cdot \bigtriangledown)\boldsymbol{\omega}] \cdot \mathbf{u} + \boldsymbol{\omega} \cdot [- \bigtriangledown P - (\mathbf{u} \cdot \bigtriangledown)\mathbf{u}]\}\, d\mathbf{x}.
\end{aligned} \tag{3.75}$$

Since

$$(\boldsymbol{\omega} \cdot \bigtriangledown)\mathbf{u} \cdot \mathbf{u} = \mathbf{u} \cdot (\boldsymbol{\omega} \cdot \bigtriangledown)\mathbf{u} = \boldsymbol{\omega} \cdot \bigtriangledown(\frac{1}{2}\mathbf{u}^2) \tag{3.76}$$

where $\mathbf{u}^2 = \mathbf{u} \cdot \mathbf{u}$, equation (3.75) becomes

$$\int_W \boldsymbol{\omega} \cdot \bigtriangledown(\frac{1}{2}\mathbf{u}^2 - P) d\mathbf{x} - \int_W [(\mathbf{u} \cdot \bigtriangledown)\boldsymbol{\omega} \cdot \mathbf{u} + \boldsymbol{\omega} \cdot (\mathbf{u} \cdot \bigtriangledown)\mathbf{u}]\, d\mathbf{x}. \tag{3.77}$$

In this expression, the first term vanishes since

$$\boldsymbol{\omega} \cdot \bigtriangledown(\frac{1}{2}\mathbf{u}^2 - P) = \bigtriangledown \cdot \left[\boldsymbol{\omega}(\frac{1}{2}\mathbf{u}^2 - P)\right] \tag{3.78}$$

using the fact that $\boldsymbol{\omega}$ is divergence-free. The second term also vanishes since

$$\begin{aligned}
(\mathbf{u} \cdot \bigtriangledown)\boldsymbol{\omega} \cdot \mathbf{u} + \boldsymbol{\omega} \cdot (\mathbf{u} \cdot \bigtriangledown)\mathbf{u} &= u_i \partial_i \omega_j u_j + \omega_j u_i \partial_i u_j \\
&= u_i \partial_i (u_j \omega_j) \\
&= \partial_i (u_i u_j \omega_j)
\end{aligned} \tag{3.79}$$

where the u_i, ω_i are the components of $\boldsymbol{\omega}$ and $\mathbf{u}$ respectively and the convention summation has been used. Thus, the helicity in W is time-invariant.

The investigation of the kinetic energy is more complicated. The usual expression for the kinetic energy in the restricted region W is

$$E_W = \int_0^L dx \int_{\mathbf{R}^2} dydz \frac{1}{2}\mathbf{u}^2 \tag{3.80}$$

which diverges. To see this, introduce

$$E(r) = \int_0^L \int_{|y-z|\leq r} \frac{1}{2}\mathbf{u}\cdot\mathbf{u}dxdydz. \tag{3.81}$$

Clearly,

$$E(r) \rightarrow E_W, \text{ as } r \rightarrow \infty. \tag{3.82}$$

One can show that $\frac{dE}{dt} \rightarrow 0$ but $E(r) \rightarrow \infty$ as $r \rightarrow \infty$. So E_W in (3.80) is not a good choice for a diagnostic.

Can we instead use the Lamb integral (2.13) to obtain a finite and conserved quantity ? The answer is "no" because $\mathbf{A}$ in (2.9) diverges. To see this intuitively, consider a straight vortex line along x-axis. At the point (0,0,1) we have $\mathbf{A} = \int_{-\infty}^{\infty} \frac{1}{4\pi\sqrt{x^2+1}}(1,0,0)dx$ which diverges.

Nevertheless, the procedure of deriving the Lamb integral sheds light on extracting a finite time-invariant form of "energy".

3.5.3 An Energy Expression for Periodic Boundary Conditions

Let $\mathbf{x} = (x, y, z)$. Define

$$\psi = \int_{\mathbf{R}^3} [\frac{1}{4\pi \mid \mathbf{x}-\mathbf{x}' \mid} - F(\mathbf{x}-\mathbf{x}')]\ \omega(\mathbf{x}')d\mathbf{x}' \tag{3.83}$$

where

$$F(\mathbf{x}) = \frac{1}{4\pi(\mid j \mid +1)L} \tag{3.84}$$

for

$$(j-\frac{1}{2})L \leq x < (j+\frac{1}{2})L. \tag{3.85}$$

One can check the following: for any $\mathbf{y}$,

$$\psi = \int_{\mathbf{R}^3} [\frac{1}{4\pi \mid \mathbf{x}-\mathbf{x}' \mid} - F(\mathbf{y}-\mathbf{x}')]\ \omega(\mathbf{x}')d\mathbf{x}'. \tag{3.86}$$

For computational purposes, we can rewrite $\psi(\mathbf{x})$ as follows.

Let $\mathbf{x} = (x, y, z)$, $\mathbf{x}' = (x', y', z')$. Define

$$a(\mathbf{x}) = \sum_{j=-\infty}^{+\infty} \left(\frac{1}{|\,\mathbf{x} - j(L,0,0)\,|} - \frac{1}{(|\,j\,|+1)L}\right). \tag{3.87}$$

From this $\psi(\mathbf{x})$ can be written as

$$\psi(\mathbf{x}) = \frac{1}{4\pi}\int_{x-\frac{L}{2}}^{x+\frac{L}{2}} dx' \int_{-\infty}^{\infty}\int_{-\infty}^{\infty} dy'dz'\ a(\mathbf{x}-\mathbf{x}')\omega(\mathbf{x}'). \tag{3.88}$$

A key property is the following:

Lemma 1 *If $\psi(\mathbf{x})$ is defined by (3.88), then it satisfies*

$$\nabla \times \psi(\mathbf{x}) = \mathbf{u}(\mathbf{x}), \tag{3.89}$$

$$\nabla \cdot \psi(\mathbf{x}) = 0. \tag{3.90}$$

The proof of the lemma is as follows:

$$\begin{aligned}
\frac{\partial \psi}{\partial x} &= \frac{1}{4\pi}\int_{x-\frac{L}{2}}^{x+\frac{L}{2}} dx' \int_{-\infty}^{\infty}\int_{-\infty}^{\infty} dy'dz' \frac{\partial}{\partial x} a(\mathbf{x}-\mathbf{x}')\omega(\mathbf{x}') \\
&+ \frac{1}{4\pi}\int_{-\infty}^{\infty}\int_{-\infty}^{\infty} dy'dz' a(\mathbf{x}-\mathbf{x}')\omega(\mathbf{x}')\Big|_{x'=x-\frac{L}{2}}^{x'=x+\frac{L}{2}} \\
&= \frac{1}{4\pi}\int_{x-\frac{L}{2}}^{x+\frac{L}{2}} dx' \int_{-\infty}^{\infty}\int_{-\infty}^{\infty} dy'dz' \frac{\partial}{\partial x} a(\mathbf{x}-\mathbf{x}')\omega(\mathbf{x}').
\end{aligned} \tag{3.91}$$

The second term vanishes because ω is periodic in x-direction and

$$a(x, y, z) = a(-x, y, z). \tag{3.92}$$

Similarly,

$$\frac{\partial \psi}{\partial y} = \frac{1}{4\pi}\int_{x-\frac{L}{2}}^{x+\frac{L}{2}} \int_{-\infty}^{\infty}\int_{-\infty}^{\infty} dx'dy'dz' \frac{\partial}{\partial y} a(\mathbf{x}-\mathbf{x}')\omega(\mathbf{x}'), \tag{3.93}$$

$$\frac{\partial \psi}{\partial z} = \frac{1}{4\pi}\int_{x-\frac{L}{2}}^{x+\frac{L}{2}} \int_{-\infty}^{\infty}\int_{-\infty}^{\infty} dx'dy'dz' \frac{\partial}{\partial z} a(\mathbf{x}-\mathbf{x}')\omega(\mathbf{x}'). \tag{3.94}$$

Furthermore,

$$\nabla \times \psi = \frac{1}{4\pi}\int_{x-\frac{L}{2}}^{x+\frac{L}{2}} \int_{-\infty}^{\infty}\int_{-\infty}^{\infty} dx'dy'dz' \mathrm{grad} a(\mathbf{x}-\mathbf{x}') \times \omega(\mathbf{x}'). \tag{3.95}$$

Since

$$\mathrm{grad}\ a(\mathbf{x}) = -\sum_{j=-\infty}^{+\infty} \frac{(x - jL, y, z)}{|\,\mathbf{x} - j(L,0,0)\,|^3}, \tag{3.96}$$

it follows that

$$\begin{aligned}\nabla \times \psi(\mathbf{x}) &= -\frac{1}{4\pi}\int_{x-\frac{L}{2}}^{x+\frac{L}{2}}\int_{-\infty}^{\infty}\int_{-\infty}^{\infty} dx'dy'dz' \sum_{j=-\infty}^{+\infty} \frac{(x-x'-jL, y-y', z-z')}{|\,\mathbf{x}-\mathbf{x}'-j(L,0,0)\,|^3} \times \omega(\mathbf{x}') \\ &= -\frac{1}{4\pi}\int_{\mathbf{R}^3} \frac{(\mathbf{x}-\mathbf{x}')\times\omega(\mathbf{x}')}{|\,\mathbf{x}-\mathbf{x}'\,|^3} d\mathbf{x}' \\ &= \mathbf{u}(\mathbf{x}). \end{aligned} \tag{3.97}$$

The last equality holds due to the Biot-Savart law.

In a similar fashion to the proof described above, one can show that $\nabla \cdot \psi(\mathbf{x}) = 0$.

□

With this lemma, it is straightforward to prove the following :

Theorem 3.5.1 *Define an energy as*

$$\begin{aligned} E &= \frac{1}{2}\int_0^L dx \int_{-\infty}^{\infty} dy \int_{-\infty}^{\infty} dz\ \psi(\mathbf{x})\cdot\omega(\mathbf{x}) \\ &= \frac{1}{8\pi}\int_0^L dx \int_{x-\frac{L}{2}}^{x+\frac{L}{2}} dx' \int_{-\infty}^{\infty}\int_{-\infty}^{\infty} dydz \int_{-\infty}^{\infty}\int_{-\infty}^{\infty} dy'dz' \\ &\sum_{j=-\infty}^{+\infty} \left(\frac{1}{|\,\mathbf{x}-\mathbf{x}'-j(L,0,0)\,|} - \frac{1}{(|\,j\,|+1)L}\right) \omega(\mathbf{x}')\cdot\omega(\mathbf{x}). \end{aligned} \tag{3.98}$$

Then E is time-invariant for smooth flow.

Proof.

$$\begin{aligned} \frac{dE}{dt} &= \frac{1}{8\pi}\int_0^L dx \int_{x-\frac{L}{2}}^{x+\frac{L}{2}} dx' \int_{-\infty}^{\infty}\int_{-\infty}^{\infty} dydz \int_{-\infty}^{\infty}\int_{-\infty}^{\infty} dy'dz' \\ &\sum_{j=-\infty}^{+\infty} \left(\frac{1}{|\,\mathbf{x}-\mathbf{x}'-j(L,0,0)\,|} - \frac{1}{(|\,j\,|+1)L}\right)\left(\frac{\partial\omega(\mathbf{x}')}{\partial t}\cdot\omega(\mathbf{x}) + \omega(\mathbf{x}')\cdot\frac{\partial\omega(\mathbf{x})}{\partial t}\right) \\ &= \frac{1}{4\pi}\int_0^L dx \int_{x-\frac{L}{2}}^{x+\frac{L}{2}} dx' \int_{-\infty}^{\infty}\int_{-\infty}^{\infty} dydz \int_{-\infty}^{\infty}\int_{-\infty}^{\infty} dy'dz' \\ &\sum_{j=-\infty}^{+\infty} \left(\frac{1}{|\,\mathbf{x}-\mathbf{x}'-j(L,0,0)\,|} - \frac{1}{(|\,j\,|+1)L}\right)\omega(\mathbf{x})\cdot\frac{\partial\omega(\mathbf{x}')}{\partial t} \end{aligned} \tag{3.99}$$

by changing the order of integration.

The vector identity

$$\mathrm{curl}(\mathbf{f}\times\mathbf{g}) = \mathbf{f}\mathrm{div}\mathbf{g} - \mathbf{g}\mathrm{div}\mathbf{f} + (\mathbf{g}\cdot\nabla)\mathbf{f} - (\mathbf{f}\cdot\nabla)\mathbf{g} \tag{3.100}$$

gives

$$\text{curl}(\mathbf{u}\times\boldsymbol{\omega}) = (\boldsymbol{\omega}\cdot\nabla)\mathbf{u} - (\mathbf{u}\cdot\nabla)\boldsymbol{\omega} \tag{3.101}$$

because $\text{div}\boldsymbol{\omega} = 0$, and because incompressibility gives $\text{div}\mathbf{u} = 0$. Hence

$$\frac{\partial\boldsymbol{\omega}}{\partial t} = \text{curl}(\mathbf{u}\times\boldsymbol{\omega}) \tag{3.102}$$

by the vorticity equation $\frac{\partial\boldsymbol{\omega}}{\partial t} = (\boldsymbol{\omega}\cdot\nabla)\mathbf{u} - (\mathbf{u}\cdot\nabla)\boldsymbol{\omega}$. Using the identity

$$\text{curl}\mathbf{f}\cdot\mathbf{g} = \text{div}(\mathbf{f}\times\mathbf{g}) + \mathbf{f}\cdot\text{curl}\mathbf{g} \tag{3.103}$$

and picking

$$\mathbf{f} = \mathbf{u}\times\boldsymbol{\omega}, \tag{3.104}$$

$$\mathbf{g} = \sum_{j=-\infty}^{+\infty}\left(\frac{1}{|\,\mathbf{x}-\mathbf{x}'-j(L,0,0)\,|} - \frac{1}{(|\,j\,|+1)L}\right)\boldsymbol{\omega}(\mathbf{x}), \tag{3.105}$$

we obtain

$$\begin{aligned}\frac{dE}{dt} &= \frac{1}{4\pi}\int_0^L dx\int_{x-\frac{L}{2}}^{x+\frac{L}{2}} dx'\int_{-\infty}^{\infty}\int_{-\infty}^{\infty} dydz\int_{-\infty}^{\infty}\int_{-\infty}^{\infty} dy'dz' \\ &\quad [\text{div}(\mathbf{f}\times\mathbf{g}) + \mathbf{f}\cdot\text{curl}\mathbf{g}] \\ &= \frac{1}{4\pi}\int_{\mathbf{x}} d\mathbf{x}\int_{\mathbf{x}'}\mathbf{f}\cdot\text{curl}\mathbf{g}\; d\mathbf{x}' \\ &= \int_{\mathbf{x}'}\mathbf{u}\times\boldsymbol{\omega}\cdot\mathbf{u}\; d\mathbf{x}' \\ &= 0\end{aligned} \tag{3.106}$$

by (3.89). □

In summary, in flows which are periodic in the x-direction and unbounded in the y and z directions, the total vorticity, helicity, and energy (3.98) are conserved quantities which can be used as checks on the numerical methods. If $\boldsymbol{\omega}\cdot\mathbf{n} = 0$ and $\mathbf{u}\cdot\mathbf{n} = 0$ at the boundaries of one period of x, linear impulse is also invariant. The angular impulse is not invariant in general.

Chapter 4

A Model Problem

Vortex waves are a very important phenomenon in the understanding of quantized vortex lines and have become a major preoccupation in superfluidity. In this chapter, we introduce a model problem which deals with vortex waves on quantized vortices in helium II, and which we shall use as a testbed for the methods we discussed. It has analytical stability results and we can use our methods to reproduce them.

This chapter is divided into three parts. The first part is concerned with explaining the model problem and defining the initial conditions and boundary conditions. A derivation of stability conditions for the local induction equation comprises part two. The final section of this chapter examines the stability conditions for the Klein-Majda equation.

4.1 A Model Problem

In order to study various numerical methods on the thin vortex simulation, we want to apply these methods to the same problem as studied in [94]. There are several reasons for us to select this model problem. First, the model problem deals with vortex waves on quantized vortices in helium II. Second, one can perform some theoretical analysis on the model problem. Third, the dynamical phenomena the model problem provides are very common and interesting.

In a situation in which an isolated vortex line is deformed into a helix, the deformation propagates as a wave which rotates about the axis of symmetry with a frequency given by Lord Kelvin [37]:

$$w = -\frac{\Gamma k^2}{4\pi}[ln(\frac{2}{ka}) - \gamma], \tag{4.1}$$

where Γ is the circulation, k is the wave number, a is the core size, γ is the Euler constant. When these helical waves are excited on a vortex line between fixed boundaries, two waves of opposite polarization combine to form a plane standing wave called a *Kelvin wave* which rotates with an angular velocity w given by (4.1). An interesting property of Kelvin waves reported in [94] is that they are unstable to the buildup of sidebands when the initial amplitude of the main helical wave is above a threshold amplitude at absolute zero temperature.

In the numerical simulations in the following chapters, we choose the same model problem as the one used by Samuels and Donnelly [94]. The initial conditions are chosen as a vortex line extended between two parallel planes 10^{-5} m apart and the vortex line being a superposition of a planar wave and two neighboring sidebands of small amplitude as a perturbation. In other words, the initial vortex filament can be expressed as a curve in three-dimensional space:

$$\begin{cases} x \in [0, L] \\ y = a_0 \cos(n_0 \pi x/L) + a_1 \cos(n_1 \pi x/L) + a_2 \cos(n_2 \pi x/L) \\ z = 0 \end{cases}$$

where $L = 10^{-5}$ m is the distance between two flat boundaries, n_0 is the number of half waves of the primary wave on the vortex, n_1 and n_2 are the numbers of half waves of the pair of nearest-neighbor sidebands (i.e. $n_1 = n_0 - 1$, $n_2 = n_0 + 1$), a_0, a_1 and a_2 are the initial amplitudes of the main wave and its sidebands. In our calculations in this thesis we set

$$a_1 = a_2 = 0.01 a_0, \tag{4.2}$$

and

$$n_0 = 11. \tag{4.3}$$

The boundary conditions are chosen so that the vortex line must meet the boundaries perpendicularly, and can slip along the boundaries. These conditions can be met by the method of images. By the method of images, we can extend the vortex filament between the walls and obtain periodic boundary conditions. The extension is illustrated by a simple example shown in Figure 4.1.

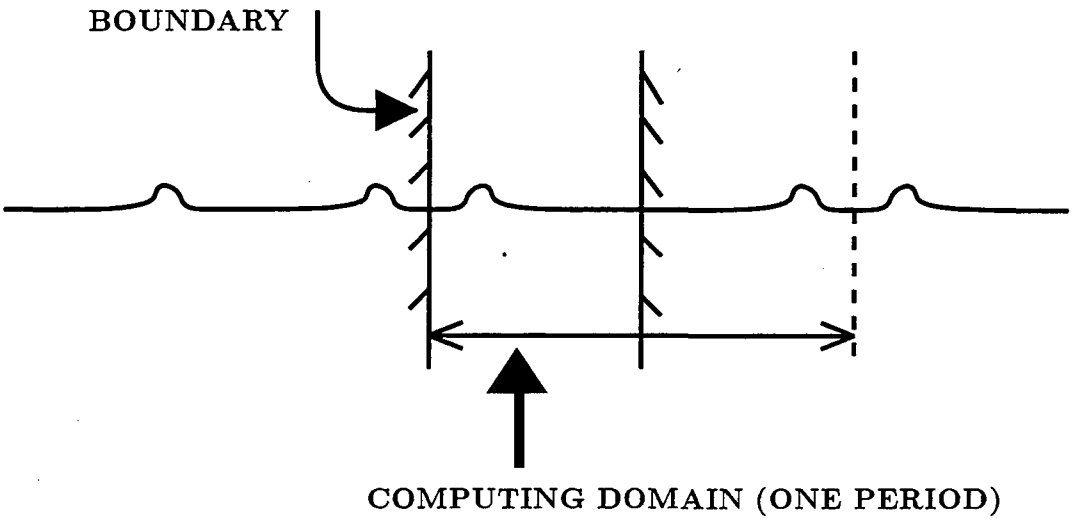

Figure 4.1: Extend a vortex filament between two planes by the method of images.

4.2 Linear Stability Analysis For LIA

In this section we perform a linear stability analysis on the sideband perturbation of Kelvin waves whose motion is described by the local induction equation.

Confining our attention to helical waves, we start by discussing stability conditions for filament function to simplify the analysis. We then go on to find the relationship between filament function perturbation and filament perturbation. This is followed by the derivation of stability conditions for helical waves. We end the section with stability conditions on the nearest-neighbor sideband perturbation of Kelvin waves.

4.2.1 Stability Conditions For the Filament Function of Helical Waves

To begin with, let us assume ϕ_H solves NLSE (3.15) exactly. Then, writing for simplicity

$$(\phi_H)_t = \frac{\partial \phi_H}{\partial t}, \ (\phi_H)_s = \frac{\partial \phi_H}{\partial s}, \text{ and } (\phi_H)_{ss} = \frac{\partial^2 \phi_H}{\partial s^2}, \tag{4.4}$$

we have

$$\frac{1}{i}(\phi_H)_t = (\phi_H)_{ss} + \frac{1}{2}|\phi_H|^2 \phi_H. \tag{4.5}$$

Substituting the perturbed solution

$$\phi(s,t) = \phi_H(,t)[1 + B(s,t)] \tag{4.6}$$

into the NLSE (3.15) gives

$$\frac{1}{i}(\phi_H)_t + \frac{1}{i}(\phi_H)_t B + \frac{1}{i}\phi_H B_t = (\phi_H)_{ss} + (\phi_H)_{ss} B + 2(\phi_H)_s B_s + \phi_H B_{ss} + \frac{1}{2}|\phi_H|^2\phi_H + \frac{1}{2}|\phi_H|^2\phi_H B + \frac{1}{2}|\phi_H|^2\phi_H(B + B^*). \tag{4.7}$$

Throughout this section the asterisk denotes the complex conjugate. By the use of equation (4.5) we obtain

$$\frac{1}{i}B_t = B_{ss} + 2\frac{(\phi_H)_s}{\phi_H}B_s + \frac{1}{2}|\phi_H|^2(B + B^*). \tag{4.8}$$

Assume ϕ_H is the exact oscillatory solution of the form

$$\phi_H(s,t) = A\exp(i[\xi s + \Omega t]), \tag{4.9}$$

where

$$\Omega = -\xi^2 + \frac{1}{2}A^2, \tag{4.10}$$

ξ, A are real-valued constants. From the definition of the filament function (3.16), one can see that the constant modulus $|\phi_H| = A$ corresponds to constant curvature of the filament and the constant wave number ξ implies a constant torsion. Constant curvature and torsion in turn define a helix configuration. Therefore, the formula (4.9) describes a family of helical waves. Under the assumption (4.9), one obtains

$$\frac{(\phi_H)_s}{\phi_H} = i\xi, \tag{4.11}$$

from which equation (4.8) reads

$$\frac{1}{i}B_t = B_{ss} + 2i\xi B_s + \frac{1}{2}|A|^2(B + B^*). \tag{4.12}$$

Furthermore, assume

$$B = \alpha_1(t)\psi_1(s) + \alpha_2(t)\psi_2(s), \tag{4.13}$$

where the complex variables $\alpha_1(t)$, $\alpha_2(t)$ remain to be determined, and $\psi_1(s)$, $\psi_2(s)$ are defined by

$$\psi_1(s) = \exp(i\beta s), \tag{4.14}$$

$$\psi_2(s) = \exp(-i\beta s) = \psi_1^*. \tag{4.15}$$

Let us now derive some useful relations. Three differentiations of (4.13) yield

$$B_t = \alpha_1'(t)\psi_1 + \alpha_2'(t)\psi_2, \tag{4.16}$$

$$B_{ss} = -\beta^2\alpha_1(t)\psi_1 - \beta^2\alpha_2(t)\psi_2, \tag{4.17}$$

$$2i\xi B_s = -2\xi\beta\alpha_1(t)\psi_1 + 2\xi\beta\alpha_2(t)\psi_2. \tag{4.18}$$

Substitutions from (4.16), (4.17) and (4.18) into (4.12) lead to

$$\begin{aligned}\frac{1}{i}[\alpha_1'(t)\psi_1 + \alpha_2'(t)\psi_2] &= -\beta^2\alpha_1(t)\psi_1 - \beta^2\alpha_2(t)\psi_2 - 2\xi\beta\alpha_1(t)\psi_1 \\ &+2\xi\beta\alpha_2(t)\psi_2 + \frac{1}{2}|A|^2[\alpha_1(t)\psi_1 + \alpha_1^*(t)\psi_2 + \alpha_2(t)\psi_2 + \alpha_2^*(t)\psi_1]\end{aligned} \tag{4.19}$$

with some use of (4.15). Setting the coefficients of ψ_1 and the coefficients ψ_2 to be zero, we obtain successively

$$\alpha_1'(t) = i[-\beta^2\alpha_1(t) - 2\xi\beta\alpha_1(t) + \frac{1}{2}|A|^2\alpha_1(t) + \frac{1}{2}|A|^2\alpha_2^*(t)], \tag{4.20}$$

$$\alpha_2'(t) = i[-\beta^2\alpha_2(t) + 2\xi\beta\alpha_2(t) + \frac{1}{2}|A|^2\alpha_2(t) + \frac{1}{2}|A|^2\alpha_1^*(t)]. \tag{4.21}$$

Taking complex conjugate of equation (4.21) gives

$$\alpha_2'^*(t) = -i[-\beta^2\alpha_2^*(t) + 2\xi\beta\alpha_2^*(t) + \frac{1}{2}|A|^2\alpha_1(t) + \frac{1}{2}|A|^2\alpha_2^*(t)]. \tag{4.22}$$

We can combine equations (4.20) and (4.22) into a matrix form:

$$\frac{d}{dt}\begin{pmatrix}\alpha_1(t)\\ \alpha_2^*(t)\end{pmatrix} = \begin{bmatrix} -i(\beta^2 + 2\xi\beta - \frac{1}{2}|A|^2) & \frac{i}{2}|A|^2 \\ -\frac{i}{2}|A|^2 & i(\beta^2 - 2\xi\beta - \frac{1}{2}|A|^2)\end{bmatrix}\begin{bmatrix}\alpha_1(t)\\ \alpha_2^*(t)\end{bmatrix}. \tag{4.23}$$

By introducing some notations:

$$a = \frac{1}{2}|A|^2, \tag{4.24}$$

$$b = -2\xi\beta, \tag{4.25}$$

$$c = \beta^2 - \frac{1}{2}|A|^2, \tag{4.26}$$

we can simplify the matrix in (4.23) to

$$\begin{aligned} M &= \begin{bmatrix} -i(\beta^2 + 2\xi\beta - \frac{1}{2}|A|^2) & \frac{i}{2}|A|^2 \\ -\frac{i}{2}|A|^2 & i(\beta^2 - 2\xi\beta - \frac{1}{2}|A|^2)\end{bmatrix} \\ &= \begin{bmatrix} i(b-c) & ia \\ -ia & i(b+c)\end{bmatrix} \\ &= i\left[bI + \begin{pmatrix} -c & a \\ -a & c\end{pmatrix}\right] \\ &\equiv i(bI + M_2). \end{aligned} \tag{4.27}$$

When $c^2 \geq a^2$, the matrix M_2 has two real eigenvalues

$$\lambda_{1,2} = \pm\sqrt{c^2 - a^2}. \tag{4.28}$$

Therefore, the two eigenvalues of M are

$$\tilde{\lambda}_1 = i(b + \sqrt{c^2 - a^2}), \tag{4.29}$$

$$\tilde{\lambda}_2 = i(b - \sqrt{c^2 - a^2}), \tag{4.30}$$

thereby showing that the two modes $\alpha_1(t)$ and $\alpha_2(t)$ remain bounded and the perturbation is stable.

When $c^2 < a^2$, M_2 has two imaginary eigenvalues

$$\lambda_1 = i\sqrt{a^2 - c^2},\ \lambda_2 = -i\sqrt{a^2 - c^2} \tag{4.31}$$

with the corresponding eigenvectors

$$\mathbf{v}_1 = \begin{pmatrix} 1 \\ \frac{c+i\sqrt{a^2-c^2}}{a} \end{pmatrix} \text{ and } \mathbf{v}_2 = \begin{pmatrix} 1 \\ \frac{c-i\sqrt{a^2-c^2}}{a} \end{pmatrix}. \tag{4.32}$$

The two eigenvalues of M are given by

$$\tilde{\lambda}_1 = i(b + i\sqrt{a^2 - c^2}) = ib - \sqrt{a^2 - c^2}, \tag{4.33}$$

$$\tilde{\lambda}_2 = i(b - i\sqrt{a^2 - c^2}) = ib + \sqrt{a^2 - c^2}, \tag{4.34}$$

and the solution to (4.23) by

$$\begin{pmatrix} \alpha_1(t) \\ \bar{\alpha}_2(t) \end{pmatrix} = c_1 e^{(ib-\sqrt{a^2-c^2})t}\mathbf{v}_1 + c_2 e^{(ib+\sqrt{a^2-c^2})t}\mathbf{v}_2, \tag{4.35}$$

where c_1 and c_2 are some constants.

Clearly, as $t \to \infty$,

$$|e^{(ib-\sqrt{a^2-c^2})t}| \to 0, \tag{4.36}$$

$$|e^{(ib+\sqrt{a^2-c^2})t}| \to \infty, \tag{4.37}$$

indicating that $\alpha_2(t)$ grows exponentially with respect to time and hence the perturbation is unstable.

Noting that $c^2 < a^2$ is equivalent to $-|A| < \beta < |A|$, we now arrive at the following theorem:

Theorem 4.2.1 *Assume ϕ_H is an exact solution of NLSE (3.15) and*

$$\phi_H(s,t) = A\exp(i[\xi s + \Omega t]) \tag{4.38}$$

where A, ξ are real-valued constants. If

$$\phi(s,t) = \phi_H\left[1 + \alpha_1(t)\exp(i\beta s) + \alpha_2(t)\exp(-i\beta s)\right] \tag{4.39}$$

where β is a real constant, and $\alpha_1(t)$, $\alpha_2(t)$ are complex variables, then the perturbation in (4.39) is unstable for $-|A| < \beta < |A|$. Here by the word "unstable" we mean the existence of exponentially growing modes.

The instabilities described by (4.39) are usually called *modulational instabilities* or *Benjamin-Feir instabilities.* Benjamin-Feir [14] showed that finite-amplitude waves on deep water are unstable to perturbations in the sideband waves. Later this was found to be a general property of the solutions of the the nonlinear Schrödinger equation [117]. The Benjamin-Feir instabilities appear in many hydrodynamic and related systems such as Taylor-Couette flow, shear flow, thin film flows and reaction-diffusion systems.

In the model problem, we have a superposition of helical waves instead of a superposition of filament functions. A relationship between these two needs to be found before employing Theorem 4.2.1.

4.2.2 Relationship Between Filament Perturbation and Filament Function Perturbation of Helical Waves

Consider two helical waves

$$\mathbf{r}_1 = \begin{bmatrix} a_1\cos(b_1 t) \\ a_1\sin(b_1 t) \\ t \end{bmatrix}, \tag{4.40}$$

and

$$\mathbf{r}_2 = \begin{bmatrix} a_2\cos(b_2 t + c_2) \\ a_2\sin(b_2 t + c_2) \\ t \end{bmatrix}, \tag{4.41}$$

where

$$b_2 = O(1)b_1,\ \ a_2 = \varepsilon a_1,\ \ \varepsilon << 1. \tag{4.42}$$

The superposition of (4.40) and (4.41) is

$$\mathbf{r} = \begin{bmatrix} a_1\cos(b_1t) + a_2\cos(b_2t + c_2) \\ a_1\sin(b_1t) + a_2\sin(b_2t + c_2) \\ t \end{bmatrix}. \tag{4.43}$$

After brief algebra, we obtain

$$\mathbf{r}'(t) \times \mathbf{r}''(t) = \begin{bmatrix} a_1b_1^2\sin(b_1t) + a_2b_2^2\sin(b_2t + c_2) \\ -a_1b_1^2\cos(b_1t) - a_2b_2^2\cos(b_2t + c_2) \\ a_1^2b_1^3 + a_2^2b_2^3 + a_1b_1a_2b_2(b_1 + b_2)\cos[(b_2 - b_1)t + c_2] \end{bmatrix}. \tag{4.44}$$

With the aid of (4.42) one finds the curvature κ of (4.43)

$$\begin{aligned} \kappa &= \frac{|\mathbf{r}'(t) \times \mathbf{r}''(t)|}{|\mathbf{r}'(t)|^3} \\ &= \frac{a_1b_1^2}{1 + a_1^2b_1^2}\left\{1 + \varepsilon[\frac{b_2^2}{b_1^2} - 2\frac{a_1^2b_1b_2}{1 + a_1^2b_1^2}]\cos[(b_2 - b_1)t + c_2]\right\} + O(\varepsilon^2), \end{aligned} \tag{4.45}$$

and the torsion τ

$$\begin{aligned} \tau &= \frac{(\mathbf{r}'(t) \times \mathbf{r}''(t)) \cdot \mathbf{r}'''(t)}{|\mathbf{r}'(t) \times \mathbf{r}''(t)|^2} \\ &= \frac{b_1}{1 + a_1^2b_1^2}\left\{1 + \varepsilon[\frac{b_2^2(b_2 - b_1)}{b_1^3} - 2\frac{a_1^2b_1b_2}{1 + a_1^2b_1^2}]\cos[(b_2 - b_1)t + c_2]\right\} + O(\varepsilon^2). \end{aligned} \tag{4.46}$$

By picking $\varepsilon = 0$ in (4.45) and (4.46), we obtain the curvature κ_1 and torsion τ_1 of (4.40):

$$\kappa_1 = \frac{a_1b_1^2}{1 + a_1^2b_1^2}, \tag{4.47}$$

$$\tau_1 = \frac{b_1}{1 + a_1^2b_1^2}. \tag{4.48}$$

Changing the subscript 1 into 2, we have the curvature κ_2 and torsion τ_2 of (4.41):

$$\kappa_2 = \frac{a_2b_2^2}{1 + a_2^2b_2^2}, \tag{4.49}$$

$$\tau_2 = \frac{b_2}{1 + a_2^2b_2^2}. \tag{4.50}$$

For comparison purposes, we want to represent κ and τ in terms of the arc length s. Note that the arc length $s(t)$ is given by

$$\begin{aligned} s(t) &= \int_0^t |\mathbf{r}'(t)|dt \\ &= \int_0^t (1 + a_1^2b_1^2)^{1/2}\left\{1 + \frac{\varepsilon a_1^2b_1b_2}{1 + a_1^2b_1^2}\cos[(b_2 - b_1)\tilde{t} + c_2] + O(\varepsilon^2)\right\}d\tilde{t} \\ &= (1 + a_1^2b_1^2)^{1/2}(1 + O(\varepsilon))t, \end{aligned} \tag{4.51}$$

so we can rewrite (4.45) and (4.46) in terms of s provided $|t| \leq O(1)$ (i.e. t not far from 0):

$$\kappa = \frac{a_1 b_1^2}{1+a_1^2 b_1^2}\left\{1+\varepsilon[\frac{b_2^2}{b_1^2}-2\frac{a_1^2 b_1 b_2}{1+a_1^2 b_1^2}]\cos[\frac{(b_2-b_1)s}{(1+a_1^2 b_1^2)^{1/2}}+c_2]\right\}+O(\varepsilon^2), \quad (4.52)$$

$$\tau = \frac{b_1}{1+a_1^2 b_1^2}\left\{1+\varepsilon[\frac{b_2^2(b_2-b_1)}{b_1^3}-2\frac{a_1^2 b_1 b_2}{1+a_1^2 b_1^2}]\cos[\frac{(b_2-b_1)s}{(1+a_1^2 b_1^2)^{1/2}}+c_2]\right\}+O(\varepsilon^2). \quad (4.53)$$

Next we think about the perturbation of the filament function. Keeping the definition of filament function in mind, the corresponding filament functions of (4.40) and (4.41) are

$$\phi_1 = \kappa_1 \exp(i\tau_1 s), \quad (4.54)$$

$$\phi_2 = \kappa_2 \exp(i\tau_2 s + c_2). \quad (4.55)$$

The superposition of these two filament function is

$$\phi = [\kappa_1 \cos(\tau_1 s) + \kappa_2 \cos(\tau_2 s + c_2)] + i[\kappa_1 \sin(\tau_1 s) + \kappa_2 \sin(\tau_2 s + c_2)]. \quad (4.56)$$

On the other hand, recalling the definition of the filament function (3.16) again, we can write

$$\phi = \kappa(s)\exp(i\int_0^s \tau(\sigma)d\sigma), \quad (4.57)$$

where $\kappa(s)$ and $\tau(s)$ are the curvature and torsion of the filament whose corresponding filament function is given by (4.56). Using (4.56) and (4.57), one obtains an expression for κ:

$$\begin{aligned}\kappa(s) &= |\phi| \\ &= \kappa_1\left\{1+\frac{\kappa_2}{\kappa_1}\cos[(\tau_2-\tau_1)s+c_2]\right\}+O(\varepsilon^2)]. \end{aligned} \quad (4.58)$$

To find $\tau(s)$, we differentiate (4.57) with respect to s:

$$\begin{aligned}\phi_s &= \kappa'(s)\exp(i\int_0^s \tau(\eta)d\eta)+\kappa(s)\exp(i\int_0^s \tau(\eta)d\eta)i\tau(s) \\ &= \phi(\frac{\kappa'(s)}{\kappa(s)}+i\tau(s)), \end{aligned} \quad (4.59)$$

which leads to

$$\frac{\phi^*\phi_s}{|\phi|^2} = \frac{\kappa'(s)}{\kappa(s)}+i\tau(s). \quad (4.60)$$

Through equation (4.56), this identity yields

$$\begin{aligned}\tau(s) &= \text{Imag}\left[\frac{\phi^*\phi_s}{|\phi|^2}\right] \\ &= \tau_1\left\{1+\frac{\tau_2-\tau_1}{\tau_1}\frac{\kappa_2}{\kappa_1}\cos[(\tau_2-\tau_1)s+c_2]\right\}+O(\varepsilon^2). \qquad (4.61)\end{aligned}$$

Collecting (4.42), (4.47), (4.48), (4.49), (4.50), (4.58) and (4.61), one finally finds

$$\kappa(s) = \frac{a_1 b_1^2}{1+a_1^2 b_1^2}\left\{1+\varepsilon\frac{b_2^2}{b_1^2}\cos[(b_2-b_1)s+c_2]\right\}+O(\varepsilon^2), \qquad (4.62)$$

$$\tau(s) = \frac{b_1}{1+a_1^2 b_1^2}\left\{1+\varepsilon\frac{b_2^2(b_2-b_1)}{b_1^3}\cos[(b_2-b_1)s+c_2]\right\}+O(\varepsilon^2). \qquad (4.63)$$

Obviously, (4.62) and (4.63) coincide with (4.52) and (4.53) to leading order.

Therefore, we can conclude that

Theorem 4.2.2 *Suppose we have two helical waves H_1 and H_2 with corresponding filament functions:*

$$\phi_1 = \kappa_1 \exp(i\int_0^s \tau_1 d\eta), \qquad (4.64)$$

$$\phi_2 = \kappa_2 \exp(i\int_0^s \tau_2 d\eta), \qquad (4.65)$$

where $\kappa_2 = O(\varepsilon)\kappa_1$, $\varepsilon << 1$, τ_1 and τ_2 are of the same order. Let $\tilde{\kappa}$ and $\tilde{\tau}$ be the the curvature and torsion of the superposition of H_1 and H_2, κ and τ the curvature and torsion of the filament whose filament function is given by $\phi = \phi_1 + \phi_2$. Then under certain conditions,

$$\tilde{\kappa} = \kappa + O(\varepsilon^2), \qquad (4.66)$$

$$\tilde{\tau} = \tau + O(\varepsilon^2). \qquad (4.67)$$

Theorem 4.2.2 tells us that the superposition of helical waves is approximately equivalent to the superposition of the corresponding filament functions. Now we can derive the stability condition for helical waves.

4.2.3 Stability Conditions For Helical Waves

Consider a helical wave in the form of

$$\mathbf{r}(r) = \begin{bmatrix} a\cos(\frac{n\pi t}{L}) \\ a\sin(\frac{n\pi t}{L}) \\ t \end{bmatrix}. \qquad (4.68)$$

Straightforward manipulations yield its curvature κ and torsion τ:

$$\kappa = \frac{a(\frac{2\pi}{\lambda})^2}{1+(\frac{2\pi}{\lambda})^2} = a(\frac{2\pi}{\lambda})^2\left[1+O((a\frac{2\pi}{\lambda})^2)\right], \tag{4.69}$$

$$\tau = \frac{a^2(\frac{2\pi}{\lambda})^5}{a^2(\frac{2\pi}{\lambda})^4(1+a^2(\frac{2\pi}{\lambda})^2} = \frac{2\pi}{\lambda}\left[1-O((a\frac{2\pi}{\lambda})^2)\right], \tag{4.70}$$

where $\lambda = \frac{2L}{n}$ is the wavelength. When $a\frac{2\pi}{\lambda}$ is small, we have approximately

$$\kappa = a(\frac{2\pi}{\lambda})^2, \tag{4.71}$$

$$\tau = \frac{2\pi}{\lambda}. \tag{4.72}$$

For the nearest-neighbor sideband perturbation of (4.68), β and A in Theorem 4.2.1 are

$$\beta = \frac{\pi}{L} = \frac{2\pi}{n\lambda}, \ A = \kappa = a(\frac{2\pi}{\lambda})^2. \tag{4.73}$$

Therefore the stability condition is

$$a(\frac{2\pi}{\lambda})^2 < \frac{2\pi}{n\lambda}, \tag{4.74}$$

i.e.

$$\frac{a}{\lambda} < \frac{1}{2\pi n}. \tag{4.75}$$

Since a cosine wave is a superposition of two helical waves, the amplitude of the cosine wave is twice as large as the original helical waves. Hence under the assumption that the vortex motion is controlled by the local induction equation we derive the *stability condition for the model problem*:

$$\frac{a_0}{\lambda} < \frac{1}{\pi n}, \tag{4.76}$$

where a_0 is the amplitude of the main wave, λ the wavelength, n the number of half waves.

4.3 Linear Stability Analysis For The Klein-Majda Equation

In this section we carry out a linear stability analysis on the sideband perturbation of Kelvin waves whose filament function obeys the Klein-Majda equation. The analysis below follows the template of [60].

Suppose the exact solution of (3.25) is of the form

$$\phi_H(\sigma,\tau) = A \ \exp(i[\xi\sigma+\Omega\tau]) \tag{4.77}$$

where Ω satisfies the dispersion relation

$$\Omega(\xi, A, \varepsilon) = -\xi^2 - \varepsilon^2 \hat{I}(\xi) + \frac{1}{2}\varepsilon^2 A^2. \tag{4.78}$$

Consider

$$\phi(\sigma, \tau) = \phi_H(\sigma, \tau)\ [1 + b\ exp(i(\beta\sigma + \alpha\tau))] \tag{4.79}$$

where $0 < b \leq 1$ and β are real-valued constants and the complex time exponent α remains to be determined. Substitute the expression (4.79) into the Klein-Majda equation (3.25). Such a procedure gives rise to the exact dispersion relation

$$\alpha_{1/2} = -2\xi\beta - \varepsilon^2 \Delta\hat{I}(\beta, \xi) \pm \sqrt{[F(\beta, \xi, \varepsilon) - a]^2 - a^2}, \tag{4.80}$$

where

$$\begin{aligned} F(\beta, \xi, \varepsilon) &= \beta^2 + \varepsilon^2 \Delta^2 \hat{I}(\beta, \xi), & (4.81)\\ \Delta\hat{I}(\beta, \xi) &= \frac{1}{2}[\hat{I}(\beta + \xi) - \hat{I}(\beta - \xi)], & (4.82)\\ \Delta^2\hat{I}(\beta, \xi) &= \frac{1}{2}[\hat{I}(\beta + \xi) + \hat{I}(\beta - \xi) - 2\hat{I}(\xi)], & (4.83)\\ a &= \frac{1}{2}\varepsilon^2 A^2. & (4.84) \end{aligned}$$

Therefore, the stability properties of the helix solutions are displayed by the functions

$$G(\beta, \xi, A, \varepsilon) = \text{sign}(R)\sqrt{|R|} \tag{4.85}$$

with

$$\begin{aligned} R^{\text{KM}} &= (F - \frac{1}{2}\varepsilon^2 A^2)^2 - (\frac{1}{2}\varepsilon^2 A^2)^2, & (4.86)\\ R^{\text{NLS}} &= (\beta^2 - \frac{1}{2}\varepsilon^2 A^2)^2 - (\frac{1}{2}\varepsilon^2 A^2)^2. & (4.87) \end{aligned}$$

Here "NLS" represents the equation (3.25) with $I = 0$. Note that it is slightly different from (3.15) with $\varepsilon^2/2$ instead of $1/2$ being the coefficient of the cubic term. However, it can be reduced to a form of (3.15) with a rescaling of $\tau \to \varepsilon^2\tau$ and $\sigma \to \varepsilon\sigma$. Clearly, instability occurs for negative radicands R.

In Figure 4.2 we plot the growth rate G against the amplitude A for sideband perturbations for the filament function with different values of ε: $\varepsilon = 0.5$, 0.309, 0.2 and 0.1. The solid curve denotes the KM model, while the dotted curve denotes the NLS model. As $\varepsilon = 0.5$, the KM model always gives stability; As $\varepsilon = 0.309$, the KM model has a smaller

stability region than that of the NLS model; As ε gets smaller, the stability region of the KM model converges to that of the NLS model. Furthermore, in the regions where both the KM model and the NLS model are unstable, the growth rate of NLS model is slightly bigger than that of KM model. Therefore, one can conclude that the stability region of the KM model depends dramatically on the core coefficient ε. And surprisingly, for ε large enough, the KM model is always more stable than the NLS model. Here it should be pointed out that we have rescaled the growth rate G so that it will not depend on ε for the NLS model.

For the model problem, the Kelvin waves are superposed by two helical waves initially. As shown in (4.71), the curvature κ and the amplitude A of a helical wave is related by

$$\kappa = A(\frac{2\pi}{\lambda})^2 = \frac{a_0}{2}(\frac{2\pi}{\lambda})^2, \tag{4.88}$$

where a_0 is the amplitude of the main cosine wave. From (4.88), we can obtain stability diagram for the model problem. We plot the growth rate G vs a_0/λ in Figure 4.3 for different values of ε: $\varepsilon = 0.5$, 0.48, 0.4778, 0.4775, 0.35, 0.309, 0.1, and 0.01, respectively. The solid lines are for the KM model and the dashed lines are for the NLS model. As shown in Figure 4.3, the KM model is always stable when $\varepsilon \geq 0.4778$. This conclusion, in this specific setting, is at variance with some of the conjectures in Klein-Majda [60]. Once $\varepsilon \leq 0.4775$, this is no longer true and the stability region of the KM model is smaller than that of the NLS model. However, as ε decreases the stability region of the KM model eventually coincides with that of the NLS model.

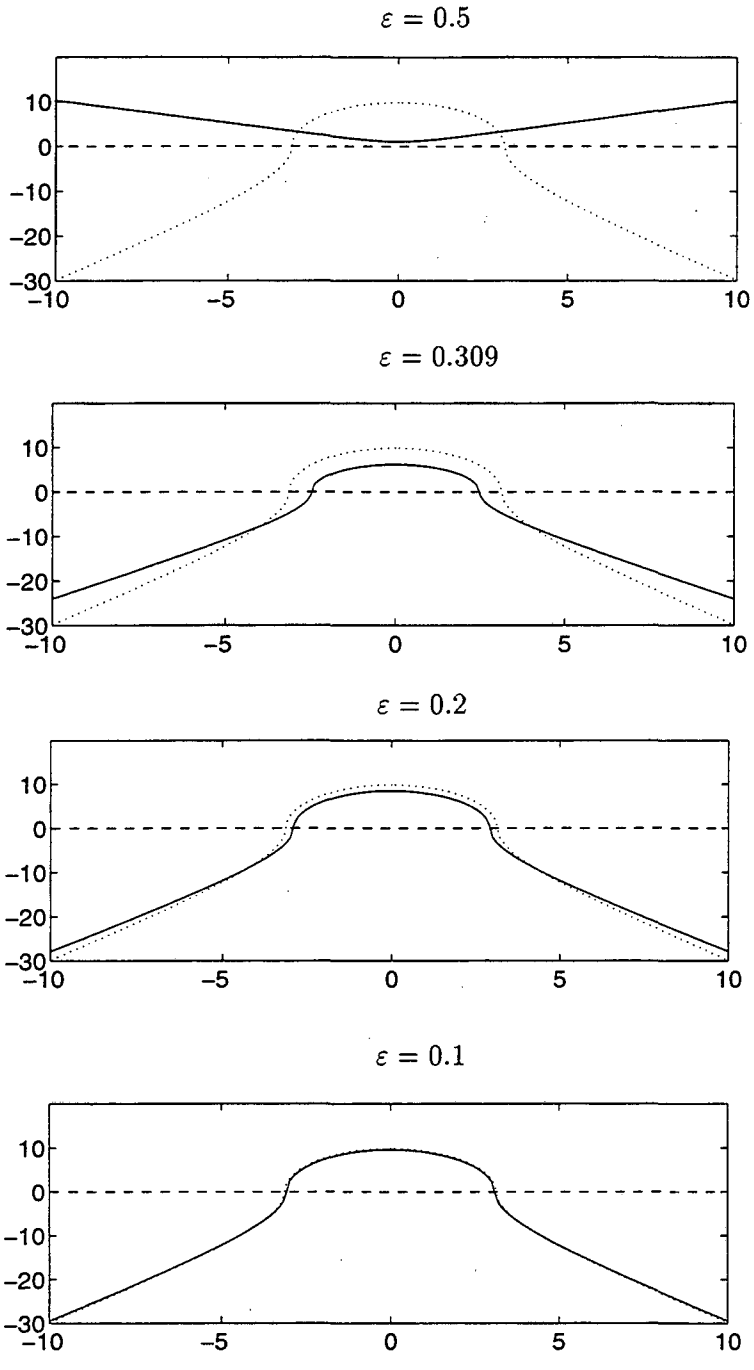

Figure 4.2: Stability diagram for sideband perturbations for the filament function of helical waves. The solid lines are for the Klein-Majda model and the dotted lines are for the NLS model. The horizontal axis is the initial amplitude of the filament function of the helical wave, and the vertical axis is the growth rate G. Instability occurs for negative G.

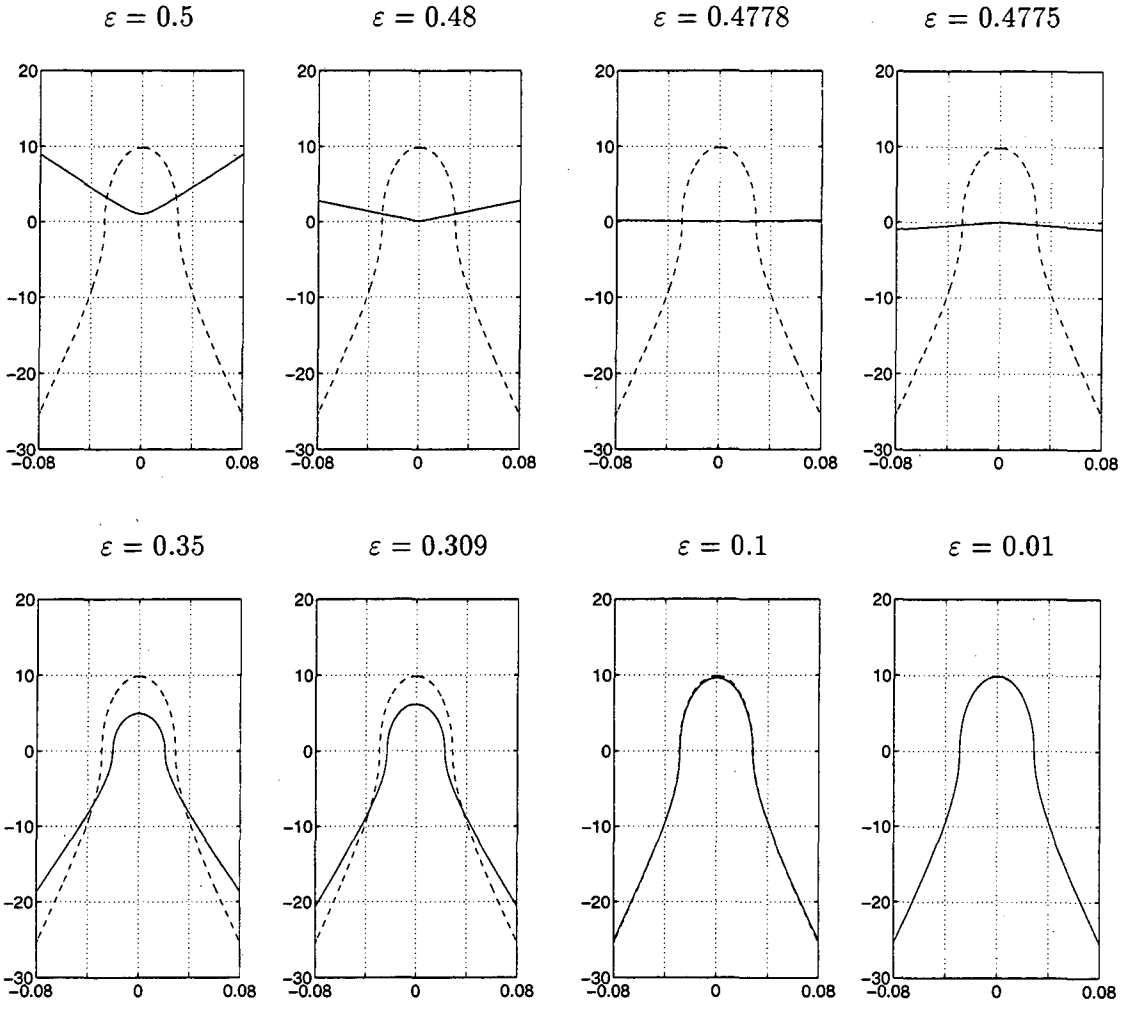

Figure 4.3: Stability diagram for the vortex filament of our model problem. The solid lines are for the Klein-Majda model and the dashed lines are for the NLS model. The horizontal axis is a_0/λ, where a_0 is the initial amplitude of the main cosine wave, λ is the wavelength. The vertical axis is the growth rate G. Instability happens for $G < 0$.

Chapter 5

Numerical Comparison of Thin Vortex Models

The goal of this chapter is to present numerical methods for solving the local induction equation, the Klein-Majda equation and the Klein-Knio equation, and then compare the numerical results when applying all equations to the same model problem.

In the first section we review the method developed by Buttke which approximates the local induction equation. This method is stable and can be designed to be second-order or fourth-order accurate. In the second section a fractional step method is introduced to solve the Klein-Majda equation for the filament function. Once the filament function is found, we give a procedure to recover the filament curve from the filament function. The details of our computational technique for the Klein-Knio equation are described in the third section. It is a hybrid of a fractional step method and a high order Runge-Kutta method. In the fourth section we attempt to evaluate the energy. In the last section we present the numerical results by applying all methods to the model problem introduced in the previous chapter.

5.1 Numerical Scheme for the Local Induction Equation

To solve the local induction equation (LIA), we present a numerical method due to Buttke [17] which is based on equation (3.12). For a more detailed mathematical treatment of such issues as proof of stability, consistency and convergence, see Buttke [16].

Let $\mathbf{t}_j^n$ denote the approximation to $\mathbf{t}(j\Delta s, n\Delta t)$. Buttke developed a Crank-

Nicholson type scheme (Figure 5.1):

$$\mathbf{t}_j^{n+1} - \mathbf{t}_j^n = \frac{\Delta t}{4(\Delta s)^2} (\mathbf{t}_j^{n+1} + \mathbf{t}_j^n) \times (\mathbf{t}_{j+1}^{n+1} + \mathbf{t}_{j-1}^{n+1} + \mathbf{t}_{j+1}^n + \mathbf{t}_{j-1}^n) \tag{5.1}$$

where Δs is the spatial increment, Δt is the temporal increment and the term $\mathbf{t}_j^{n+1} + \mathbf{t}_j^n$ has been cancelled by the first term in the cross product.

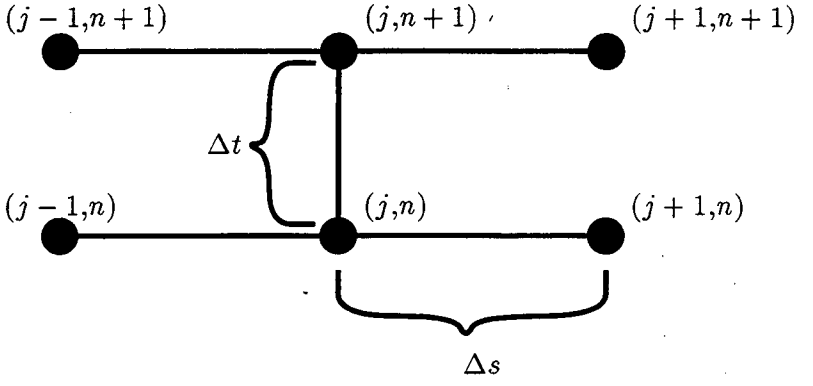

Figure 5.1: Stencil of the Buttke scheme

The finite difference scheme (5.1) is formally second-order accurate. It has three invariants:

$$| \mathbf{t}_j^{n+1} | = | \mathbf{t}_j^n |, \tag{5.2}$$

$$\sum_{j=1}^{j=N} \mathbf{t}_j^{n+1} = \sum_{j=1}^{j=N} \mathbf{t}_j^n, \tag{5.3}$$

$$\sum_{j=1}^{j=N} | \mathbf{t}_{j+1}^{n+1} - \mathbf{t}_j^{n+1} |^2 = \sum_{j=1}^{j=N} | \mathbf{t}_{j+1}^n - \mathbf{t}_j^n |^2 . \tag{5.4}$$

The first invariant (5.2) implies that there is no local stretching of the vortex. The second invariant (5.3) guarantees that a closed vortex remains closed. The third invariant (5.4) corresponds to

$$\frac{d}{dt} \int | \mathbf{t}' |^2 \, ds = 0. \tag{5.5}$$

The equation (5.1) can be solved by two iterative methods. Both methods produce a sequence of unit vectors $\mathbf{x}_j^k$ which converges to $\mathbf{t}_j^n$, provided Δt is appropriately restricted.

In the first iterative method, given unit vector $\mathbf{t}_j^n$, we define $\mathbf{y}_j^{k+1}$ by the equation

$$\mathbf{y}_j^{k+1} - \mathbf{t}_j^n = \frac{\Delta t}{4(\Delta s)^2} (\mathbf{x}_j^k + \mathbf{t}_j^n) \times (\mathbf{x}_{j+1}^k + \mathbf{x}_{j-1}^k + \mathbf{t}_{j+1}^n + \mathbf{t}_{j-1}^n) \tag{5.6}$$

and then define

$$\mathbf{x}_j^{k+1} \equiv \frac{\mathbf{y}_j^{k+1}}{|\,\mathbf{y}_j^{k+1}\,|}. \tag{5.7}$$

It can be shown that $\mathbf{x}_j^n \longrightarrow \mathbf{t}_j^{n+1}$ if $\Delta t < \frac{1}{4}(\Delta s)^2$ [16].

In the second iterative method, we define the sequence of unit vectors $\mathbf{x}_j^k$ by

$$\mathbf{x}_j^{k+1} - \mathbf{t}_j^n = \frac{\Delta t}{4(\Delta s)^2}(\mathbf{x}_j^{k+1} + \mathbf{t}_j^n) \times (\mathbf{x}_{j+1}^k + \mathbf{x}_{j-1}^k + \mathbf{t}_{j+1}^n + \mathbf{t}_{j-1}^n). \tag{5.8}$$

The sequence $\mathbf{x}_j^k$ obtained in this manner converges to $\mathbf{t}_j^{n+1}$ if $\Delta t < (\Delta s)^2$ [16].

A formally fourth-order accurate method can be obtained by the equation:

$$\mathbf{t}_j^{n+1} - \mathbf{t}_j^n = \frac{\Delta t}{4(\Delta s)^2}\mathbf{t}_j \times [\frac{4}{3}(\mathbf{t}_j + \mathbf{t}_{j+1}) - \frac{1}{12}(\mathbf{t}_{j-2} + \mathbf{t}_{j+2})] \tag{5.9}$$

where $\mathbf{t}_j \equiv (\mathbf{t}_j^n + \mathbf{t}_j^{n+1})$.

To summarize, the basic flow of the algorithm for the local induction equation is as follows:

- Represent the initial curve in terms of arc length s. Assume the initial curve can be expressed as follows in terms of σ,

$$\begin{cases} x = x(\sigma) \\ y = y(\sigma) \\ z = z(\sigma) \quad \text{with } 0 \le \sigma \le T \end{cases}$$

  where σ is a parameter. We define

$$s(\sigma) = \int_0^\sigma f(u)du \tag{5.10}$$

  where

$$f(\sigma) = \sqrt{x'(\sigma)^2 + y'(\sigma)^2 + z'(\sigma)^2}. \tag{5.11}$$

  The total arc length $s0 = s(T)$ can be calculated by numerical integration. Once $s0$ is found, solve the initial value problem

$$\begin{cases} \frac{d\sigma}{ds} &= \frac{1}{f(\sigma)} \\ \sigma(0) &= 0 \text{ with } 0 \le s \le s0 \end{cases}$$

  to find σ as a function of s. Then the initial curve in terms of s follows.

- Use iterative method to solve LIA (3.12).
- Integrate

$$\frac{d\mathbf{r}}{ds} = \mathbf{t} \tag{5.12}$$

to update the position vectors.

For the model problem, we interpret the points s_j as the midpoints of the intervals by subdividing (0,$s0$) into N equal parts:

$$s_j = (j - \frac{1}{2})ds, \ j = 1, 2, ..., N \tag{5.13}$$

where $ds = s0/N$.

The boundary conditions (i.e. between the planes) may then be enforced by reflection:

$$\mathbf{t}_0^n = (t_{1,x}^n, -t_{1,y}^n, -t_{1,z}^n), \tag{5.14}$$

$$\mathbf{t}_{N+1}^n = (t_{N,x}^n, -t_{N,y}^n, -t_{N,z}^n), \tag{5.15}$$

where $t_{1,x}^n$, $t_{1,y}^n$ and $t_{1,z}^n$ are the three components of vector $\mathbf{t}_1^n$; $t_{N,x}^n$, $t_{N,y}^n$ and $t_{N,z}^n$ are the three components of vector $\mathbf{t}_N^n$.

If the coordinates of the vortex filament are desired at any particular time $t = n \cdot dt$, they can be found by numerical integration according to the midpoint rule (for simplicity we keep the first point fixed):

$$\mathbf{r}_0^n = \mathbf{r}_0^0, \tag{5.16}$$

$$\mathbf{r}_j^n = \mathbf{r}_{j-1}^n + dt \cdot \mathbf{t}_j^n, \ j = 1, 2, ..., N. \tag{5.17}$$

5.2 Numerical Method For the Klein-Majda Equation

The purpose of this section is to simulate the vortex motion which is described by the Klein-Majda equation. In the first part of this section we present a fractional step method designed by Klein and Majda [60] to solve the Klein-Majda equation (3.25). In the second part of the section we try to recover the filament from the filament function.

5.2.1 Fractional Step Method

Fractional step method is a well-known algorithm in numerical analysis for evolution equations. The general idea of fractional step method is the following.

Suppose one is interested in an initial value problem of the form

$$y_t = Ay + By, \ y(0) \text{ known}, \tag{5.18}$$

where A, B are linear or nonlinear operators on y in some space. Its solution produces a "solution operator", say, S_{A+B} such that

$$y(t) = S_{A+B}\ y(0). \tag{5.19}$$

Assume S_A, S_B are the solution operators of the differential equations $y_t = Ay$, $y_t = By$ respectively, in other words,

$$y_t = Ay, \ y(0) \text{ known} \iff y(t) = S_A\ y(0), \tag{5.20}$$

$$y_t = By, \ y(0) \text{ known} \iff y(t) = S_B\ y(0), \tag{5.21}$$

where $\iff$ denotes an equivalence under the appropriate solvability conditions. Then, under quite general conditions, the Lie-Trotter product formula holds (See Chorin et al. [34] and references therein):

$$S_{A+B}(t) = \lim_{n\to\infty} \left(S_A(\frac{t}{n}) S_B(\frac{t}{n}) \right)^n. \tag{5.22}$$

Therefore, to solve the full problem (5.18), we may solve the "partial" equations (5.20) and (5.21) separately for short time intervals and then employ the time-step iteration procedure (5.22). The error $||S_{A+B}(t) - (S_A(\frac{t}{n})S_B(\frac{t}{n}))^n||$ for finite n is typically $O(\frac{1}{n})$. But if A and B commute or special precautions have been taken, then the error can become $O(\frac{1}{n^2})$ [34]. Here the unsubscripted norm $||\cdot||$ refers to any norm in the operator space (for example, L^2 norm or L^1 norm).

Now we introduce a fractional step method for solving the Klein-Majda equation [60]. The method is developed for general periodic initial data. It consists of two steps. In one fractional step, solve the linear problem

$$\frac{1}{i}\frac{\partial \phi}{\partial \tau} = \frac{\partial^2 \phi}{\partial \tilde{\sigma}^2} - \varepsilon^2 I[\phi] \tag{5.23}$$

exactly. Through discrete fast Fourier transform (DFFT) of the data for ϕ on an equi-distance grid, one obtains the Fourier modes $\hat{\phi}_l$, $l = -N/2,...,N/2-1$. Then applying the exact solution formula

$$\hat{\phi}_l(\tau+\triangle\tau) = \hat{\phi}_l(\tau)\exp(-i[l^2+\varepsilon^2\hat{I}(l)]\triangle\tau) \tag{5.24}$$

and using the inverse Fourier transform (IFFT) gives the solution of (5.23).

In the second fractional step, solve the nonlinear ODE

$$\frac{1}{i}\frac{\partial\phi}{\partial\tau} = \varepsilon^2\frac{1}{2}\phi \mid \phi \mid^2 \tag{5.25}$$

exactly at each discrete spatial location by

$$\phi_l(\tau+\triangle\tau) = \phi_l(\tau)\exp(i\varepsilon^2\frac{1}{2} \mid \phi_j(\tau) \mid^2 \triangle\tau). \tag{5.26}$$

The two steps are alternated in time through Strang-type splitting. The method is second order accurate and unconditionally stable. An adaptive time step $\triangle\tau$ is chosen by

$$\triangle\tau = s\frac{2\pi}{w^*}\frac{1}{N}, \tag{5.27}$$

where s is a safety factor (say s = 0.5), N is the number of grid points and w^* is the weighted average frequency

$$w^* = \max(-\int \hat{w}(\xi) \mid \hat{\phi} \mid^2 (\xi)d\xi/\|\phi\|^2_{L^2}, \int w(\mid \phi \mid) \mid \hat{\phi} \mid^2 d\sigma/\|\phi\|^2_{L^2}) \tag{5.28}$$

and $\hat{w}$, w are the frequencies in the fractional step solution formulas in (5.24) and (5.26).

5.2.2 Relationship Between the Filament and the Filament Function

If a filament function $\phi(s,t) = \kappa \exp(i\int_0^s \tau ds)$ is known, one can determine the filament by the following procedure.

As usual, let **t**, **n**, **b** denote the tangent, normal and binormal vectors of the filament **r**. We introduce a new quantity **N**:

$$\mathbf{N} = (\mathbf{n}+i\mathbf{b})\exp(i\int_0^s \tau(\xi,t)d\xi). \tag{5.29}$$

Differentiating **N** with respect to s and using the Serret-Frenet equations (3.4) and (3.5), we find that

$$\frac{\partial\mathbf{N}}{\partial s} = -\phi\mathbf{t}. \tag{5.30}$$

We also see that

$$\frac{\partial \mathbf{t}}{\partial s} = \frac{1}{2}(\phi^* \mathbf{N} + \phi \mathbf{N}^*), \tag{5.31}$$

where ϕ^* and $\mathbf{N}^*$ denote the complex conjugate of ϕ and $\mathbf{N}$, respectively. From (5.30) and (5.31) we have

$$\frac{d}{ds}\begin{pmatrix} \mathbf{r} \\ \mathbf{t} \\ \mathbf{N} \\ \mathbf{N}^* \end{pmatrix} = \begin{bmatrix} 0 & 1 & 0 & 0 \\ 0 & 0 & \frac{\psi^*}{2} & \frac{\psi}{2} \\ 0 & -\psi & 0 & 0 \\ 0 & -\psi^* & 0 & 0 \end{bmatrix} \begin{pmatrix} \mathbf{r} \\ \mathbf{t} \\ \mathbf{N} \\ \mathbf{N}^* \end{pmatrix}. \tag{5.32}$$

Given $\mathbf{r}(0,t)$,$\mathbf{t}(0,t)$ and $\mathbf{N}(0,t)$, one can integrate (5.32) to find $\mathbf{t}(s,t)$ and then integrate $\mathbf{t}(s,t)$ to obtain $\mathbf{r}(s,t)$.

The procedure, which determines the time evolution of $\mathbf{r}$, $\mathbf{t}$, and $\mathbf{N}$ at the point $s = 0$, is nontrivial. We can avoid this difficulty by fixing $\mathbf{r}(0,t)$, $\mathbf{t}(0,t)$ and $\mathbf{N}(0,t)$ in our numerical simulations.

In summary, in order to solve the Klein-Majda equation for the vortex motion, we must do the following. First we solve the Klein-Majda equation (3.25) by a fractional step method in order to determine $\phi(s,t)$. Once $\phi(s,t)$ is found, we solve (5.32) to find $\mathbf{r}(s,t)$ by fixing $\mathbf{r}(0,t)$, $\mathbf{t}(0,t)$ and $\mathbf{N}(0,t)$.

5.3 Numerical Scheme For the Klein-Knio Equation

In this section we describe our numerical scheme for solving the Klein-Knio equation (3.48).

Klein and Knio [58] proposed a spectral variant of the thin-tube model. This variant takes advantage of the periodic nature of the targeted perturbations by using the initial parametrization variable s as Lagrangian variable. This allows a "spectral" interpolation of the filament geometry, which is incorporated in the present variant of the thin-tube model by processing the Lagrangian nodal locations with a discrete fast Fourier transform routine. The resulting Fourier coefficients are then used to estimate the first and second spectral derivatives of the Lagrangian nodel coordinates with respect to s. Once the first and second derivatives are computed, the tangent, normal, binormal, and curvature of the filament can be evaluated directly. One has to be very careful when performing the spectral processing.

Once the velocity is computed, they use a variable-step second-order predictor-corrector scheme to advance the vortex filament.

We use a different method here which is simple and straightforward to program. We will describe our method in details in this section.

Before introducing our method for solving the Klein-Knio equation with periodic boundary conditions, we give a treatment of the periodic boundary conditions [58].

5.3.1 Periodic Boundary Conditions

In principal, the Biot-Savart evaluation of the velocity requires integration over the entire vorticity field, i.e. over infinitely many periodic images of the control volume as well. While this can be done analytically in two dimensions for point vortices [65], such an analytic expression for the infinite summation procedure in three dimensions has not yet been found. Consequently, a common approach is to truncate the interaction to a finite number of images, which causes a slight inaccuracy. On the other hand, one can employ Poisson's summation formula for infinite series in order to convert the slowly converging sum over the periods to a more rapidly converging Fourier series. This technique has been used by Strain [103] when he developed fast algorithms for classical potential theory.

We give an alternative approach here. The main idea is to precalculate the summations over the periodic images for discrete values using a much larger cutoff. Subsequently, the specific evaluations of the summations during the simulation are obtained by interpolation. For simplicity, assume the periodicity direction coincides with the x-direction of a right-handed coordinate system (x,y,z) with basis vectors $(\mathbf{e}_1, \mathbf{e}_2, \mathbf{e}_3)$. We can write the velocity $\mathbf{u}^{\text{ttm}}$ as

$$\mathbf{u}^{\text{ttm}}(\mathbf{x}) = \sum_{i=1}^{N} (\mathbf{u}_1(\mathbf{x}) + \mathbf{u}_2(\mathbf{x})), \tag{5.33}$$

where $\mathbf{u}_1(\mathbf{x})$ and $\mathbf{u}_2(\mathbf{x})$ are respectively the contributions of the i-th element of length $\delta\chi = (\Delta x, \Delta y, \Delta z)$ centered at $\chi^c = (x_o, y_o, z_o)$ and its image system.

Since we assume $L >> \delta$, the effect of the core smoothing function can be neglected from the contribution of the image system. Hence we can take $f_\delta \equiv 1$ for the image system. After straightforward manipulations, we obtain

$$\mathbf{u}_1(\mathbf{x}) = \frac{\Gamma}{4\pi} \frac{(\chi^c - \mathbf{x}) \times \delta\chi}{|\chi^c - \mathbf{x}|} f_\delta(\chi^c - \mathbf{x}), \tag{5.34}$$

$$\mathbf{u}_2(\mathbf{x}) = \frac{\Gamma}{4\pi}\Big(\sum_{k\neq 0}\frac{(\chi^c-\mathbf{x})\times\delta\chi}{[(x_o+kL-x)^2+(y_o-y)^2+(z_o-z)^2]^{3/2}} + \sum_{k\neq 0}\frac{kL(\Delta y\ \mathbf{e}_3-\Delta z\ \mathbf{e}_2)}{[(x_o+kL-x)^2+(y_o-y)^2+(z_o-z)^2]^{3/2}}\Big), \tag{5.35}$$

where L is the period and the contribution of the image system of the vortex filament is handled exactly. Define

$$F(x,y,z) = \sum_{k\neq 0}\frac{1}{[(x+kL)^2+y^2+z^2]^{3/2}}, \tag{5.36}$$

$$G(x,y,z) = \sum_{k\neq 0}\frac{kL}{[(x+kL)^2+y^2+z^2]^{3/2}}. \tag{5.37}$$

In a preprocessing step, the functions F and G are evaluated numerically by truncating the summation at a large index. The computed values are stored which are interpolated during the computations. The storage can be optimized by tabulating half the needed values because

$$F(-x,-y,-z) = F(x,y,z), \tag{5.38}$$

$$G(-x,-y,-z) = \mathrm{sign}(x)G(x,y,z). \tag{5.39}$$

Once the velocity induced by the entire image system of a single element is estimated, summation over the image systems of all the elements must be performed to obtain the total velocity. In doing so, the vortex interaction algorithm ensures that the assumption that the core smoothing function acts on the nearest vortex element is satisfied by the following technique. In order to estimate the velocity field at a point inside the computational domain, the algorithm first performs a translation of the entire domain along the periodicity direction, $x \rightarrow x' = x + d$, so that the point under consideration coincides with the center of the original domain (Figure 5.2). This coordinate translation is also applied to the Lagrangian locations of the vortex elements. Based on the translated locations, the algorithm identifies exactly the members of all image systems which lie within the original computational domain. The locations of these elements are then used in the summation described above. This procedure enables us to enforce periodicity boundary conditions exactly and interpolated on fine grids.

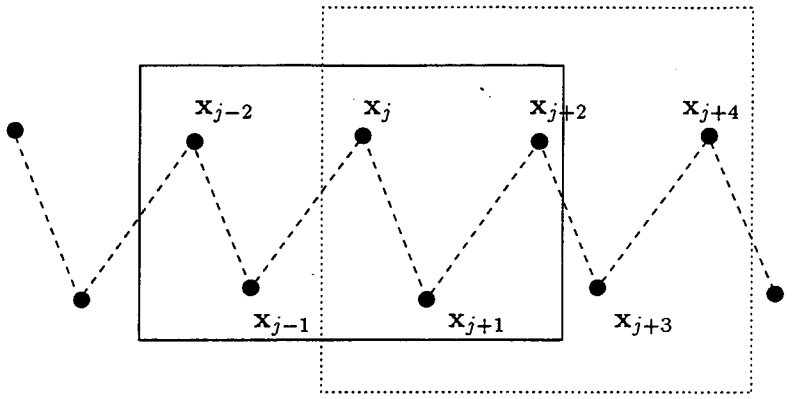

Figure 5.2: In three-dimensional simulations of spatially periodic flows, the core smoothing function acts on the nearest vortex element hence the computational domain has to be changed when different points are under consideration. For example, the computational domain for $\mathbf{x}_j$ includes $\mathbf{x}_{j-2}$, $\mathbf{x}_{j-1}$, $\mathbf{x}_{j+1}$, and $\mathbf{x}_{j+2}$, whereas the computational domain for $\mathbf{x}_{j+2}$ is based on $\mathbf{x}_j$, $\mathbf{x}_{j+1}$, $\mathbf{x}_{j+3}$, and $\mathbf{x}_{j+4}$.

5.3.2 Numerical Recipe For the Klein-Knio Equation

To solve the Klein-Knio equation (3.48), the procedure consists of the following steps:

1. To start the integration of the Klein-Knio equation, the physical core structure coefficient C and its analog C^{ttm} based on numerical vorticity distribution are required. One can calculate the physical core structure coefficient C by

$$C = \lim_{r\to\infty}\left(\frac{4\pi^2}{\Gamma^2}\int_0^r r'\nu^{(0)^2}dr' - \ln r\right) - \frac{1}{2} \tag{5.40}$$

and the circumferential velocity is related to the leading order axial vorticity via $\bar{r}\zeta^{(0)} = (\bar{r}\nu^{(0)})_{\bar{r}}$. For Gaussian axial vorticity distribution and zero axial flow, $C = -0.558$.

To obtain C^{ttm}, one can pick a numerical vortex core smoothing function f and calculate C^{ttm} by

$$\zeta^{(0),\mathrm{ttm}}(\bar{r}) = \Gamma\int_{-\infty}^{\infty} f(\sqrt{\bar{r}^2+z^2})dz, \tag{5.41}$$

$$\zeta_{11}^{(1),\mathrm{ttm}} = \frac{\Gamma\kappa}{2}\int_{-\infty}^{\infty}\frac{\bar{r}z^2}{\sqrt{\bar{r}^2+z^2}}f'(\sqrt{\bar{r}^2+z^2})dz, \tag{5.42}$$

$$C^{\mathrm{ttm}} = -\left(\frac{1}{2}+\frac{2\pi}{\Gamma}\int_0^{\infty}\left[\frac{1}{\kappa}\zeta_{11}^{(1),\mathrm{ttm}} + \bar{r}\ln\bar{r}\zeta^{(0),\mathrm{ttm}}\right]d\bar{r}\right). \tag{5.43}$$

If we choose $f(r) = \frac{3}{4\pi}\ e^{-r^3}$, $C^{\rm ttm} = 0.49925804107389$. The derivation is as follows. The substitution of $f(r) = \frac{3}{4\pi}\ e^{-r^3}$ into (5.43) gives

$$\begin{aligned} C^{\rm ttm} &= -\frac{1}{2} + \frac{9}{4}\int_0^\infty \int_{-\infty}^\infty \frac{\bar{r}z^2}{\sqrt{\bar{r}^2+z^2}}(\bar{r}^2+z^2)e^{-(\bar{r}^2+z^2)\sqrt{\bar{r}^2+z^2}}\ dzd\bar{r} \\ &\quad -\frac{3}{2}\int_0^\infty \int_{-\infty}^\infty \bar{r}\ln\bar{r}\ e^{-(\bar{r}^2+z^2)\sqrt{\bar{r}^2+z^2}}\ dzd\bar{r} \\ &= -\frac{1}{2} + \frac{9}{8}\int_{-\infty}^\infty \int_{-\infty}^\infty \frac{|\bar{r}|z^2}{\sqrt{\bar{r}^2+z^2}}(\bar{r}^2+z^2)e^{-(\bar{r}^2+z^2)\sqrt{\bar{r}^2+z^2}}\ dzd\bar{r} \\ &\quad -\frac{3}{4}\int_{-\infty}^\infty \int_{-\infty}^\infty |\bar{r}|\ln|\bar{r}|\ e^{-(\bar{r}^2+z^2)\sqrt{\bar{r}^2+z^2}}\ dzd\bar{r} \\ &\equiv -\frac{1}{2} + \frac{9}{8}t_1 - \frac{3}{4}t_2. \end{aligned} \tag{5.44}$$

To evaluate t_1 and t_2, we make a change of variables: $\bar{r} = r\cos\theta, z = r\sin\theta$. Then

$$\begin{aligned} t_1 &= \int_0^\infty r^5 e^{-r^3}\ dr \int_0^{2\pi} |\cos\theta|\sin^2\theta\ d\theta = \frac{4}{3}\int_0^\infty r^5 e^{-r^3}\ dr \\ &= \frac{4}{3}\cdot\frac{1}{3} = \frac{4}{9}, \end{aligned} \tag{5.45}$$

and

$$\begin{aligned} t_2 &= \int_0^\infty r^2\ln r\ \ e^{-r^3}\ dr \int_0^{2\pi} |\cos\theta| d\theta + \int_0^\infty r^2 e^{-r^3}\ dr \int_0^{2\pi} |\cos\theta|\ln|\cos\theta| d\theta \\ &= \int_0^\infty r^2\ln r\ \ e^{-r^3}\ dr + \frac{1}{3}(-4+4\ln 2). \end{aligned} \tag{5.46}$$

Let $t = r^3$, we have

$$\begin{aligned} \int_0^\infty r^2\ln r e^{-r^3}\ dr &= \frac{1}{9}(\int_0^1 + \int_1^\infty)e^{-t}\ln t\ dt \\ &= \frac{1}{9}(\int_0^1 \ln t\ d(-e^{-t}+1) + \int_1^\infty \ln t\ d(-e^{-t})) \\ &= \frac{1}{9}(\int_0^1 \frac{e^{-t}-1}{t}\ dt + \int_1^\infty \frac{e^{-t}}{t}\ dt) \\ &= \frac{1}{9}\int_0^1 \frac{1}{t}(e^{-\frac{1}{t}} + e^{-t} - 1)\ dt \end{aligned} \tag{5.47}$$

which can be calculated by quadrature algorithm. We use the Composite Simpson's rule to obtain the value listed above.

2. Evaluate the induced velocity $\mathbf{u}(\mathbf{x})$:

$$\mathbf{u}(\mathbf{x}) = \mathbf{u}^{\rm ttm} + \frac{\Gamma}{4\pi}(\kappa\mathbf{b})[C - C^{\rm ttm} + \ln\frac{\delta^{\rm ttm}}{\delta}], \tag{5.48}$$

where the evaluation of $\mathbf{u}^{\mathrm{ttm}}$ is described in the previous section. To obtain the product of the curvature κ and the binormal vector $\mathbf{b}$, we use a periodic cubic spline to interpolate the discrete numerical nodes. Specifically, for each component (x, y or z), we find a piece-wise cubic polynomial of a parameter η to fit the numerical data. For example, for x component, given the values x_0, x_1,...,x_N on the nodes η_0,η_1,...,η_N, our periodic cubic spline algorithm seeks a function $S(\eta)$ such that

a. $S(\eta)$ is a cubic polynomial, denoted S_i, on the interval $[\eta_i, \eta_{i+1}]$ for each $i = 0, 1, ..., N-1$;

b. $S(\eta_i) = x(\eta_i)$ for each $i = 0, 1, ..., N-1$;

c. $S_{i+1}(\eta_{i+1}) = S_i(\eta_{i+1})$ for each $i = 0, 1, ..., N-2$;

d. $S'_{i+1}(\eta_{i+1}) = S'_i(\eta_{i+1})$ for each $i = 0, 1, ..., N-2$;

e. $S''_{i+1}(\eta_{i+1}) = S''_i(\eta_{i+1})$ for each $i = 0, 1, ..., N-2$;

f. the periodic boundary conditions are satisfied:

$$\begin{aligned} S_0(\eta_0) &= S_{N-1}(\eta_N), \\ S'_0(\eta_0) &= S'_{N-1}(\eta_N), \\ S''_0(\eta_0) &= S''_{N-1}(\eta_N). \end{aligned}$$

The parameter η for the spline can be chosen arbitrarily. Here it is taken as the length of the piece-wise straight line going through the numerical nodes. We pick this parameter because it is easy to calculate and it is a very good approximation (second order accurate) to the current arc length s. Once we have the cubic spline representations for x, y and z, the binormal vector times the curvature $\kappa\mathbf{b}$ can be calculated directly

$$\begin{aligned} \kappa\mathbf{b} &= \frac{d\mathbf{r}}{ds} \times \frac{d^2\mathbf{r}}{ds^2} \\ &= \left(\frac{d\mathbf{r}}{d\eta}\frac{d\eta}{ds}\right) \times \left(\frac{d^2\mathbf{r}}{d\eta^2}\left(\frac{d\eta}{ds}\right)^2 + \frac{d\mathbf{r}}{d\eta}\frac{d^2\eta}{ds^2}\right) \\ &= \left(\frac{d\mathbf{r}}{d\eta} \times \frac{d^2\mathbf{r}}{d\eta^2}\right)\left(\frac{d\eta}{ds}\right)^3, \end{aligned} \tag{5.49}$$

where

$$\frac{d\mathbf{r}}{d\eta} = (\frac{dx}{d\eta}, \frac{dy}{d\eta}, \frac{dz}{d\eta}), \tag{5.50}$$

$$\frac{d^2\mathbf{r}}{d\eta^2} = (\frac{d^2x}{d\eta^2}, \frac{d^2y}{d\eta^2}, \frac{d^2z}{d\eta^2}), \tag{5.51}$$

$$\frac{d\eta}{ds} = 1/|\frac{d\mathbf{r}}{d\eta}|. \tag{5.52}$$

3. Integrate

$$\frac{d\mathbf{x}}{dt} = \mathbf{u} \tag{5.53}$$

to advance the vortex filament.

For the model problem, numerical experiments show that it is very inefficient if we try to use (5.48) directly because the time step is very small. To be more efficient, we use a fractional step algorithm in conjunction with a high order embedded Runge-Kutta method. Before presenting our method, we need to review the Runge-Kutta method.

Runge-Kutta method is an efficient technique for the solution of the non-stiff initial value problem

$$y'(x) = f(x, y(x)),\ y(x_0) = y_0. \tag{5.54}$$

A general s-stage explicit Runge-Kutta method is [47]

$$\begin{aligned} k_1 &= f(x_n, y_n) \\ k_2 &= f(x_n + c_2 h, y_n + h a_{21} k_1) \\ k_3 &= f(x_n + c_3 h, y_n + h(a_{31} k_1 + a_{32} k_2)) \\ &\cdots \\ k_s &= f(x_n + c_s h, y_n + h(a_{s1} k_1 + \ldots + a_{s,s-1} k_{s-1})) \\ y_{n+1} &= y_n + h(b_1 k_1 + \ldots + b_s k_s) \end{aligned} \tag{5.55}$$

where the parameters a_{ij}, b_i, $c_i = \sum_{j=1}^{i-1} a_{ij}$ must be chosen to satisfy the equations of order condition.

Briefly, (5.55) can be symbolized by Butcher's array

0					
c_2	a_{21}				
c_3	a_{31}	a_{32}			
.	.	.	.		
.	.	.	.		
c_s	a_{s1}	a_{s2}	...	$a_{s,s-1}$	
	b_1	b_2	...	b_{s-1}	b_s

For example, the Runge-Kutta method of order four has the Butcher's array

0				
1/2	1/2			
1/2	0	1/2		
1	0	0	1	
	1/6	2/6	2/6	1/6

An embedded Runge-Kutta method comprises two Runge-Kutta formulas of orders p and q ($q > p$ and usually $q = p + 1$) which share the same function evaluations. By using methods of differing order one can predict the local truncation error and, using this prediction, choose a step size that will keep the global error in check. There are many embedded Runge-Kutta methods. One popular technique is the Runge-Kutta-Fehlberg method which consists of using a Runge-Kutta method of order five to estimate the local error in a Runge-Kutta method of order four. In our simulation we use an embedded Runge-Kutta method of order (7)8 due to Prince and Dormand [82].

To approximate (5.48) and (5.53), one can do the following. In one fractional step, solve

$$\frac{d\mathbf{x}}{dt} = \mathbf{u}^{\text{ttm}} \tag{5.56}$$

by an embedded Runge-Kutta method for one step with controlled step size dt1. In the second fractional step, solve

$$\frac{d\mathbf{x}}{dt} = \frac{\Gamma}{4\pi}(\kappa\mathbf{b})[C - C^{\text{ttm}} + \ln\frac{\delta^{\text{ttm}}}{\delta}] \tag{5.57}$$

by the embedded Runge-Kutta method for several steps so that the total advanced time is equal to dt1. The two steps are alternated in time through Strang-type splitting.

5.4 Numerical Calculation of Energy

As stated before, total vorticity, helicity and energy described by (3.98) are conserved quantities for flows which are periodic in the x-direction. For an isolated slender

vortex, the helicity, which measures the winding numbers, is always a constant. The total vorticity is also conserved as long as the filament is connected. Hence the energy (3.98) is the one of great interest.

When dealing with a single slender vortex filament, we can simplify the estimate of energy (3.98) by the following technique. Let $\mathbf{x}(s)$ be the centerline of the vortex filament. Assume

$$\text{supp } \omega(\mathbf{x}) \subset \Omega = \{\mathbf{x}' \mid |\mathbf{x}' - \mathbf{x}(s)| < \delta_c \text{ for some s}\} \tag{5.58}$$

and δ_c satisfies $\delta < \delta_c << R$ where δ is the core size and R is the radius of curvature.

Let $p =$ arc length of the centerline in a period of x-direction. One can show that in curvilinear coordinate system:

$$E = \frac{1}{8\pi}\int_0^p ds \int_{s-\frac{p}{2}}^{s+\frac{p}{2}} ds' \int_0^{\delta_c} r dr \int_0^{2\pi} d\theta \int_0^{\delta_c} r' dr' \int_0^{2\pi} d\theta'$$
$$\sum_{j=-\infty}^{+\infty} \left(\frac{1}{|\mathbf{x}-\mathbf{x}'-j(L,0,0)|} - \frac{1}{(|j|+1)L}\right) \omega(\mathbf{x}')\cdot\omega(\mathbf{x}). \tag{5.59}$$

We can split E into two terms:

$$E = \frac{1}{8\pi}\int_0^p [b_1(s) + b_2(s)]ds, \tag{5.60}$$

where

$$b_1(s) = \int_{s-\frac{p}{2}}^{s+\frac{p}{2}} ds' \int_0^{\delta_c} r dr \int_0^{2\pi} d\theta \int_0^{\delta_c} r' dr' \int_0^{2\pi} d\theta'$$
$$\sum_{j\neq 0} \left(\frac{1}{|\mathbf{x}-\mathbf{x}'-j(L,0,0)|} - \frac{1}{(|j|+1)L}\right) \omega(\mathbf{x}')\cdot\omega(\mathbf{x}), \tag{5.61}$$

and

$$b_2(s) = \int_{s-\frac{p}{2}}^{s+\frac{p}{2}} ds' \int_0^{\delta_c} r dr \int_0^{2\pi} d\theta \int_0^{\delta_c} r' dr' \int_0^{2\pi} d\theta' \left(\frac{1}{|\mathbf{x}-\mathbf{x}'|} - \frac{1}{L}\right) \omega(\mathbf{x}')\cdot\omega(\mathbf{x}). \tag{5.62}$$

The evaluation of $b_1(s)$ can be done as follows.

$$b_1(s) \approx \int_{s-\frac{p}{2}}^{s+\frac{p}{2}} ds' \ \Gamma^2 \frac{\partial}{\partial s}\mathbf{x}(s)\cdot\frac{\partial}{\partial s'}\mathbf{x}(s')$$
$$\sum_{j\neq 0} \left(\frac{1}{|\mathbf{x}(s)-\mathbf{x}(s')-j(L,0,0)|} - \frac{1}{(|j|+1)L}\right) \tag{5.63}$$

Write $\mathbf{x}(s) = (x(s), y(s), z(s))$, then

$$\sum_{j\neq 0}\left(\frac{1}{|\,\mathbf{x}(s)-\mathbf{x}(s')-j(L,0,0)\,|}-\frac{1}{(|\,j\,|+1)L}\right)$$
$$=\frac{1}{L}H\left(\frac{x(s)-x(s')}{L},\sqrt{\left(\frac{y(s)-y(s')}{L}\right)^2+\left(\frac{z(s)-z(s')}{L}\right)^2}\right) \tag{5.64}$$

and the function H of two variables is defined as

$$H(d_1,d_2)=\sum_{j\neq 0}\left\{\frac{1}{[(d_1-j)^2+d_2^2]^{\frac{1}{2}}}-\frac{1}{|\,j\,|+1}\right\}. \tag{5.65}$$

H has no singularity and can be tabulated by exploiting the following relationships:

$$H(-d_1,d_2)=H(d_1,d_2), \tag{5.66}$$
$$H(d_1,-d_2)=H(d_1,d_2). \tag{5.67}$$

Therefore

$$b_1(s)=\int_{s-\frac{p}{2}}^{s+\frac{p}{2}} ds'\Gamma^2\frac{\partial}{\partial s}\mathbf{x}(s)\cdot\frac{\partial}{\partial s'}\mathbf{x}(s')$$
$$\frac{1}{L}H\left(\frac{x(s)-x(s')}{L},\sqrt{\left(\frac{y(s)-y(s')}{L}\right)^2+\left(\frac{z(s)-z(s')}{L}\right)^2}\right) \tag{5.68}$$

can be computed accurately with numerical integration.

To compute $b_2(s)$, pick a parameter δ_B satisfying $\delta << \delta_B << R$. Then

$$b_2(s)=\int_{\delta_B<|s'-s|<\frac{p}{2}} ds'\int_0^{\delta_c} rdr\int_0^{2\pi} d\theta\int_0^{\delta_c} r'dr'\int_0^{2\pi} d\theta'\left(\frac{1}{|\,\mathbf{x}-\mathbf{x}'\,|}-\frac{1}{L}\right)\boldsymbol{\omega}(\mathbf{x})\cdot\boldsymbol{\omega}(\mathbf{x}')$$
$$+\int_{s-\delta_B}^{s+\delta_B} ds'\int_0^{\delta_c} rdr\int_0^{2\pi} d\theta\int_0^{\delta_c} r'dr'\int_0^{2\pi} d\theta'\left(\frac{1}{|\,\mathbf{x}-\mathbf{x}'\,|}-\frac{1}{L}\right)\boldsymbol{\omega}(\mathbf{x})\cdot\boldsymbol{\omega}(\mathbf{x}')$$
$$\equiv b_3(s)+b_4(s). \tag{5.69}$$

We can approximate $b_3(s)$ by

$$b_3(s)\approx\int_{\delta_B<|s'-s|<\frac{p}{2}} ds'\Gamma^2\frac{\partial}{\partial s}\mathbf{x}(s)\cdot\frac{\partial}{\partial s'}\mathbf{x}(s')\left(\frac{1}{|\,\mathbf{x}(s)-\mathbf{x}(s')\,|}-\frac{1}{L}\right). \tag{5.70}$$

As in Klein-Knio's asymptotic approach, we assume that the leading term vorticity is independent of arc length coordinate. Thus $b_4(s)$ can be computed by

$$b_4(s)\approx\int_{-\delta_B}^{\delta_B} dz\int_0^{\delta_c} rdr\int_0^{2\pi} d\theta\int_0^{\delta_c} r'dr'\int_0^{2\pi} d\theta'$$
$$\left(\frac{1}{[(rcos\theta-r'cos\theta')^2+(rsin\theta-r'sin\theta')^2+z^2]^{\frac{1}{2}}}-\frac{1}{L}\right)\boldsymbol{\omega}(r)\cdot\boldsymbol{\omega}(r'). \tag{5.71}$$

where $\omega(r)$ is the leading term of vorticity distribution .

For a given vorticity distribution $\omega(r)$ and a fixed δ_B, $b_4(s)$ is a constant which can be calculated once and for all.

5.5 Numerical Experiments with The Local Induction Equation

In Figure 5.3 we present the general configuration of the vortex filament at time $t = 0.0, 0.5, 1.0$ and 1.5. The initial filament is represented by 257 points. We observe that the filament evolves smoothly. In our numerical simulation using the local induction method, we can monitor conservation of the arc length as an accuracy check. In Figure 5.4, we plot the time-dependent evolution of the total arc length as well as energy.

In a subsequent simulation, we simulate the sideband instability and dynamic behaviors of Kelvin waves using the same numerical algorithm but the results are analyzed into Fourier components and plotted as a function of time.

When the ratio of the amplitude of the main harmonic a_0 and its wavelength λ is 0.02 initially, the amplitudes of the sideband waves don't grow (Figure 5.5 top). We obtain *stable* phenomena. If the initial a_0/λ is increased, the amplitudes of the sidebands start to grow due to Benjamin-Feir instabilities. However, after some time the amplitude of the main harmonic begins to grow and the amplitudes of the sidebands declines. The main harmonic and the sidebands grow or decay alternatively and the process repeats itself although not with perfect periodicity (Figure 5.5 bottom). This kind of phenomenon is normally referred to as the *Fermi-Pasta-Ulam recurrence* [41], as opposed to Poincaré recurrence, which requires the return of both amplitude and phase to their initial states. We observe that a further increase in a_0/λ leads to a behavior which is neither stable nor recurrent (Figure 5.6). Such a phenomenon is *chaotic*.

The numerical results presented here are in good agreement with the linear stability analysis and illustrate stable, recurrent and chaotic phenomena.

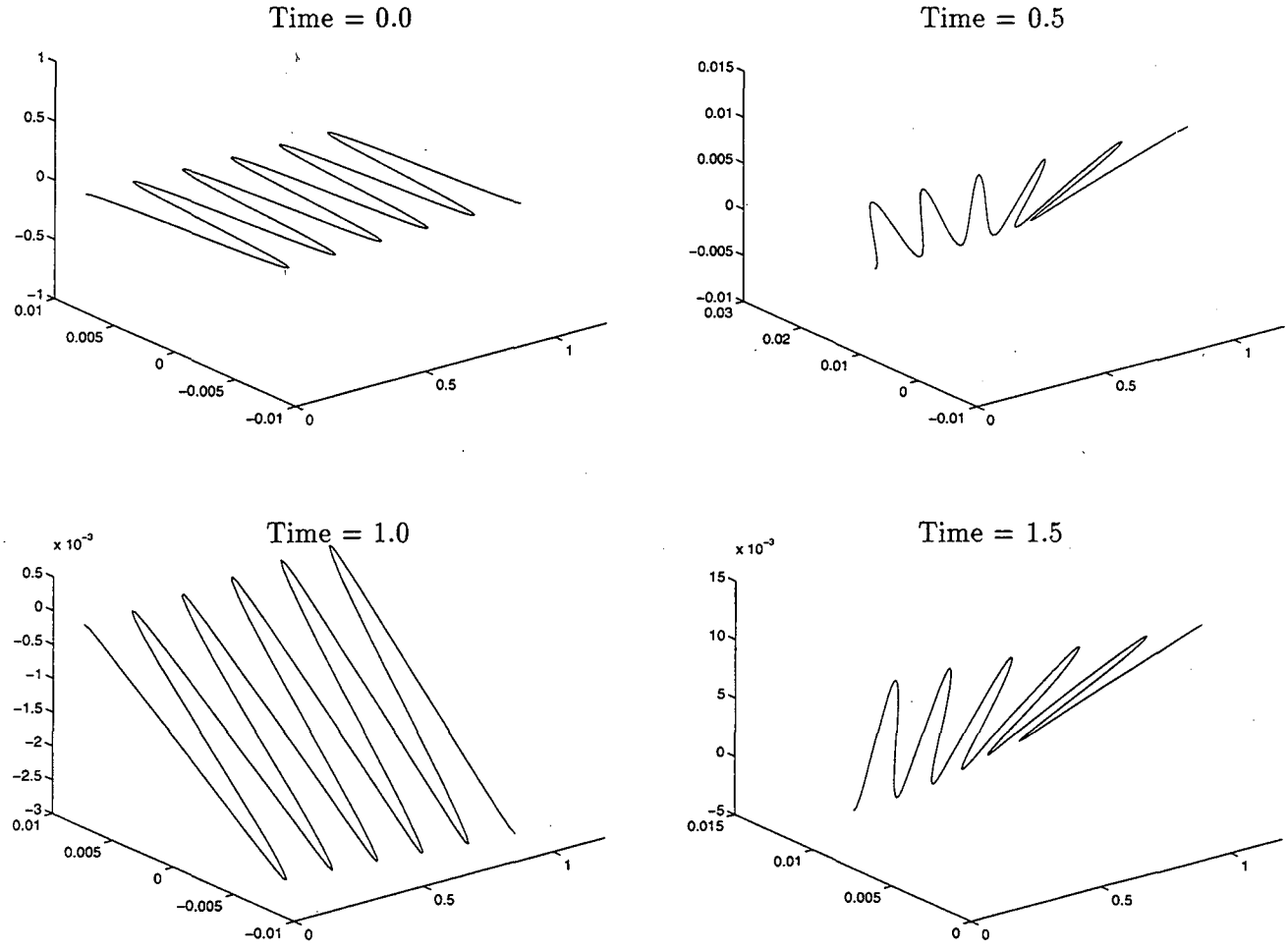

Figure 5.3: Evolution of the Kelvin waves whose motion is described by the local induction equation: $\frac{a_0}{\lambda} = 0.04$.

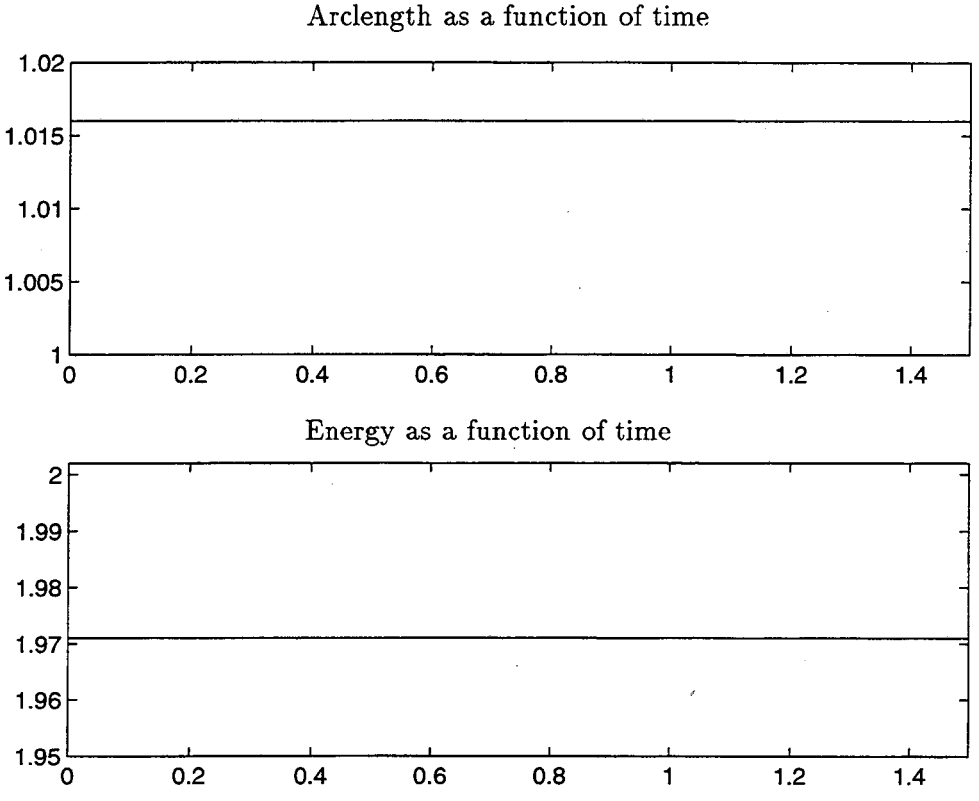

Figure 5.4: Approximate conservation of invariants for the local induction equation with $a_0/\lambda = 0.04$.

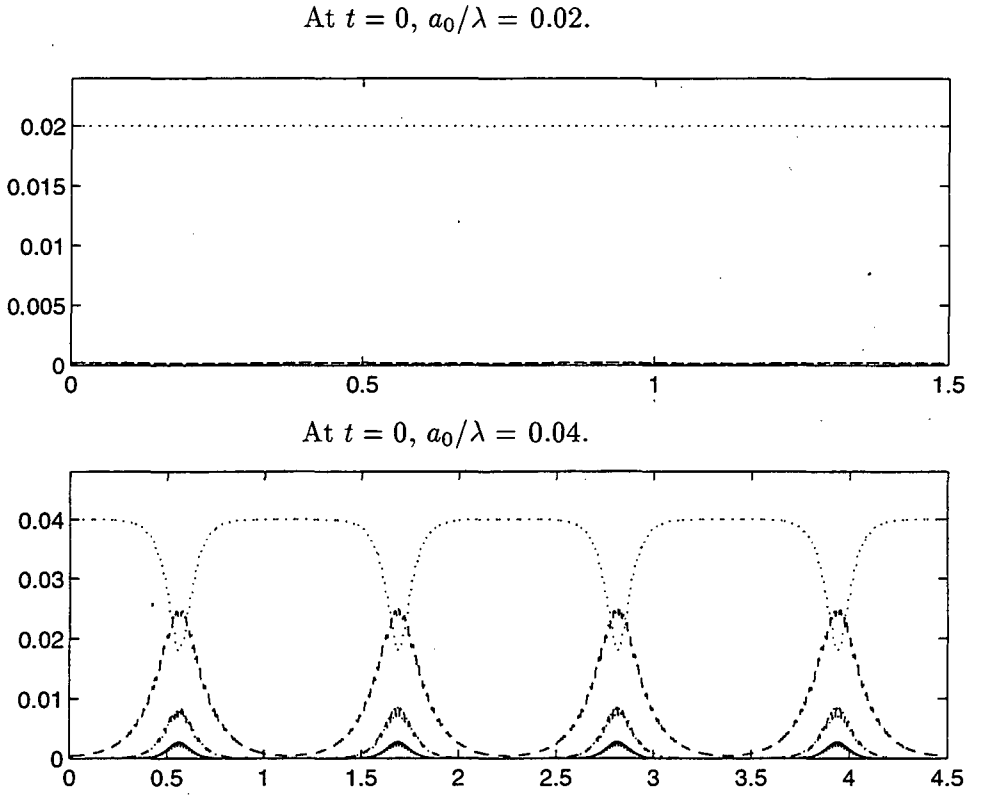

Figure 5.5: Sideband instability and stable, recurrent phenomenon for Kelvin waves which evolve according to the local induction equation. The x-axis is the time, whereas the y-axis is the ratio of the amplitude and wavelength λ. The initial conditions are a superposition of a planar wave (number of half waves $n = 11$, amplitude a_0 and wavelength λ) and two neighboring sidebands of small amplitude as a perturbation. Plotted are the amplitude of the main harmonic ($n = 11$) and the lower harmonics ($n = 10, 9, 8$ in order of decreasing amplitude) as a function of time. A plot of the upper harmonics ($n = 12, 13, 14$) looks very similar.

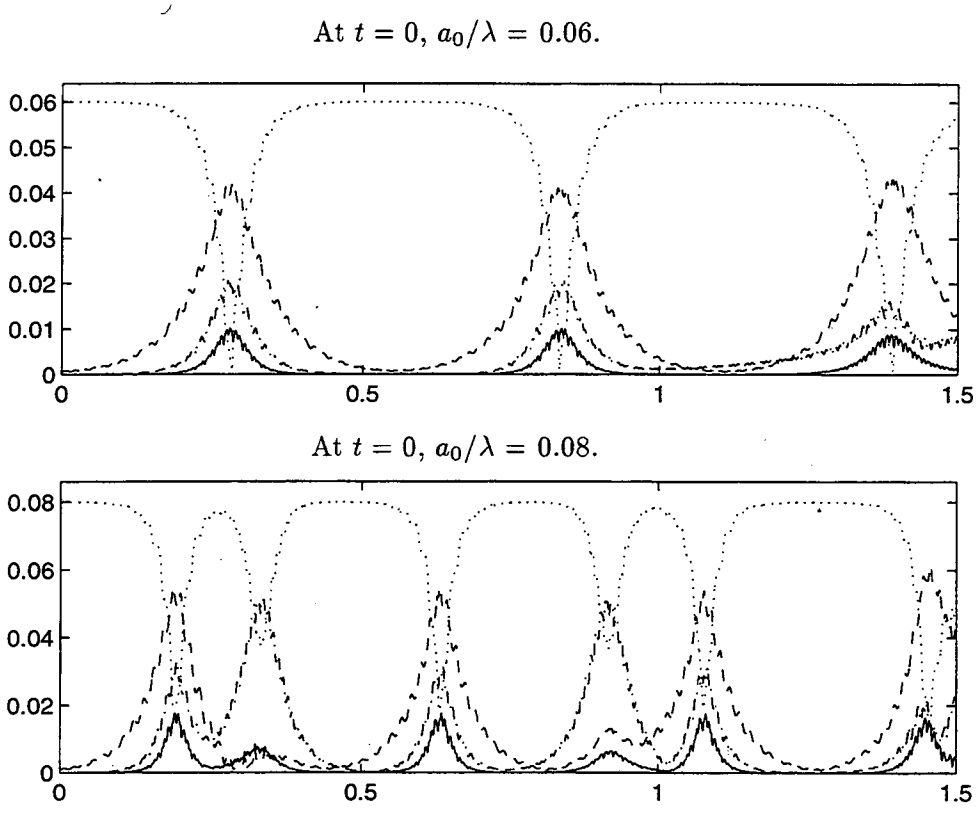

Figure 5.6: Sideband instability and chaotic phenomenon for Kelvin waves which evolve according to the local induction equation.

5.6 Numerical Results with The Klein-Majda Equation

In this section we present the numerical results for both the filament function and the filament curve according to the Klein-Majda equation.

5.6.1 Numerical Experiments for the Filament Function

In Figure 4.2 we have shown the stability diagram for sideband perturbations for the filament function of the helical waves. To see it more clearly, we enlarge some part of the diagram for $\varepsilon = 0.309$ in Figure 5.7.

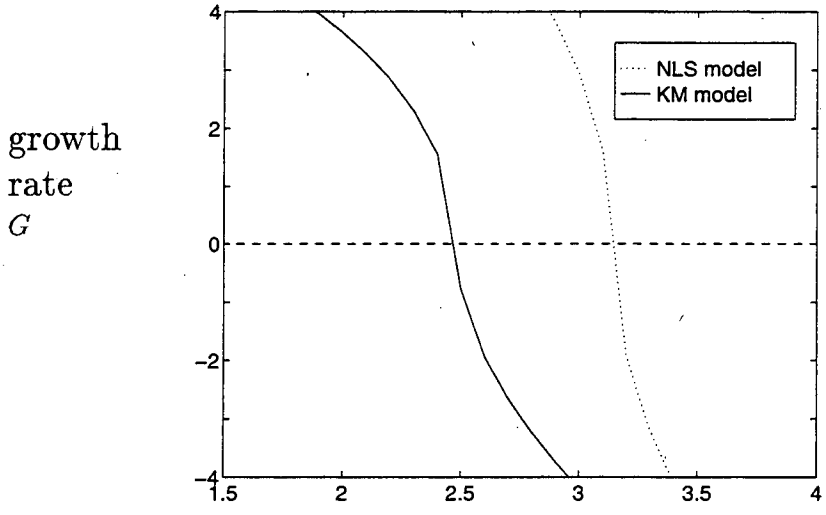

Figure 5.7: Stability diagram for sideband perturbations of the filament function of the helical wave. This figure is a local enlargement of Figure 4.2 with $\varepsilon = 0.309$. The x-axis is the initial amplitude of the filament function. The y-axis is the growth rate G. Instability occurs for negative G.

Let A denote the initial amplitude of the filament function of the helical wave. It is clear from Figure 5.7 that when $A = 2.3884$, both the NLS model and the KM model yield stable solutions; when $A = 2.8227$ or 3.0398, the KM model gives unstable solution and the NLS model still yields stable solution; when $A = 3.3655$, 4.3426, or 6.5139, both models generate unstable solutions. Figure 5.8, Figure 5.9, Figure 5.10, Figure 5.11, Figure

5.12 and Figure 5.13 present the time histories of the amplitudes of the modes $n = 8$, 9, 10, 11 for $A = 2.3884, 2.8227, 3.0398, 3.3655, 4.3426$ and 6.5139, respectively. For different values of A we observe stable, recurrent, and chaotic behaviors. Our numerical results agree very well with the stability diagram (Figure 5.7).

Our next numerical experiment is to study the maximum curvature. In Figure 5.14, Figure 5.15, Figure 5.16, Figure 5.17, Figure 5.18, and Figure 5.19 we plot the time histories of the maximum curvature corresponding to Figure 5.8, Figure 5.9, Figure 5.10, Figure 5.11, Figure 5.12, and Figure 5.13, respectively. The dashed lines correspond to the NLS model and the solid lines correspond to the KM model. As one can see from these figures, there is no high or narrow peak of the solid lines compared to the dashed lines, and this suggests that no hairpin structure is developed so far according to [60]. We shall confirm this again by studying the vortex filament curve of our model problem in the next subsection.

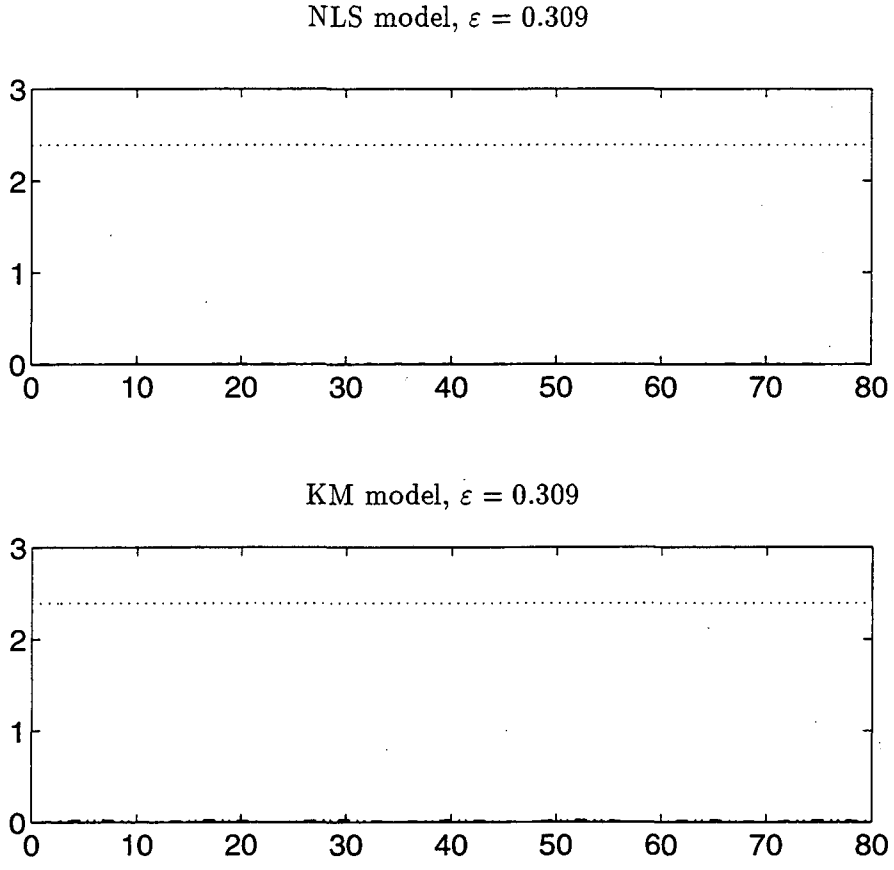

Figure 5.8: The sideband perturbations of the filament function of the helical wave with $A = 2.3884$, where A is the initial amplitude of the filament function.

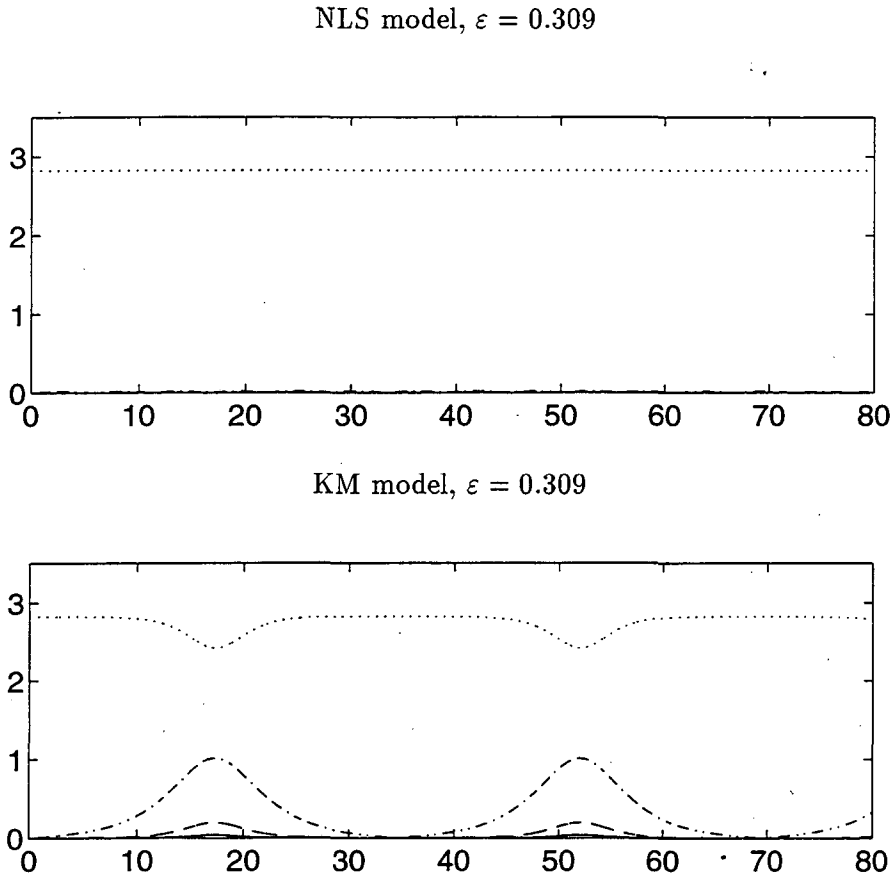

Figure 5.9: The sideband perturbations of the filament function of the helical wave with initial amplitude $A = 2.8227$.

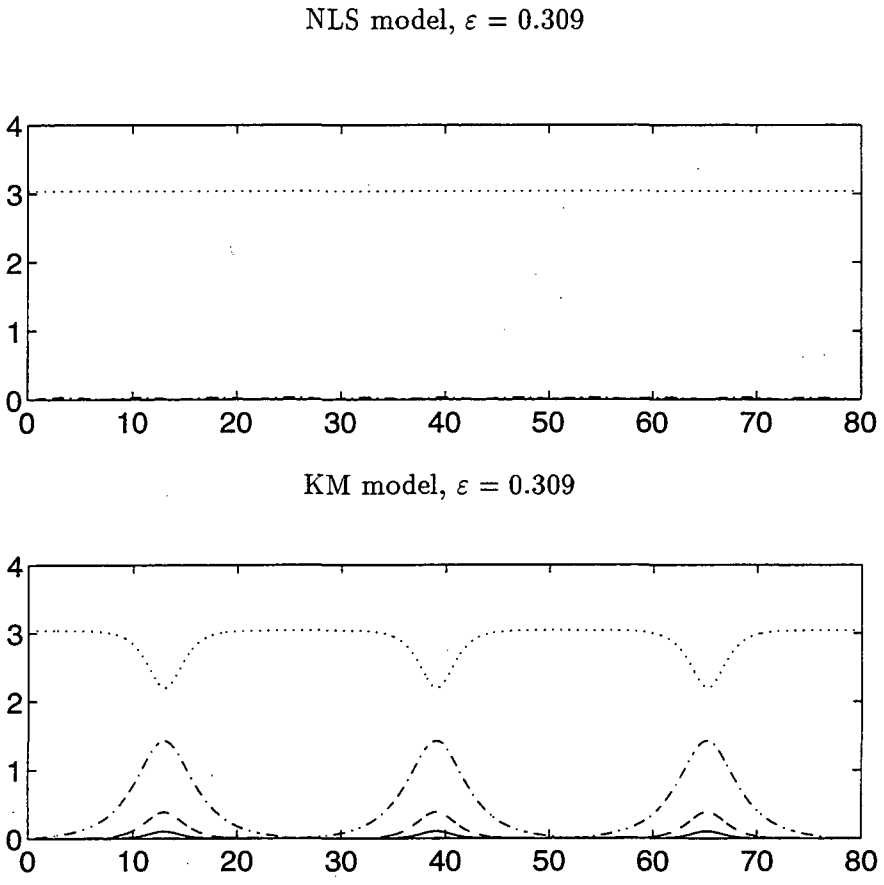

Figure 5.10: The sideband perturbations of the filament function of the helical wave with $A = 3.0398$.

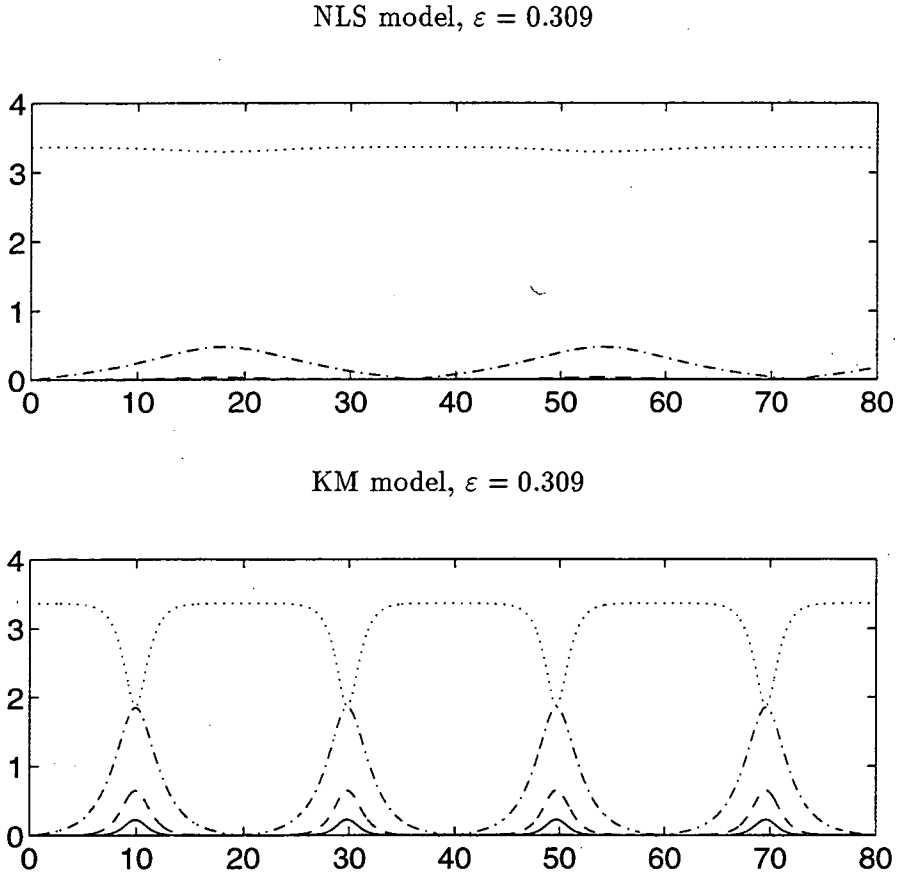

Figure 5.11: The sideband perturbations of the filament function of the helical wave with $A = 3.3655$.

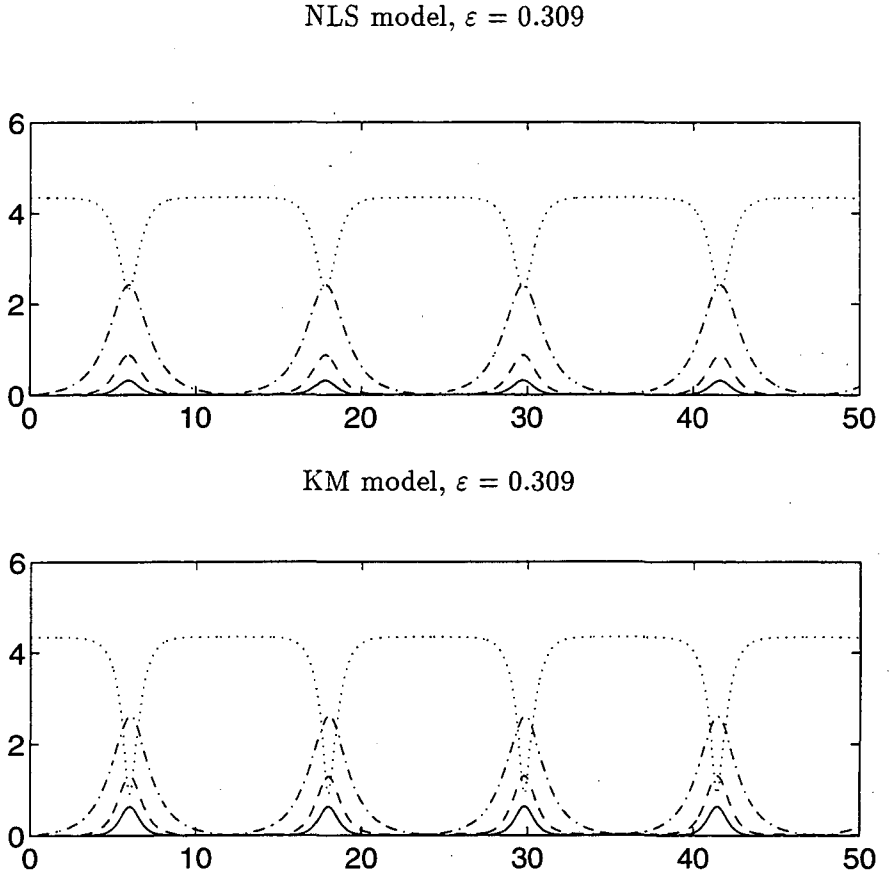

Figure 5.12: The sideband perturbations of the filament function of the helical wave with $A = 4.3426$.

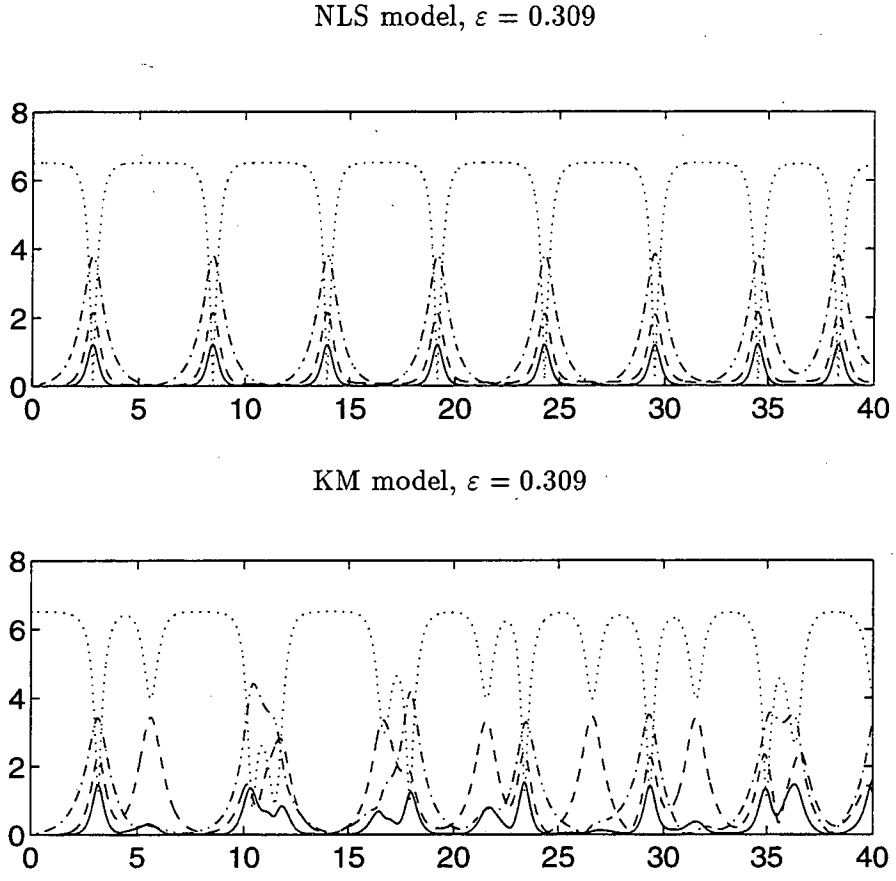

Figure 5.13: The sideband perturbations of the filament function of the helical wave with $A = 6.5139$.

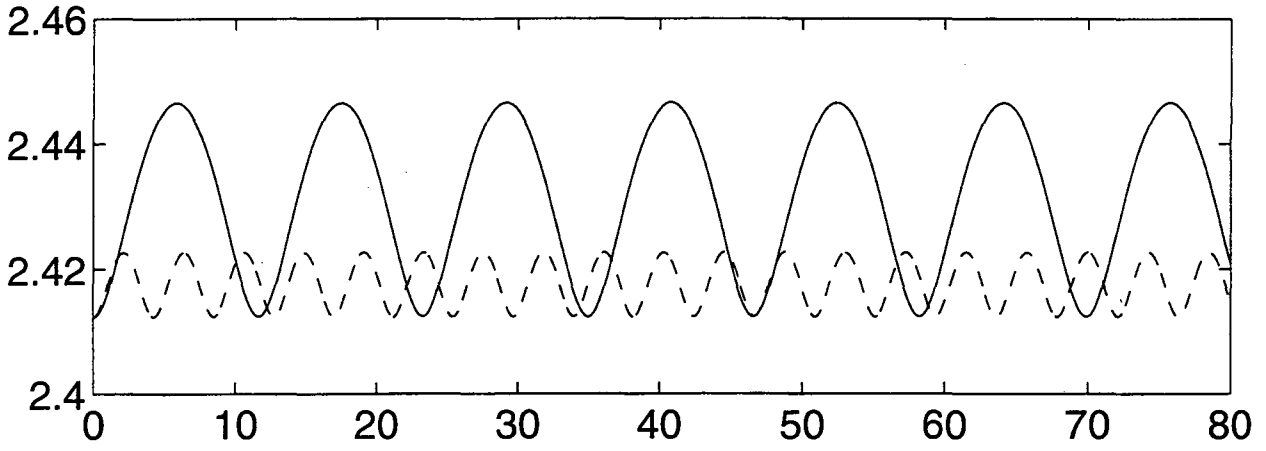

Figure 5.14: Time history of the maximum curvature corresponding to Figure 5.8. The dashed line denotes the NLS model and the solid line denotes the KM model.

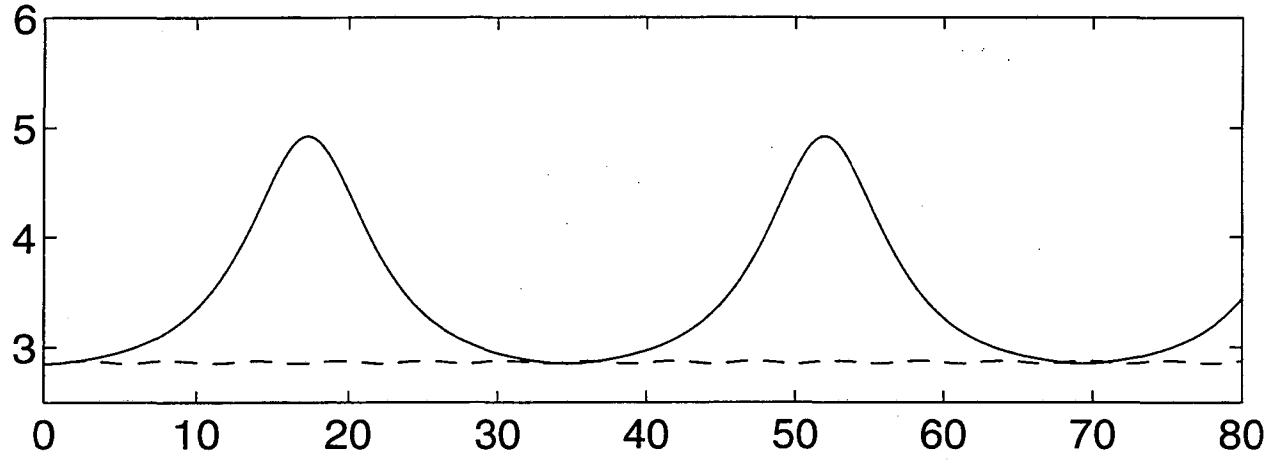

Figure 5.15: Time history of the maximum curvature corresponding to Figure 5.9. The solid line represents the KM model and the dashed line represents the NLS model.

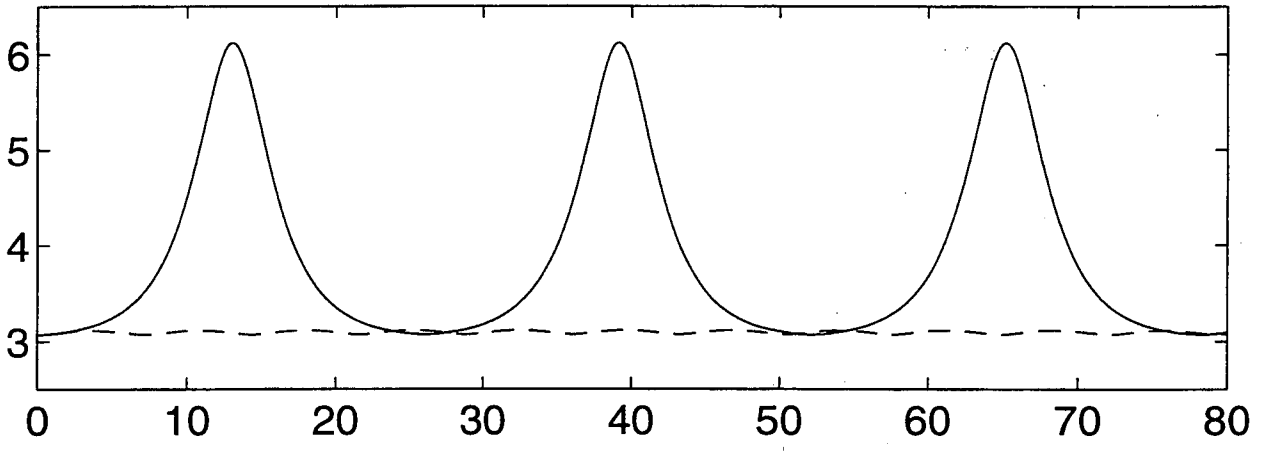

Figure 5.16: Time history of the maximum curvature corresponding to Figure 5.10. The solid line is for the KM model and the dashed line is for the NLS model.

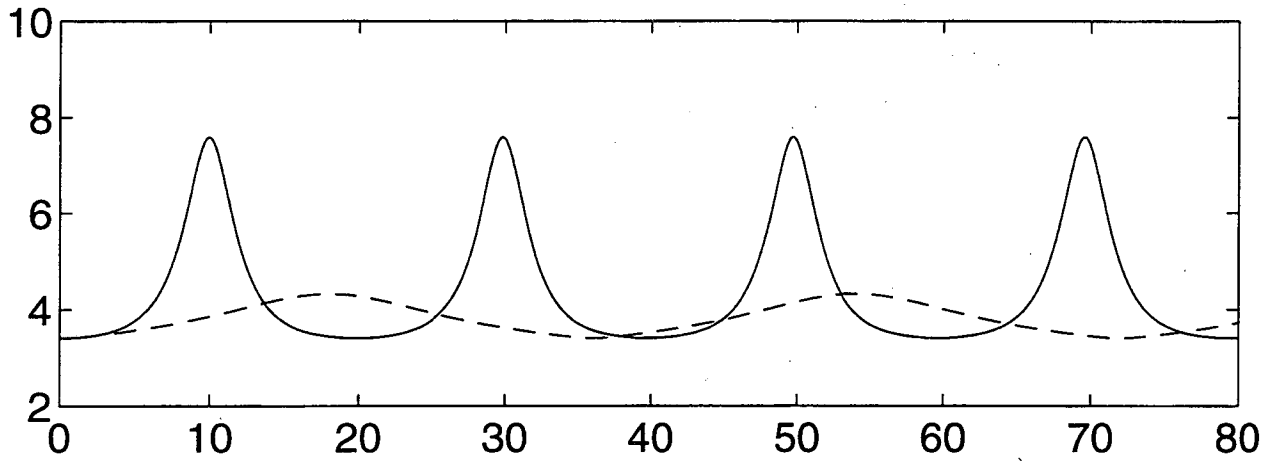

Figure 5.17: Time history of the maximum curvature corresponding to Figure 5.11. The solid line: the KM model; the dashed line: the NLS model.

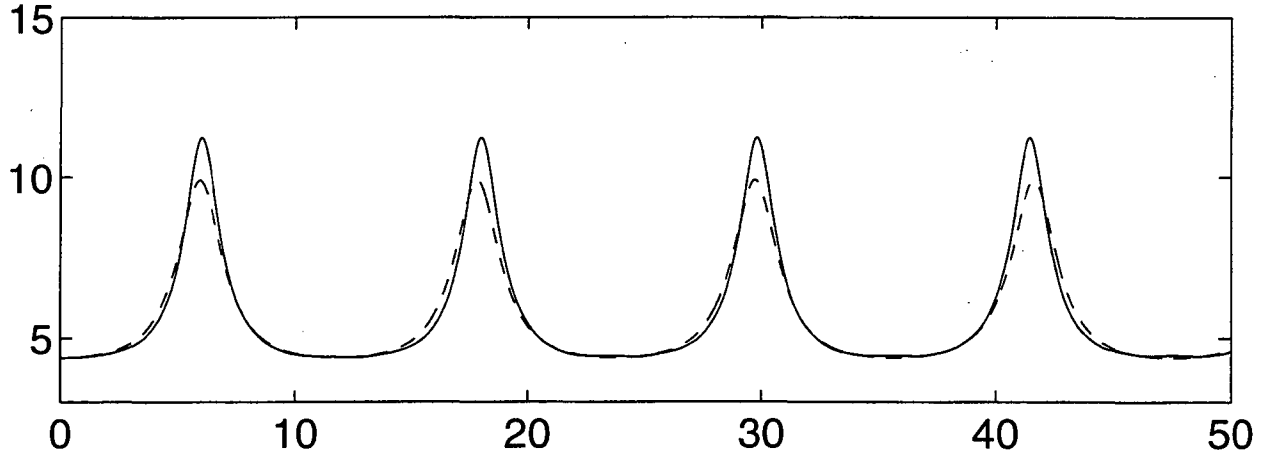

Figure 5.18: Time history of the maximum curvature corresponding to Figure 5.12. The solid line represents the KM model and the dashed line represents the NLS model.

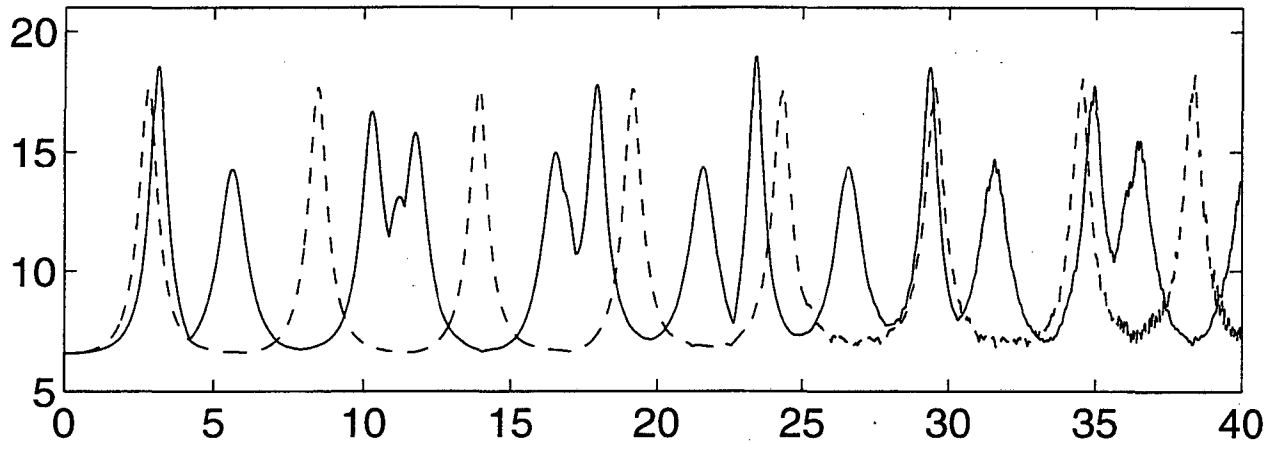

Figure 5.19: Time history of the maximum curvature corresponding to Figure 5.13. The solid line denotes the KM model and the dashed line denotes the NLS model.

5.6.2 Numerical Experiments for the Filament Curve

We have studied the sideband perturbation of the filament function numerically. Now we study the vortex filament curve directly.

In Figure 5.21 we present the evolution of the Kelvin waves according to the Klein-Majda equation with $\varepsilon = 0.309$. Initially we use 257 points to represent the vortex filament between the walls. Since we are not interested in the absolute positions of the vortex filament, we can avoid some calculations by fixing $\mathbf{r}(0,t)$,$\mathbf{t}(0,t)$ and $\mathbf{N}(0,t)$. In our calculations, we set $\mathbf{t}(0,t) = (1,0,0)$, $\mathbf{N}(0,t) = (0,-1,i)$ and $\mathbf{r}(0,t) = \mathbf{r}(0,0)$. No hairpin structure is observed, consistent with the predictions before.

Figure 5.22 demonstrates the time evolution of the arc length and energy. It shows the conservation of these two quantities.

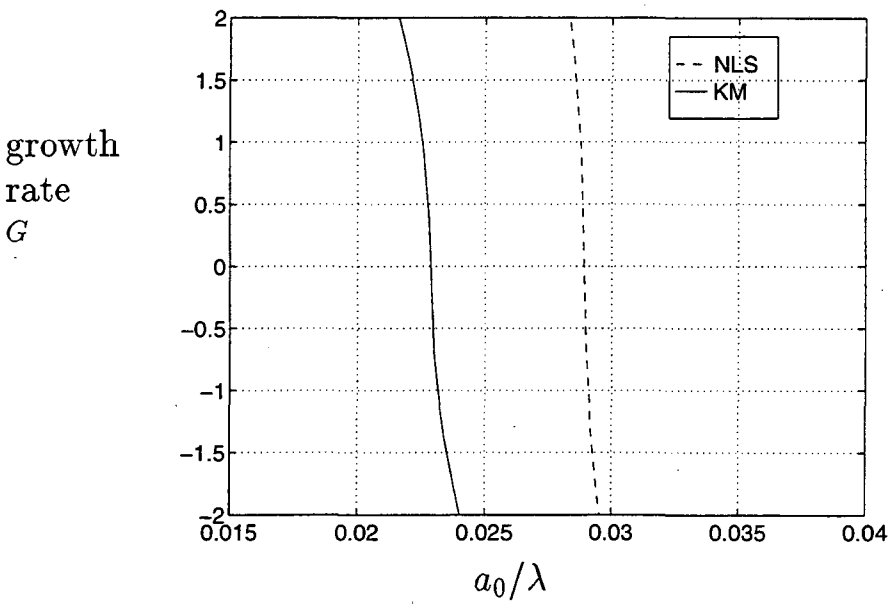

Figure 5.20: Stability diagram for sideband perturbations of our model problem. This figure is a local enlargement of Figure 4.3 with $\varepsilon = 0.309$. Instability occurs for negative G.

In a set of figures (from Figure 5.23 to Figure 5.27) we give the time evolution of the amplitudes of the main harmonic and its sidebands with $a_0/\lambda = 0.02, 0.025, 0.035, 0.04$, and 0.06 at time $t = 0$. We present the results for both the NLS model and the KM model. We observe stable, recurrent and chaotic behaviors respectively. Our numerical results are in good agreement with the analytical results of the stability analysis (see Figure 5.20).

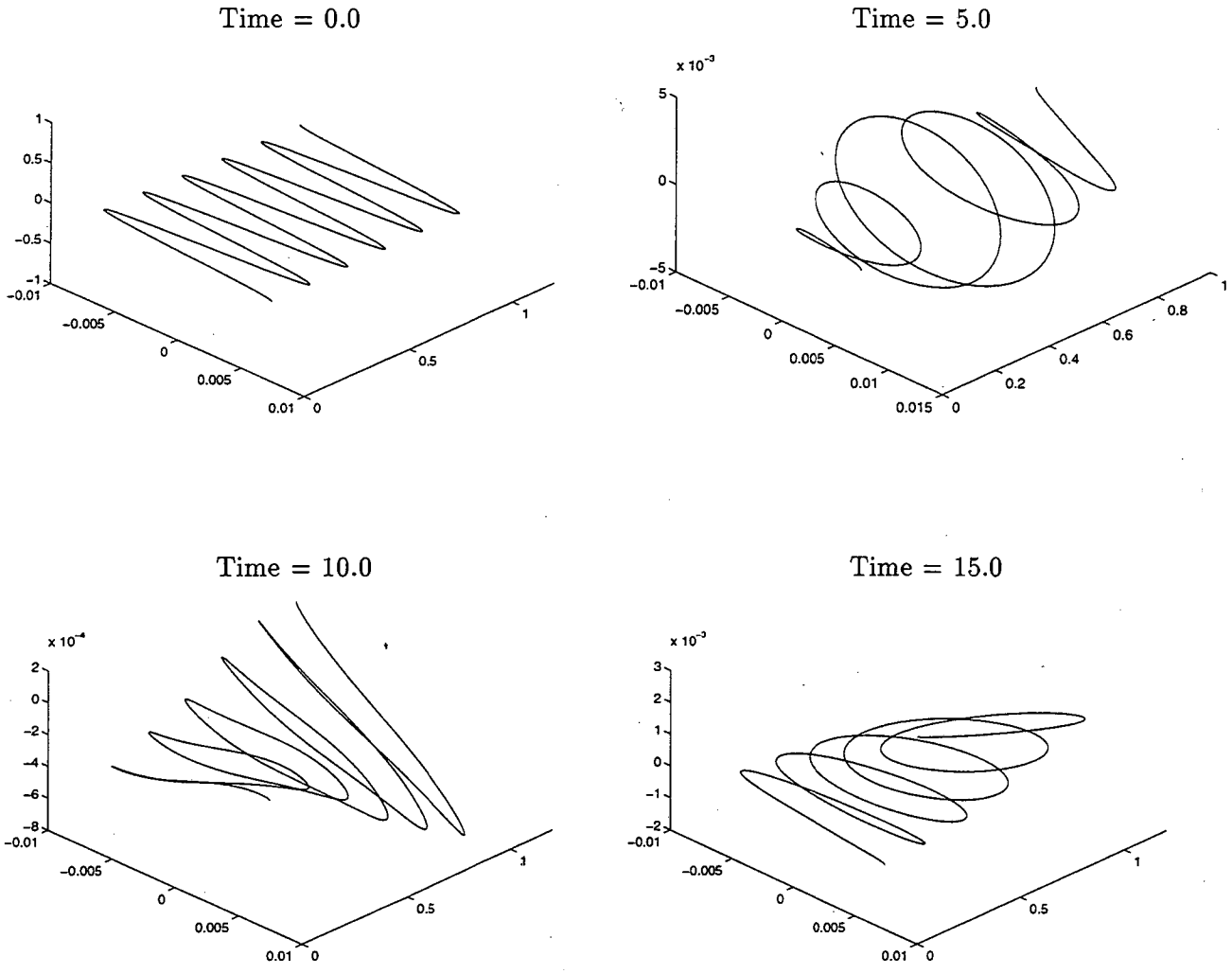

Figure 5.21: Motion of the Kelvin waves according to the Klein-Majda equation: $\varepsilon = 0.309$, $a_0/\lambda = 0.04$.

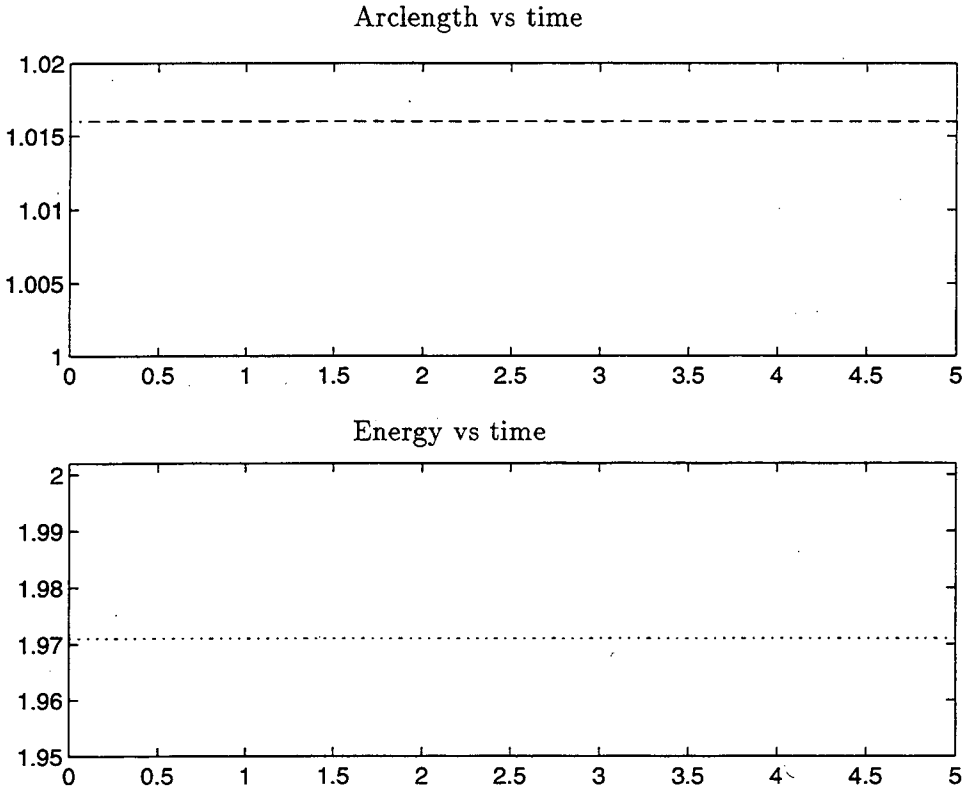

Figure 5.22: Approximate conservation of invariants for the Klein-Majda equation with $a_0/\lambda = 0.04, \varepsilon = 0.309$.

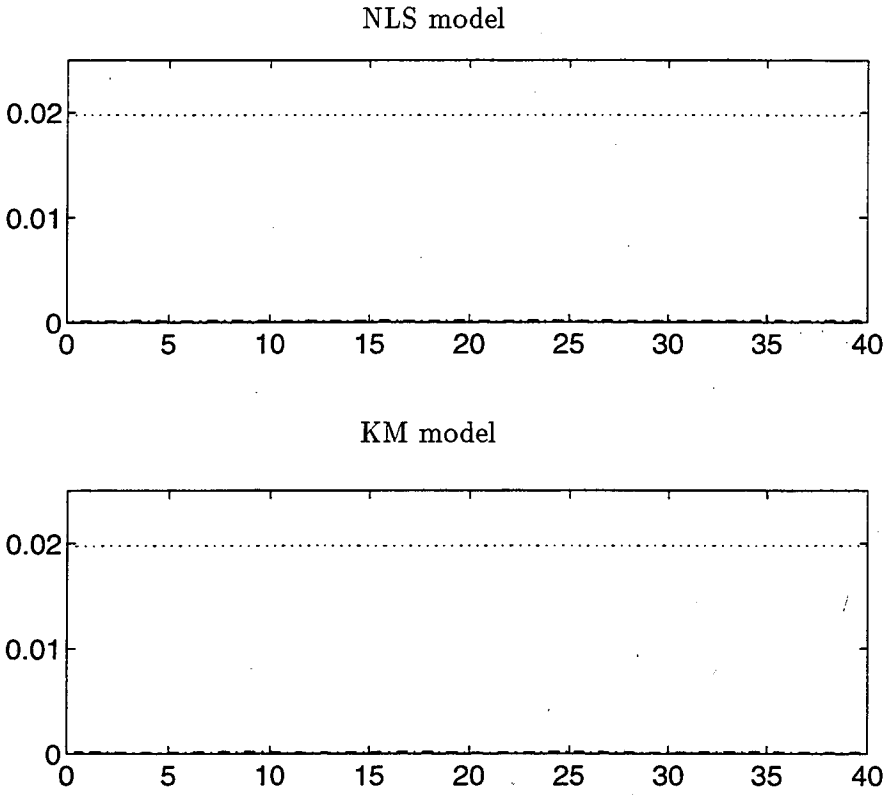

Figure 5.23: Sideband instability for the Kelvin waves where $a_0/\lambda = 0.02$ at time $t = 0.0$ and $\varepsilon = 0.309$. The x-axis is the scaled amplitudes of interested modes ($n = 8, 9, 10, 11$) of the filament curve. The y-axis is time.

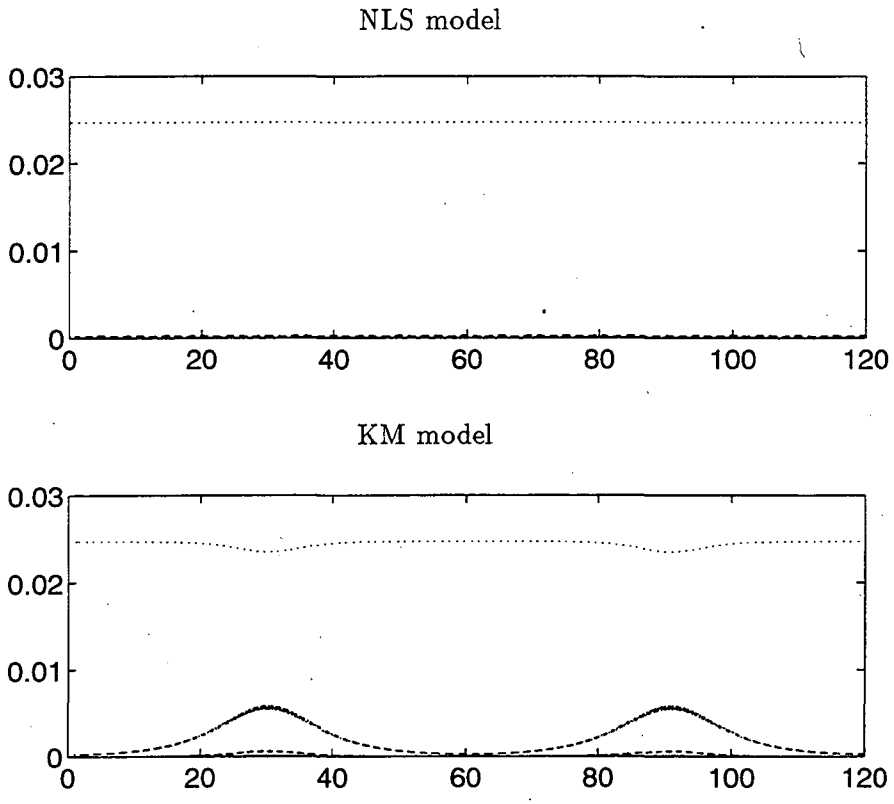

Figure 5.24: Sideband instability for the Kelvin waves where $a_0/\lambda = 0.025$ initially and $\varepsilon = 0.309$.

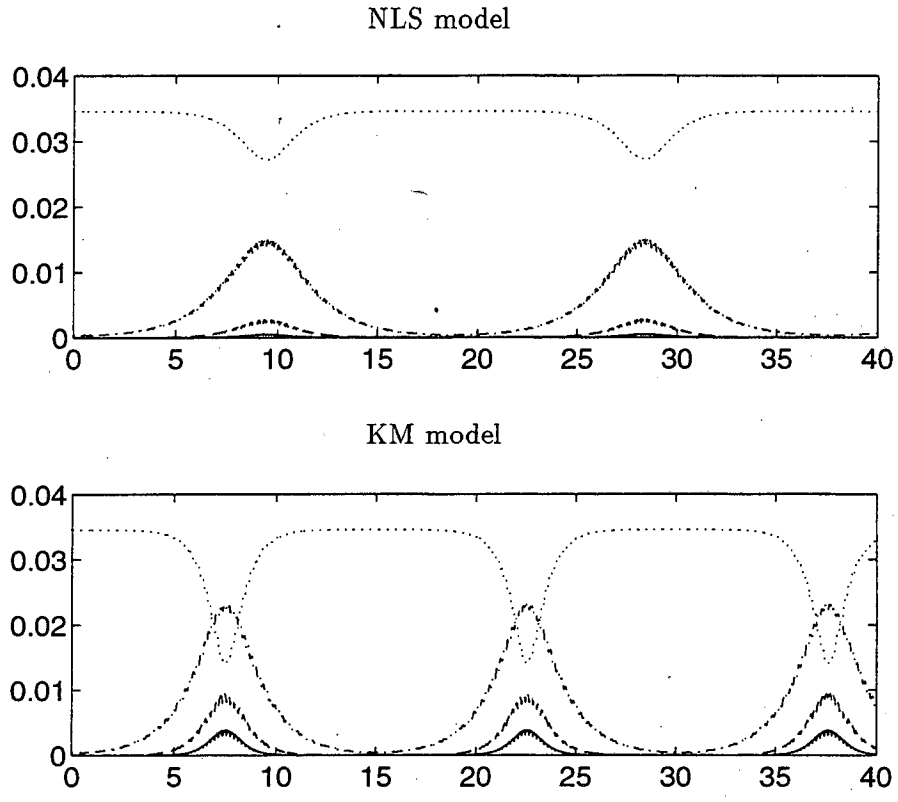

Figure 5.25: Sideband instability for the Kelvin waves where $a_0/\lambda = 0.035$ initially and $\varepsilon = 0.309$.

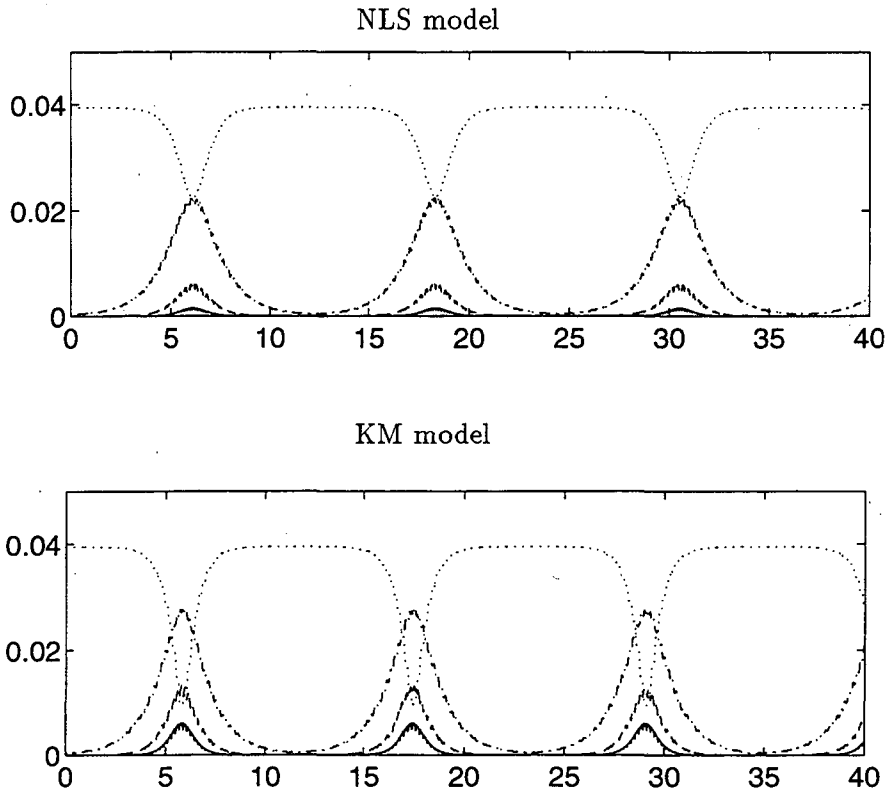

Figure 5.26: Sideband instability for the Kelvin waves where $a_0/\lambda = 0.04$ initially and $\varepsilon = 0.309$.

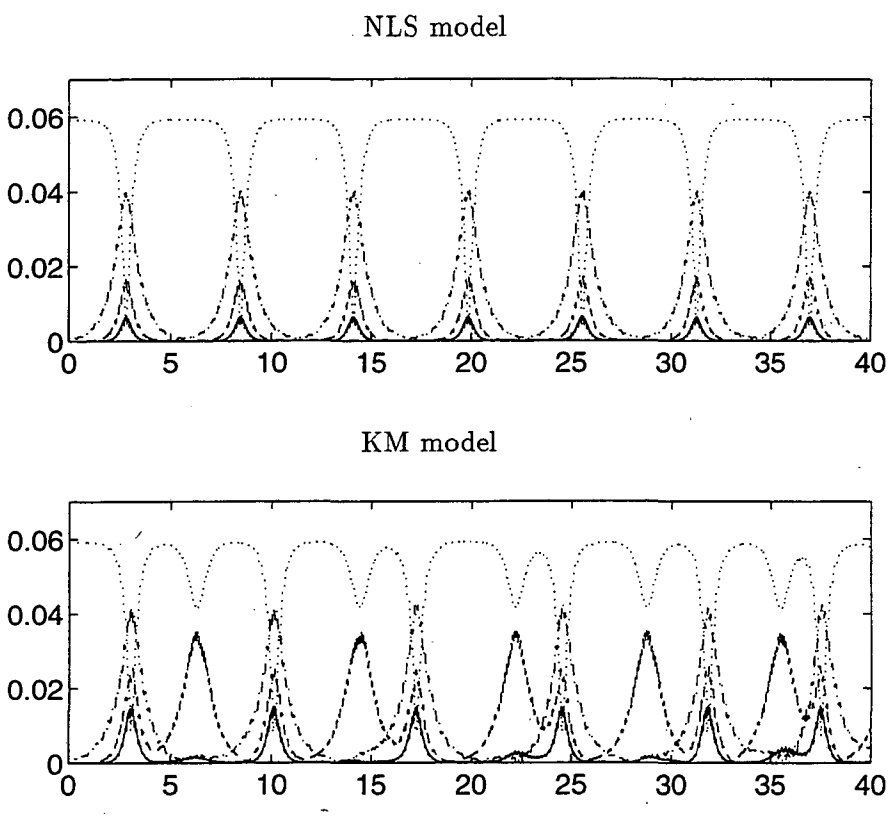

Figure 5.27: Sideband instability for the Kelvin waves where $a_0/\lambda = 0.06$ initially and $\varepsilon = 0.309$.

5.7 Numerical Results with the Klein-Knio Equation

We present our numerical results with the Klein-Knio equation in this section.

In Figure 5.28 we show the evolution of the vortex filament in the model problem where the ratio of the physical core size and the distance between the walls is: $\alpha = 10^{-5}$. We choose the initial vortex filament with $a_0/\lambda = 0.04$. The filament evolves smoothly and hairpin structure is not observed. We plot the total arc length and energy against time in Figure 5.29. Again, the total length is conserved and there is no stretching. In Figure 5.30 and 5.31 we show the dynamic behaviors with $a_0/\lambda = 0.02, 0.04, 0.06, 0.08$ initially. We obtain stable, recurrent and chaotic phenomena respectively.

In Figure 5.32, we compare the solution of the LIA and the Klein-Knio equation for $a_0/\lambda = 0.03$. We find that the Klein-Knio equation gives stable behavior, whereas the LIA gives unstable behavior. This indicates that the stability region of the Klein-Knio equation is larger than that of the LIA.

Figure 5.33 and Figure 5.34 illustrate the dynamics behaviors of the vortex filament retaining the same shape as the Kelvin waves but with a thicker core. The parameter α here is 10^{-4}. Stable, recurrent, and chaotic behaviors are also observed.

To understand the relationship between the stability region of the Klein-Knio equation and the core size, we study the dynamic behaviors for different values of α (= core size/distance between the walls). In Figure 5.35 we plot the evolution of amplitudes of the main wave and its sidebands for $\alpha = 10^{-5}$, 10^{-4}, 10^{-3} with $a_0/\lambda = 0.04$ initially. When $\alpha = 10^{-5}$, the behavior is recurrent; when $\alpha = 10^{-4}$, the behavior is also recurrent but the growth rate or the decreasing rate of the amplitudes is smaller than that of a thinner one; when $\alpha = 10^{-3}$, the behavior is stable. Figure 5.35 implys that as the core gets thicker, the stability region of the Klein-Knio equation becomes larger.

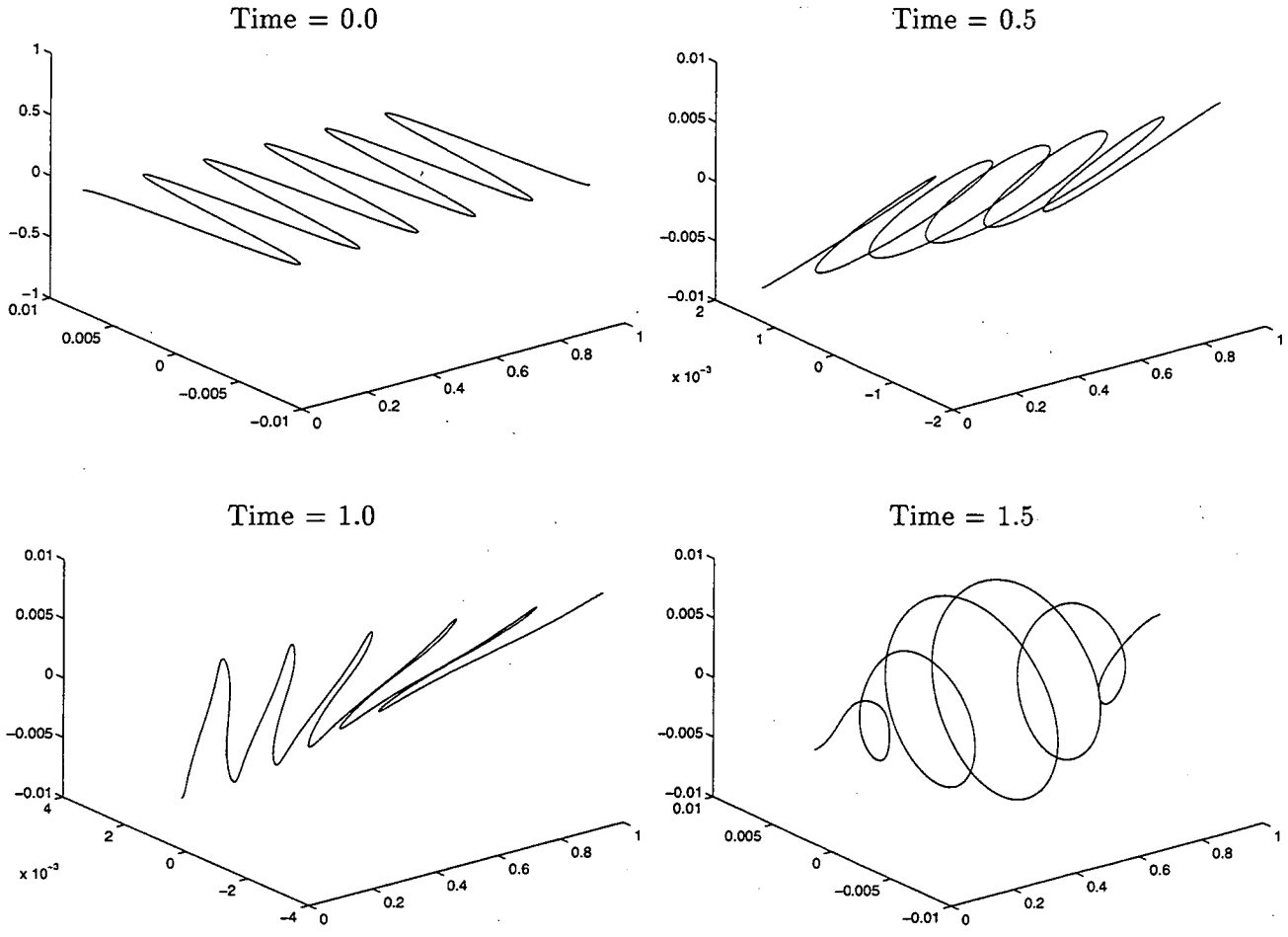

Figure 5.28: Evolution of Kelvin waves following the Klein-Knio equation.

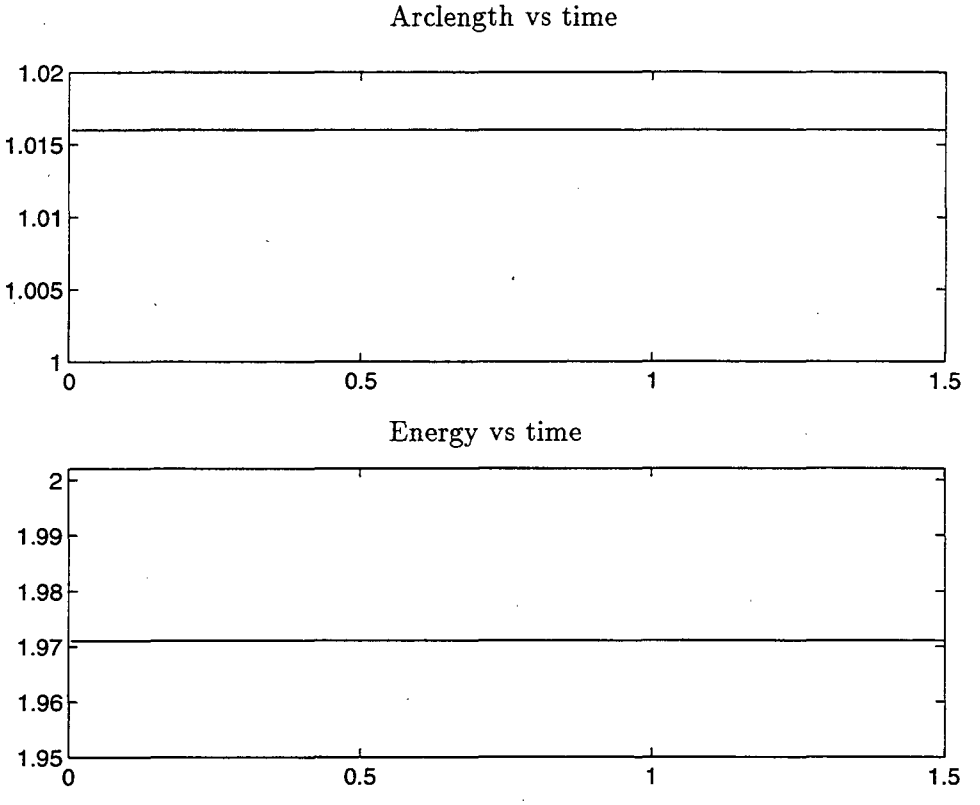

Figure 5.29: Approximate conservation of invariants for the Klein-Knio equation with $a_0/\lambda = 0.04$ at time $t = 0$.

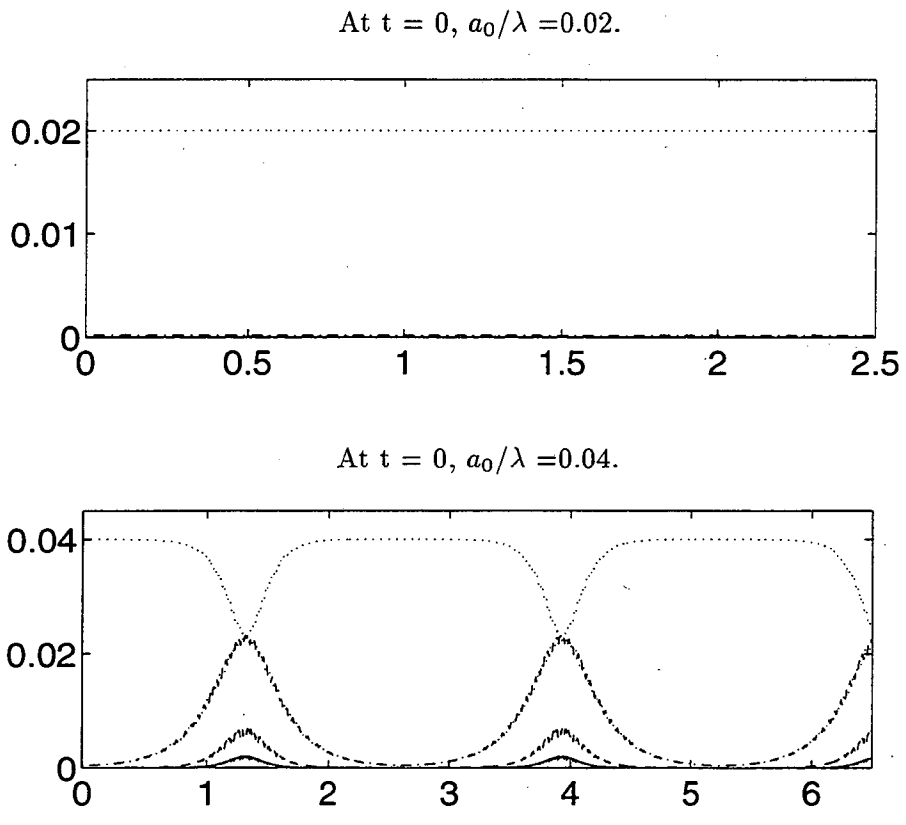

Figure 5.30: Sideband instability and stable, recurrent phenomenon for Kelvin waves following the Klein-Knio equation. The amplitudes of the main harmonic and the lower harmonics are plotted as a function of time.

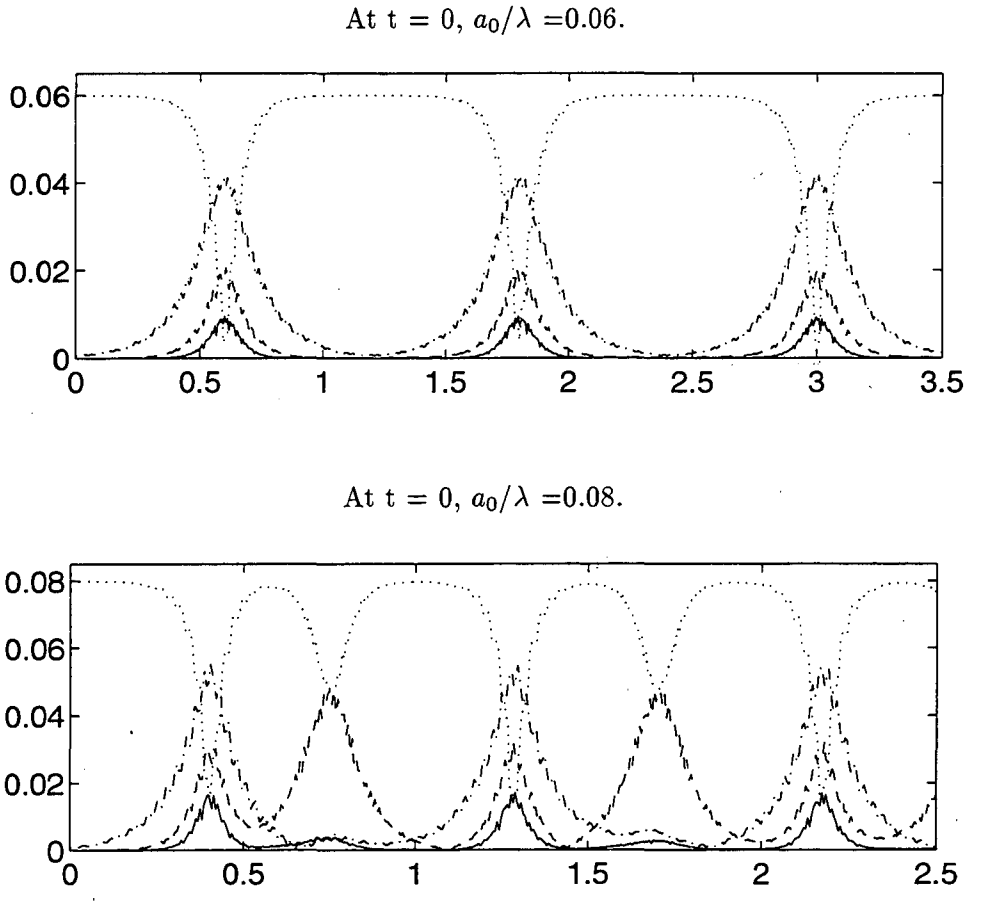

Figure 5.31: Sideband instability and recurrent, chaotic phenomenon for Kelvin waves following the Klein-Knio equation.

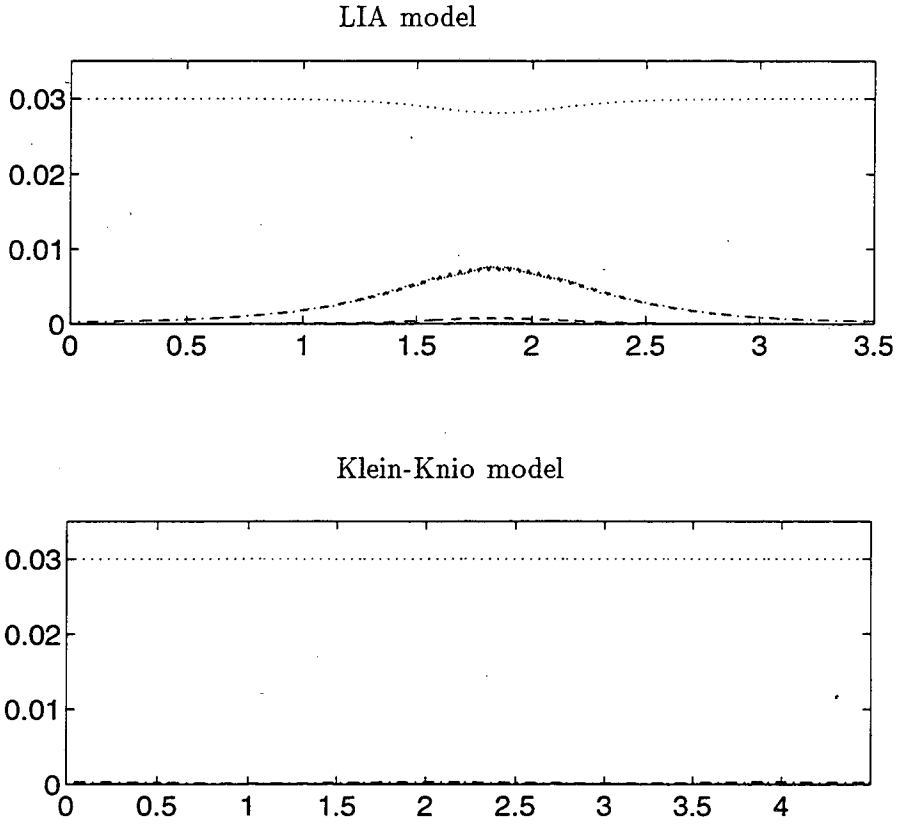

Figure 5.32: Comparison of the LIA and the KK. This plot shows that the stability region of the Klein-Knio equation is larger than the LIA for the model problem.

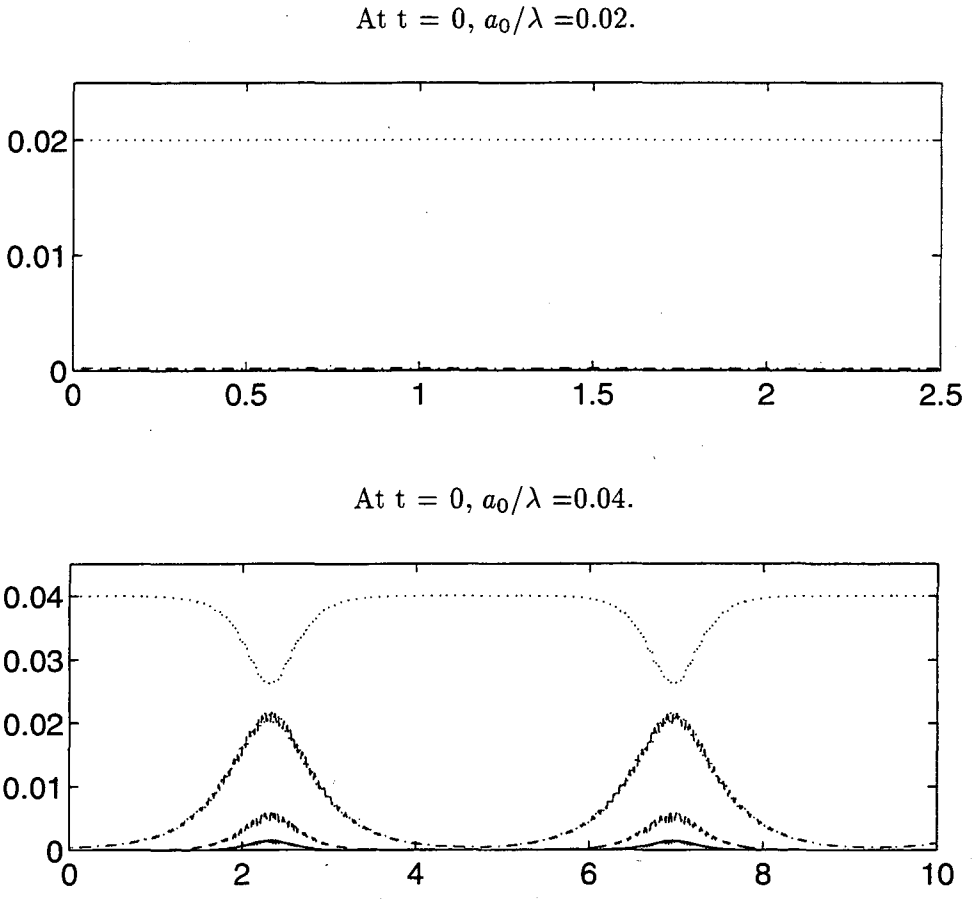

Figure 5.33: Sideband instability and stable, recurrent phenomenon for a thicker filament by the Klein-Knio equation.

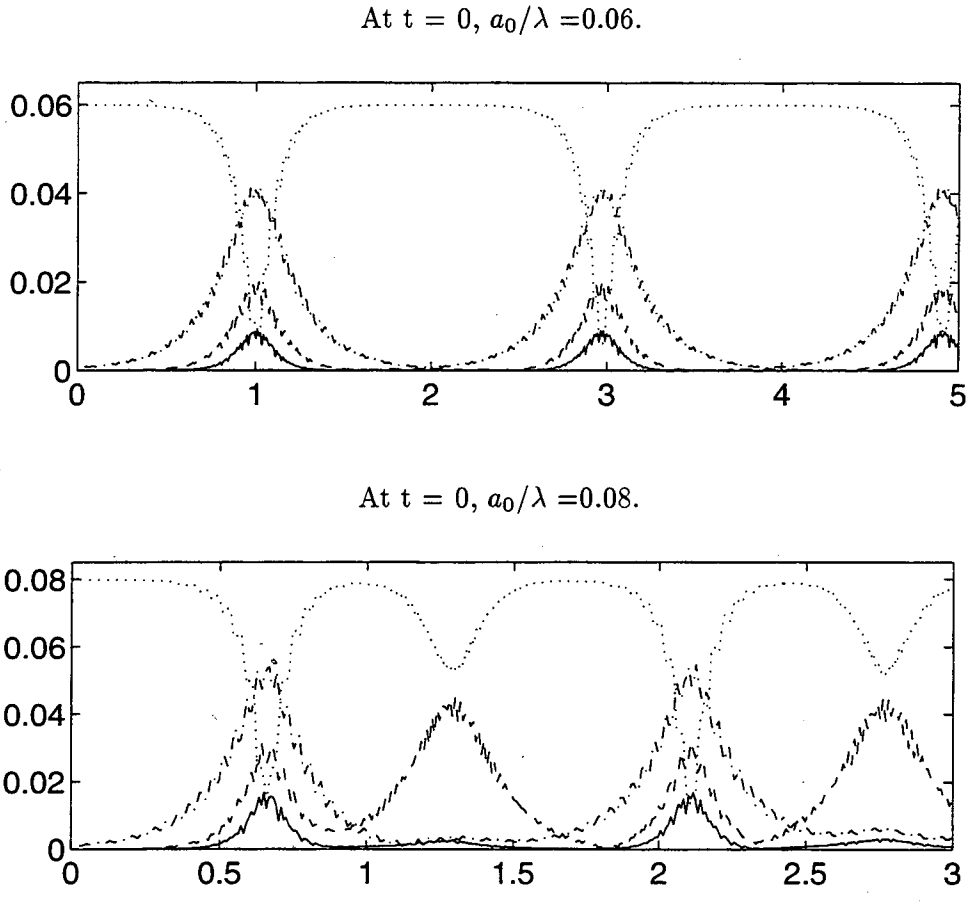

Figure 5.34: Sideband instability and recurrent, chaotic phenomenon for a thicker filament by the Klein-Knio equation.

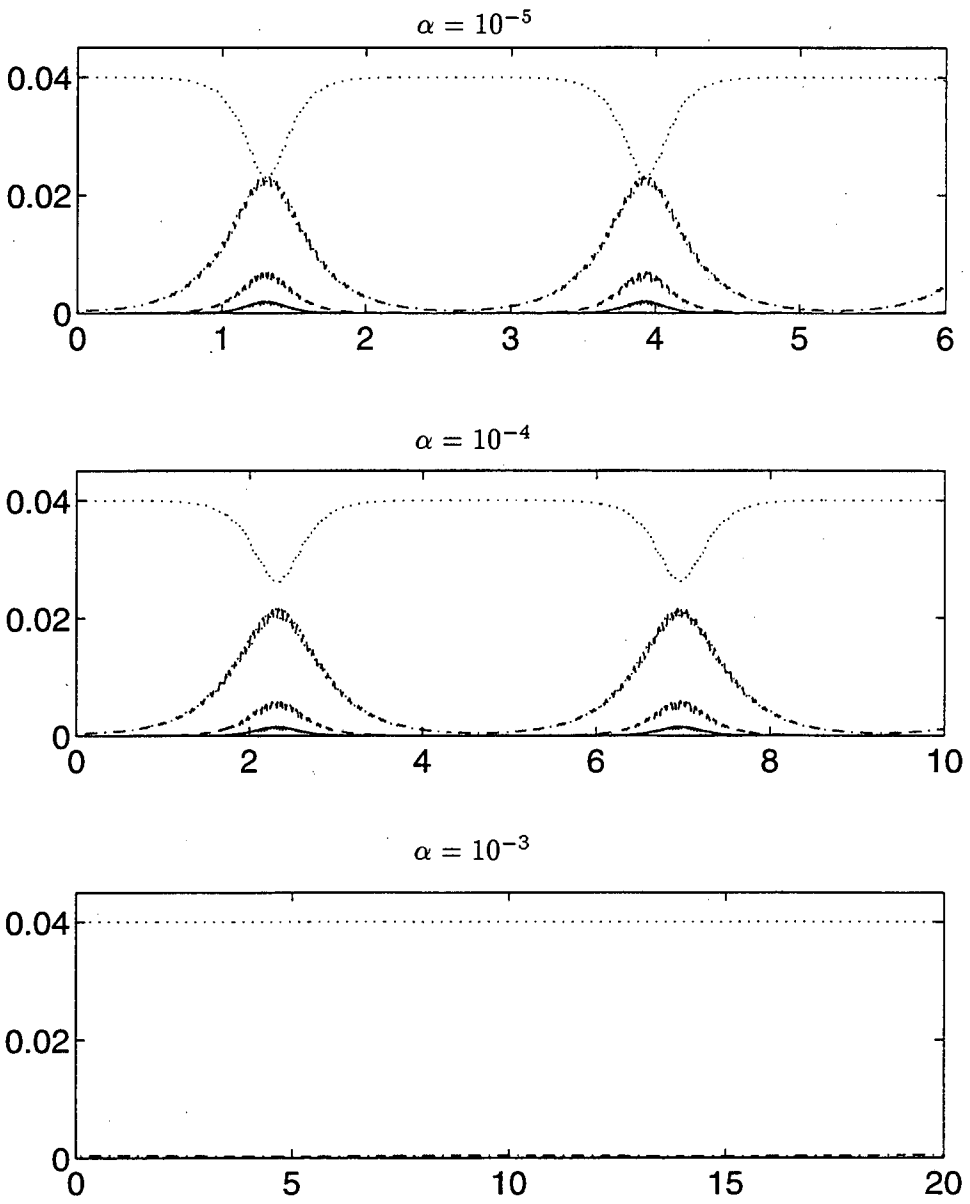

Figure 5.35: Comparison of the dynamic behaviors by the Klein-Knio equation for different core sizes where $a_0/\lambda = 0.04$ at time $t = 0$. Here the parameter α denotes the ratio of the core size to the distance between the walls.

At this point, we have gained a clear picture of the three kinds of model equations for thin vortices. For our model problem, they present similar behaviors but their stability regions are different. In particular, the stability regions of the Klein-Majda equation and the Klein-Knio equation depends on the core size of the vortex filament. When the core size is large enough, the Klein-Majda equation always gives stable behavior.

Chapter 6

Analysis of Biot-Savart Vortex Models

In the previous chapters we have discussed various numerical methods for a single thin vortex filament and studied the sideband instabilities of Kelvin waves in superfluid helium. For comparison purposes, in this chapter we want to examine whether similar behaviors appear in classical vortices.

The organization of the chapter is as follows. Section 6.1 introduces the Biot-Savart vortex models. Section 6.2 discusses a numerical method to calculate energy. Section 6.3 presents numerical observations.

6.1 Biot-Savart Vortex Models

Biot-Savart vortex models, also called vortex methods in the numerical analysis literature, are numerical techniques for analyzing and computing vortex motion. For theoretical, numerical, computational, and physical aspects of vortex methods, see Beale and Majda [10], [11], Chorin [28], Leonard [68], [69], Puckett [83], Sethian [97], [98], Sethian and Ghoniem [99]. For fast vortex methods, see Almgren, Buttke, and Colella [4] and references therein. In this section section we just give a quick look at the vortex filament method.

Instead of using a single filament to approximate the vorticity field ω, we use a finite collection of vortex filaments C_i $(i = 1, ..., N)$ to approximate ω and each C_i has individual finite cross section and circulation Γ_i. The vortex filaments are closely spaced, so that their cores overlap. In this way, a smooth vorticity field can be represented by the

vortex filaments (see Figure 6.1).

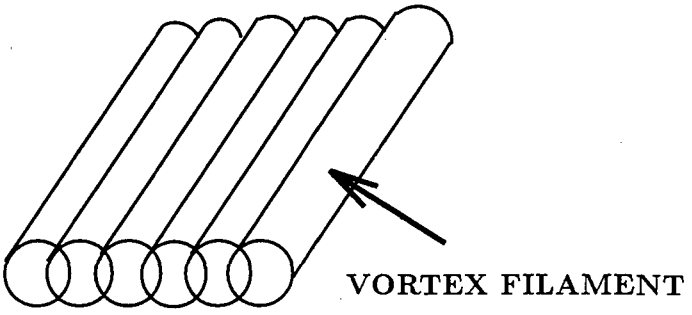

Figure 6.1: A smooth distribution of vorticity, represented by a collection of overlapping vortex filaments.

For the purposes of discretization along the vortex filaments, each of the filament C_i is approximated by n_i segments. Each segment is a circular cylinder of length s_{j_i} and radius σ_{j_i} $(j_i = 1, ..., n_i)$. Ensure that the lengths of all segments are less than h, which is a predetermined bound. In other words, when the length of a segment exceeds h, accuracy may be lost and therefore the segment is broken into two halves of equal lengths and cross sections. The new coordinates are obtained by linear interpolation. In this way, vortex stretching is implicitly accounted for. To make life easy, pick all Γ_i equal, $\Gamma_i = \Gamma$ for all i.

Let $\mathbf{x}_i^c$ be the center of the i-th segment. The velocity at a point $\mathbf{x}$ is the following discrete version of (2.16):

$$\mathbf{u}(\mathbf{x},t) = -\frac{\Gamma}{4\pi}\sum_i \frac{(\mathbf{x}_i^c - \mathbf{x}) \times (\mathbf{x}_{i+1} - \mathbf{x}_i)}{|\,\mathbf{x}_i^c - \mathbf{x}\,|^3}\; f(\frac{|\,\mathbf{x}_i^c - \mathbf{x}\,|}{\sigma}) \tag{6.1}$$

where the sum is over all segments on all filaments, f is a core function chosen so as to enhance accuracy [12], [48], and σ is the cutoff size that can serve as a measure of the thickness of the filaments and is invariant in time. σ should be greater than the typical distance between neighboring segments.

There are many choices for f. For example,

$$f_2(r) = 1 - e^{-r^3} \tag{6.2}$$

is a core function which has second order accuracy and

$$f_4(r) = 1 + (\frac{3}{2}r^3 - 1)e^{-r^3} \tag{6.3}$$

is one having fourth order accuracy.

At each time step, once the fluid velocity $\mathbf{u}(\mathbf{x})$ is known, one can use a fourth-order Runge-Kutta method to solve the ODEs

$$\frac{d\mathbf{x}}{dt} = \mathbf{u} \tag{6.4}$$

with time step control

$$\triangle t \ \max_j \mid \mathbf{u}_j^n \mid \leq C, \tag{6.5}$$

where $\triangle t$ is the time step and C is a predetermined tolerance. One can also use an imbedded Runge-Kutta method to solve the ODE (6.4) where time step dt is controlled by the error tolerance.

To conclude vortex filament method, we want to mention some numerical difficulties underlying the method. Since it requires the evaluation of the effect that every vortex segment has upon all the other ones in the flow field, the direct evaluation requires $O(n^2)$ operations per time step for obtaining the velocities, where n is the overall number of segments

$$n = \sum_{i=1}^{N} n_i. \tag{6.6}$$

By contrast, advancing the nodes over the time step takes only $O(n)$ operations, hence the velocity computation (6.1) is the most expensive component of the algorithm. The $O(n^2)$ operation count leads to a rapid increase in CPU time per time step as the discretization is refined or additional nodes are introduced due to vortex stretching. Furthermore, the generation of smaller and smaller scales in inviscid flows usually leads to larger and larger acceleration of the nodes, thereby necessitating smaller time steps. A technique of hairpin removal has been proposed by Chorin [24], [27] to overcome this difficulty.

6.2 Evaluation of Energy for the Biot-Savart Vortex Models

This section presents a numerical scheme for evaluating the energy (3.98).

Denote $\mathbf{x}_i^c$ the center of the i-th segment $\delta\mathbf{l}_i$, Γ_i the circulation. The energy (3.98) can be computed as

$$E = \frac{1}{8\pi}\int_0^L dx \int_{x-\frac{L}{2}}^{x+\frac{L}{2}} dx' \int_{-\infty}^{\infty}\int_{-\infty}^{\infty} dydz \int_{-\infty}^{\infty}\int_{-\infty}^{\infty} dy'dz'$$

$$\sum_{j\neq 0}\left(\frac{1}{(\mid \mathbf{x}-\mathbf{x}'-j(L,0,0)\mid}-\frac{1}{(\mid j\mid +1)L}\right)\boldsymbol{\omega}(\mathbf{x}')\cdot\boldsymbol{\omega}(\mathbf{x})$$

$$+\quad \frac{1}{8\pi}\int_0^L dx\int_{x-\frac{L}{2}}^{x+\frac{L}{2}}dx'\int_{-\infty}^{\infty}\int_{-\infty}^{\infty}dydz\int_{-\infty}^{\infty}\int_{-\infty}^{\infty}dy'dz'$$

$$\frac{1}{\mid \mathbf{x}-\mathbf{x}'\mid}\,\boldsymbol{\omega}(\mathbf{x}')\cdot\boldsymbol{\omega}(\mathbf{x})$$

$$+\quad \frac{1}{8\pi L}\int_0^L dx\int_{x-\frac{L}{2}}^{x+\frac{L}{2}}dx'\int_{-\infty}^{\infty}\int_{-\infty}^{\infty}dydz\int_{-\infty}^{\infty}\int_{-\infty}^{\infty}dy'dz'\;\boldsymbol{\omega}(\mathbf{x}')\cdot\boldsymbol{\omega}(\mathbf{x})$$

$$\equiv\quad T_1+T_2+T_3 \tag{6.7}$$

To calculate T_1 in (6.7), with a change of variable

$$x'\rightarrow x'+\frac{L}{2}-x, \tag{6.8}$$

we first perform the following integration

$$\begin{aligned}
T_1 &= \frac{1}{8\pi}\int_0^L dx\int_0^L dx'\int_{-\infty}^{\infty}\int_{-\infty}^{\infty}dydz\int_{-\infty}^{\infty}\int_{-\infty}^{\infty}dy'dz' \\
&\quad \sum_{j\neq 0}\left(\frac{1}{\sqrt{(-x'-jL+\frac{L}{2})^2+(y'-y)^2+(z'-z)^2}}-\frac{1}{(|j|+1)L}\right)\boldsymbol{\omega}(\mathbf{x}')\cdot\boldsymbol{\omega}(\mathbf{x}) \\
&= \frac{1}{8\pi}\sum_i\sum_j\sum_{k\neq 0}\left[\frac{1}{\sqrt{(x'^c-\frac{L}{2}+kL)^2+(y'^c-y^c)^2+(z'^c-z^c)^2}}-\frac{1}{(|k|+1)L}\right] \\
&\quad \Gamma_i\Gamma_j\delta\mathbf{l}_i\cdot\delta\mathbf{l}_j \\
&= \frac{1}{8\pi}\sum_i\sum_j K\left(\frac{x'^c}{L},\frac{1}{L}\sqrt{(y'^c-y^c)^2+(z'^c-z^c)^2}\right)\Gamma_i\Gamma_j\delta\mathbf{l}_i\cdot\delta\mathbf{l}_j,
\end{aligned} \tag{6.9}$$

where the function

$$K(x,r)=\frac{1}{L}\sum_{k\neq 0}\left(\frac{1}{\sqrt{(x-\frac{1}{2}+k)^2+r^2}}-\frac{1}{|k|+1}\right) \tag{6.10}$$

can be calculated once and for all and a set of values is stored. A specific value of $K(x,r)$ in the computation can be obtained by interpolation from the stored values. In our calculation we use a second-order interpolation scheme in two dimensions. Consider that we want to interpolate a scalar function $g(x,y)$ onto position $P(x,y)$ from an interpolation stencil of a lattice grid with mesh spacing h in x-direction and mesh spacing k in y-direction. Assume P lies inside the square $P_1P_2P_3P_4$ as drawn in Figure 6.2.

Let A_i (i = 1,2,3,4) be the area of each shaded region and $A = A_1 + A_2 + A_3 + A_4$ be the total area. The interpolation scheme can be written

$$g(x,y)=\frac{A_3}{A}g(x_1,y_1)+\frac{A_4}{A}g(x_2,y_2)+\frac{A_1}{A}g(x_3,y_3)+\frac{A_2}{A}g(x_4,y_4), \tag{6.11}$$

where

$$A_1 = (x_3 - x)(y_3 - y), \tag{6.12}$$

$$A_2 = (x_4 - x)(y - y_4), \tag{6.13}$$

$$A_3 = (x_1 - x)(y_1 - y), \tag{6.14}$$

$$A_4 = (x - x_2)(y_2 - y), \tag{6.15}$$

$$A = hk. \tag{6.16}$$

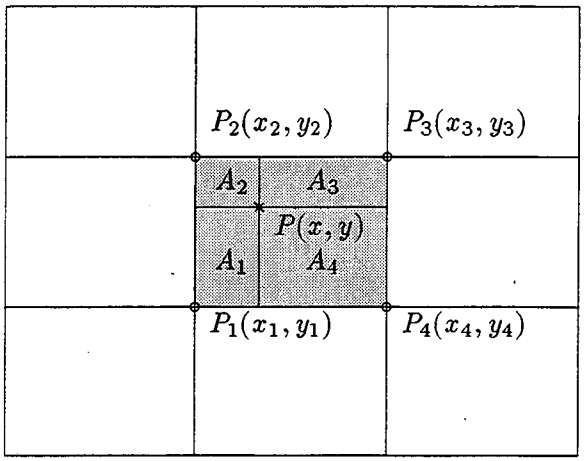

Figure 6.2: Interpolation stencil of a lattice grid.

Similarly, T_2 in equation (6.7) can be expressed as

$$T_2 = \frac{1}{8\pi}\int_0^L dx \int_0^L dx' \int_{R^4} dydzdy'dz' \frac{1}{\sqrt{(x' - \frac{L}{2})^2 + (y' - y)^2 + (z' - z)^2}} \omega(\mathbf{x}) \cdot \omega(\mathbf{x}'). \tag{6.17}$$

When $x' = \frac{L}{2}, y' = y, z' = z$, singularity occurs. Unfortunately, due to the presence of the term $(x' - \frac{L}{2})^2$, there is no scaling property as shown in equation (2.24).

Define

$$E_i = \frac{1}{8\pi}\int_{x_i}^{x_{i+1}} dx \int_{-\sigma}^{\sigma} dy \int_{-\sqrt{\sigma^2-y^2}}^{\sqrt{\sigma^2-y^2}} dz \int_{x_i}^{x_{i+1}} dx' \int_{-\sigma}^{\sigma} dy' \int_{-\sqrt{\sigma^2-y'^2}}^{\sqrt{\sigma^2-y'^2}} dz' \frac{\omega(\mathbf{x}) \cdot \omega(\mathbf{x}')}{\sqrt{(x' - \frac{L}{2})^2 + (y' - y)^2 + (z' - z)^2}} \tag{6.18}$$

then

$$T_2 = \sum E_i \tag{6.19}$$

where the sum is over all segments on all filaments. (6.18) is a six-fold integral which can be approximated by numerical integration. Ricardson's extrapolation can be employed to generate results of high accuracy. If I_h approximates (6.18) with step size h and error $O(h^2)$, then $\frac{16Q_2-Q_1}{15}$ approximates (6.18) with error $O(h^6)$ where

$$Q_1 = \frac{4I_{h/2} - I_h}{3}, \tag{6.20}$$

$$Q_2 = \frac{4I_{h/4} - I_{h/2}}{3}. \tag{6.21}$$

Finally, the approximation of T_3 in expression (6.7) is simple:

$$T_3 = -\frac{1}{8\pi L}\sum_i \sum_j \Gamma_i \Gamma_j \delta \mathbf{l}_i \cdot \mathbf{l}_j. \tag{6.22}$$

6.3 Numerical Experiments

In order to study the model problem, we will use several vortex filaments, each of which initially having the shape of Kelvin waves. To satisfy the boundary conditions, we extend the vortex filaments between the planes by the method of images. As in section 5.3.1, the induced velocity by the vortex filaments at a point $\mathbf{x}$ can be written as

$$\mathbf{u}(\mathbf{x}) = \sum_{i=1}^{N}\sum_{j=1}^{n_i}(\mathbf{u}_1^i(\mathbf{x}) + \mathbf{u}_2^i(\mathbf{x})) \tag{6.23}$$

where $\mathbf{u}_1^i$ and $\mathbf{u}_2^i$ are respectively the contributions of the j-th element on the i-th vortex filament and its image system, which are given in (5.34) and (5.35) with $\chi^c = (x_o, y_o, z_o)$ representing the center of the j-th element on the i-th vortex filament.

We test the codes by choosing initial data as a set of straight vortex lines with $\sigma = 0.1$. The line remains a straight line, which is consistent with physical intuition.

Now we simulate the model problem by choosing $\sigma = 0.1$, $h = 0.4\sigma$, $C = 0.5h$ and $a_0/\lambda = 0.04$. The calculation starts with $N = 7$ and $n_i = 200$ for $1 \leq n_i \leq N$. The computation is terminated if there is a filament with more than 1000 segments. The fourth-order core function (6.3) is used in our computation.

Figure 6.3 shows perspective views of the vortex depicted at time $t = 0.0$, 0.4216, 0.8198, 1.2034, 1.5787 and 1.9189. Violent stretching happens very quickly.

Figure 6.4 and Figure 6.5 depict two views of the same vortex at time $t = 0.0$, 0.4216, 0.8198, 1.2034, 1.5787 and 1.9189. These views are generated by projecting the vortex lines on the xy-plane and yz-plane. One can see that the cross-section is no longer unchanged.

To obtain an accurate measure for the evolution of the vortex, the computed energy, arc length, and total number of segments are examined in Figure 6.6.

To study the dynamic behavior, we apply the Fourier transform to the filament which is the centerline at $t = 0$ and we plot the evolution of the amplitudes of modes $n =$ 8, 9, 10 and 11 in Figure 6.7 and Figure 6.8 with different initial data $a_0/\lambda = 0.02$, 0.04, 0.06, 0.08. These results show that classical vortex does not present the same dynamical phenomena as the superfluid vortex. Instead, classical vortex seems to present some kind of chaotic behaviors. Our numerical experiments indicate that thick vortices with variable cross-section behave differently from thin vortices with constant cross-section.

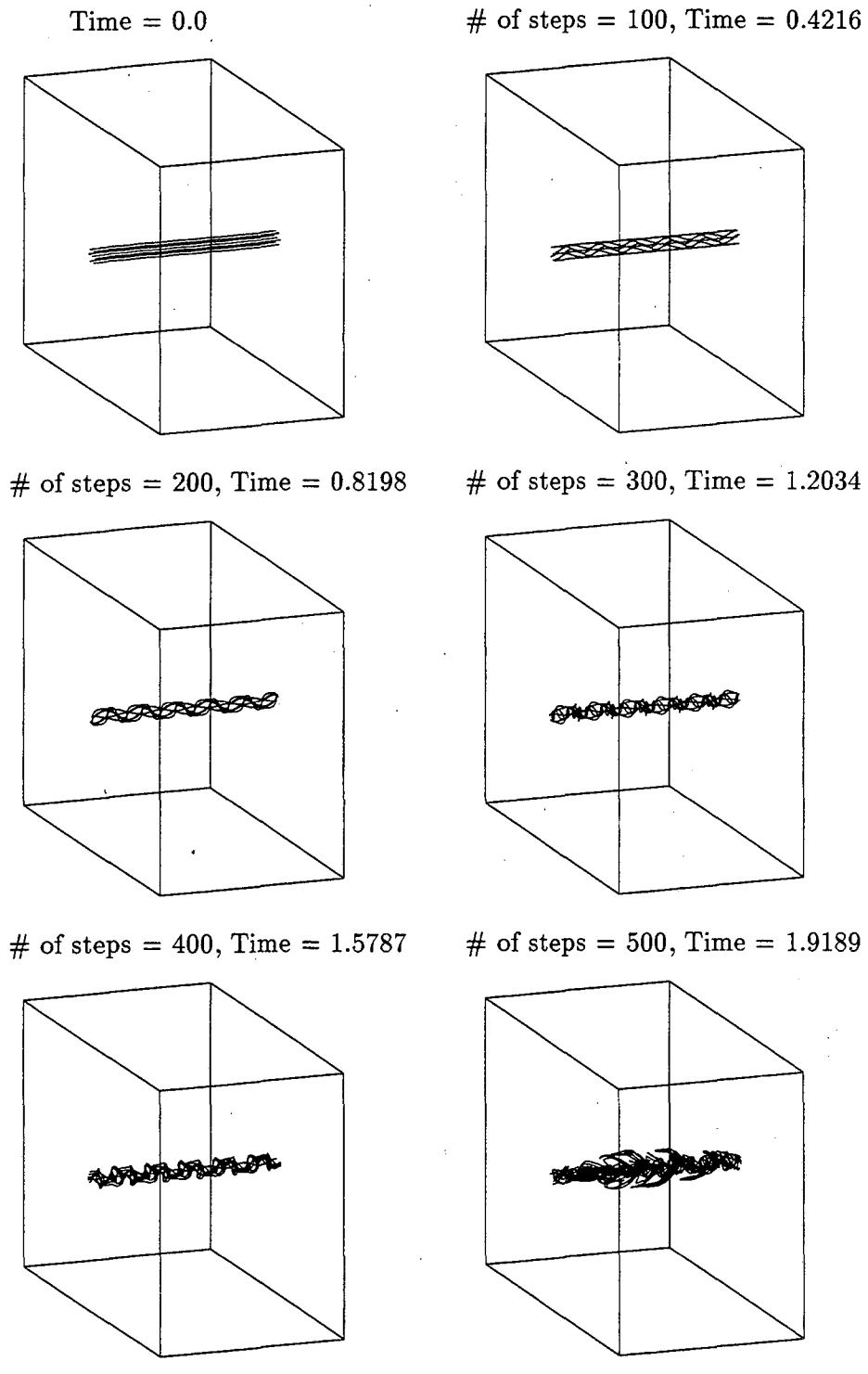

Figure 6.3: Perspective views of the vortex depicted at time = 0.0, 0.4216, 0.8198, 1.2034, 1.5787 and 1.9189. The results are obtained with $a_0/\lambda = 0.04$, $N = 7$, and $n_i = 200$ ($i = 1, ..., N$) at time = 0.

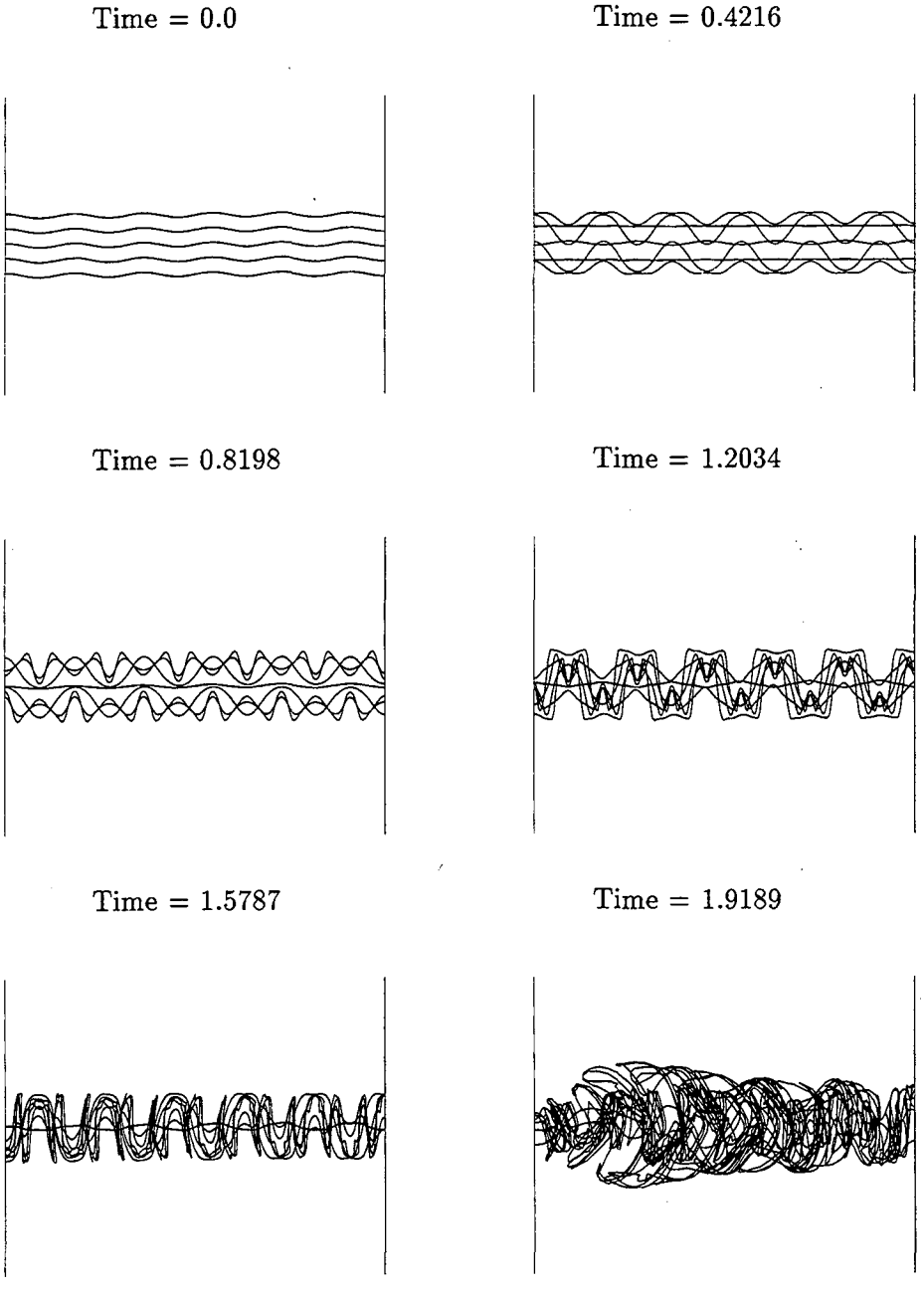

Figure 6.4: The form of the vortex of Figure 6.3. The plots are obtained by projecting the vortex on the xy-plane.

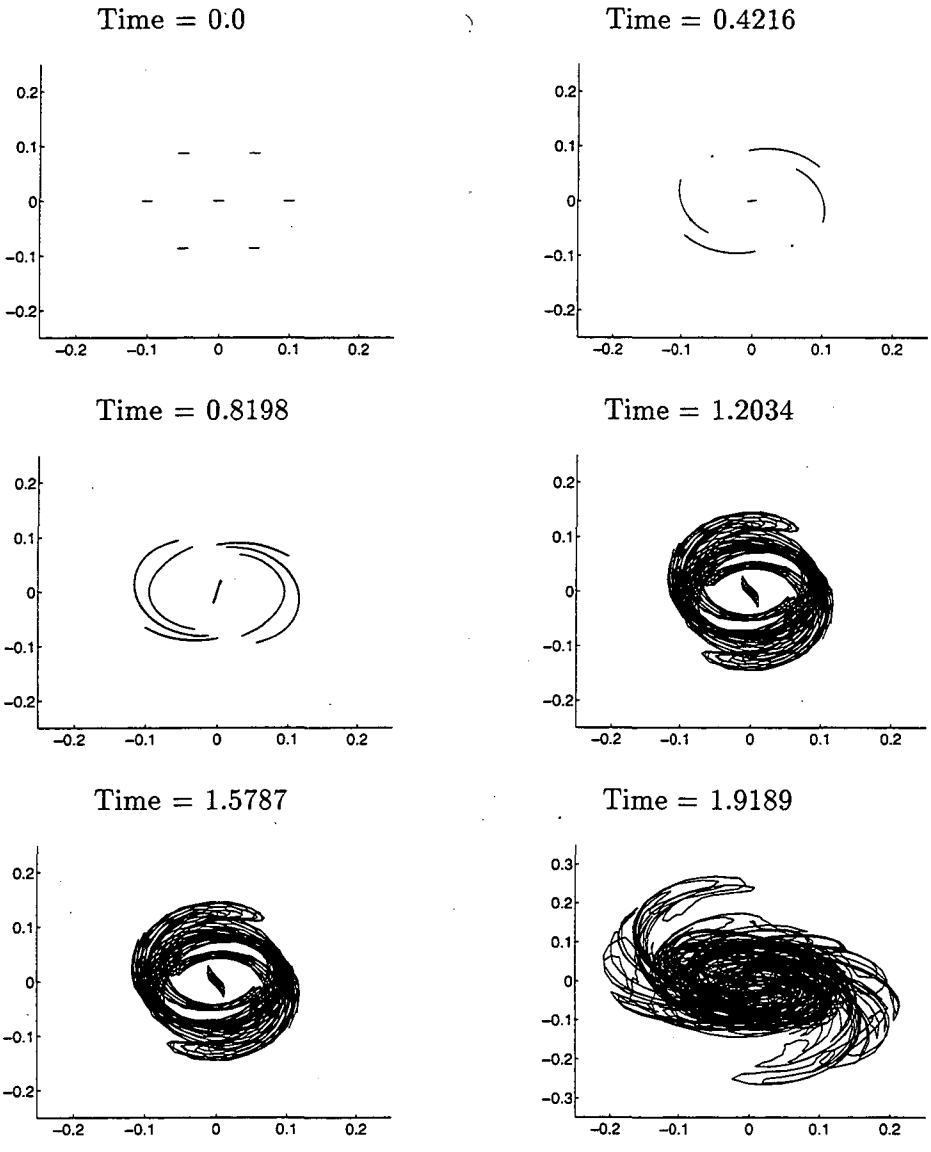

Figure 6.5: The form of the vortex of Figure 6.3. The plots are obtained by projecting the vortex on the yz-plane.

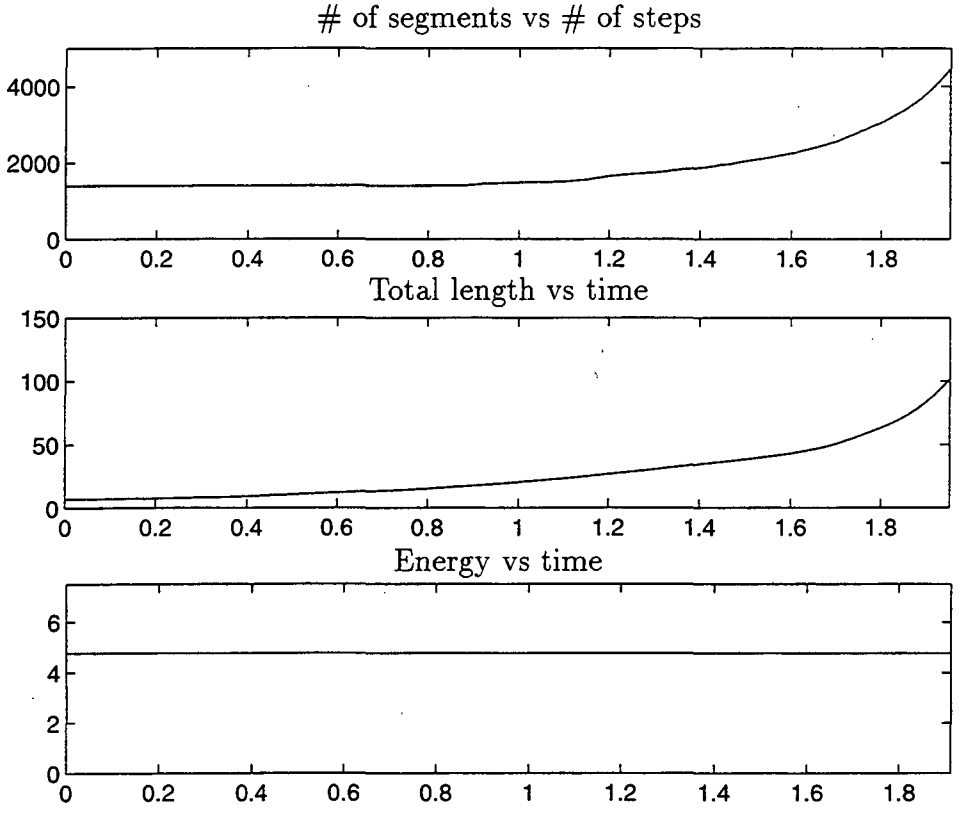

Figure 6.6: Calculation of the vortex method: $a_0/\lambda = 0.04$.

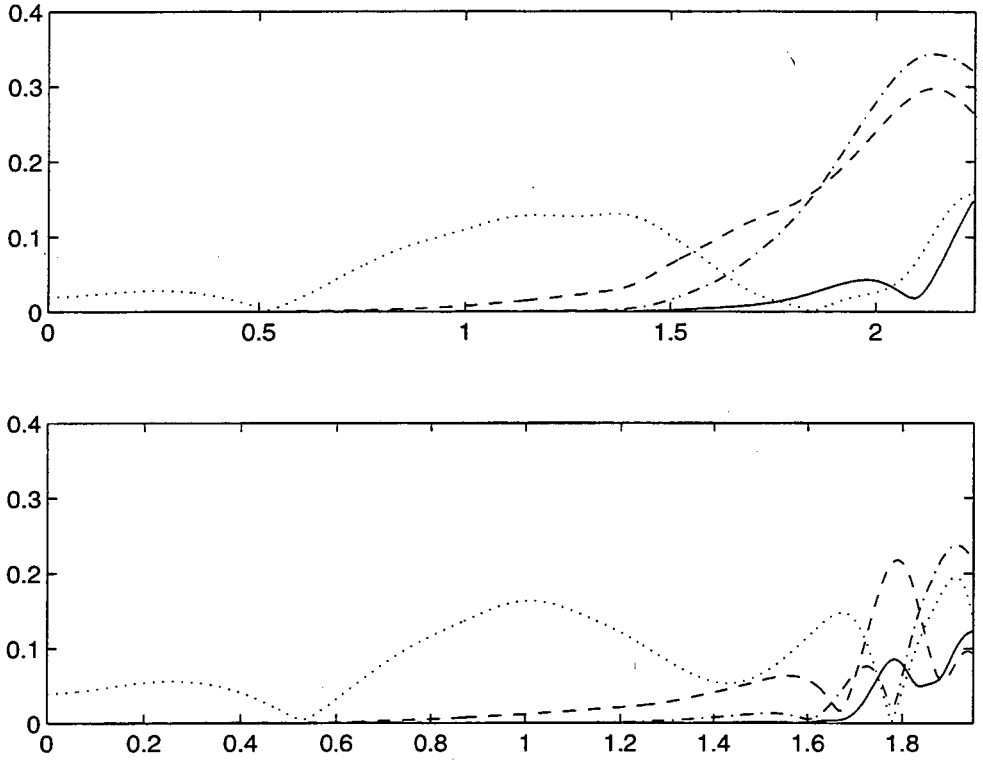

Figure 6.7: Dynamic behavior by the vortex filament method with $a_0/\lambda = 0.02$ (top) and $a_0/\lambda = 0.04$ (bottom). Dotted curve denotes the amplitude of mode $n = 11$, dashed curve $n = 10$, dashdot curve $n = 9$, and solid curve $n = 8$.

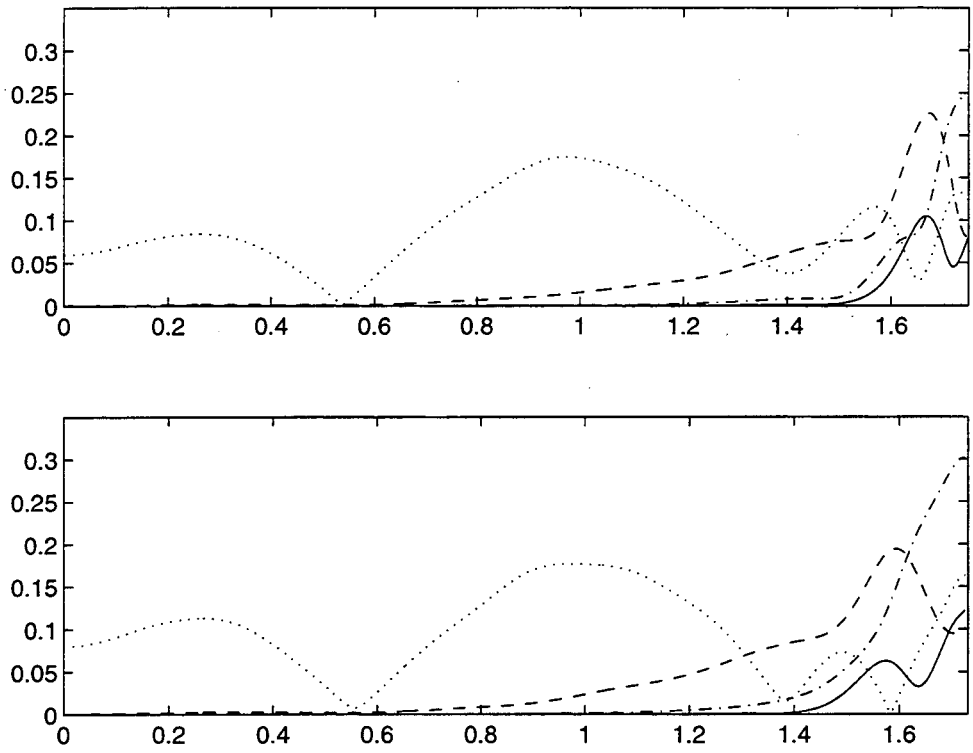

Figure 6.8: Dynamic behavior by the vortex filament method with $a_0/\lambda = 0.06$ (top) and $a_0/\lambda = 0.08$ (bottom). Dotted curve: $n = 11$; Dashed curve: $n = 10$; Dashdot curve: $n = 9$; Solid curve: $n = 8$.

Chapter 7

Conclusions

We have used three different methods, namely the self-induction equation, the Klein-Majda equation, and the Klein-Knio equation, to study the sideband instability of Kelvin waves in superfluid helium. In this model problem, we assume that the thin vortex filament has constant cross-section.

Our numerical simulations reveal that all those methods yield qualitatively similar results. For our model problem, the self-induction equation, the Klein-Majda equation, and the Klein-Knio equation all present stable, recurrent, and chaotic phenomena, corresponding to different ratios of the amplitude of the main wave and its wavelength. The vortex filament whose motion is described by the self-induction equation, the Klein-Majda equation or the Klein-Knio equation evolves smoothly and the total arc length is almost conserved. Furthermore, hairpin structures are not formed during the vortex filament evolution .

The stability region of the Klein-Majda equation is closely related to the core size of the vortex filament. When the core size is larger than a critical value, the Klein-Majda equation always gives a stable solution. When the core size decreases below the critical value, the stability region of the Klein-Majda equation is smaller than that of the self-induction equation. When the core size is further decreased, the stability region of the Klein-Majda equation coincides with the stability region of the self-induction equation. For the model problem, the stability region of the Klein-Majda equation is smaller than that of the self-induction equation.

The stability region of the Klein-Knio equation also depends on the core size of the vortex filament. The bigger the core size, the larger is the stability region. We further find that for the model problem, the Klein-Knio equation has a larger stability region than that

of the self-induction equation. Hence, among our three methods for the model problem, the Klein-Knio equation gives the largest stability region, while the Klein-Majda equation has the smallest stability region.

We also carried out the computations for thicker cores with variable cross-section. A Biot-Savart model was employed. Only chaotic phenomena were observed for sideband perturbations.

Our calculations using the self-induction equation and the Klein-Majda equation are in good agreement with the results of the linear stability theory. Our numerical results imply that thick vortices with variable cross-section behave quite differently from thin vortices with constant cross-section. The thickness of the vortex core might play an important role in the difference in dynamical behavior between superfluid vortices and classical vortices.

If the self-induction equation, the Klein-Majda equation, and the Klein-Knio equation are used to describe superfluid turbulence [37], [95], [17], then the physical assumption that there is no vortex folding on small scale has been implicitly made. Our numerical simulations suggest that this may be a reasonable conclusion for a single filament, but is for the moment an additional assumption for a tangle of filaments. Deeper understanding remains to be found.

The assumption that a tangle of superfluid vortex filaments might not fold on small scales agrees well with the statistical theory of three-dimensional vortex motion: According to the equilibrium theory presented in Chapter 2, the rate of change of vortex length per unit volume L is connected with the rate of change of the temperature T. Unlike in fluid mechanics where a classical fluid has a self-adjusting temperature T, a superfluid has a fixed temperature T. Therefore L is a finite constant and wild folding is prohibited for superfluid vortices.

The differences between classical and superfluid vortex dynamics have been highlighted by Buttke [16], and we have verified them. At this point we do not know whether slender vortex theory or classical vortex theory is a better way to describe superfluid vortex motion. It is well-known from the convergence theory of vortex method [49] that the discretization of the circulation is not significant in the dynamics. This may imply that the slenderness of superfluid vortices is more important in accounting for their non-classical dynamics than the quantization of circulation.

Bibliography

[1] D. J. Adams and G. S. Dubey. Taming the Ewald sum in the computer simulation of charged systems. *Journal of Computational Physics*, 72:156–176, 1987.

[2] J. Akao. *Phase transitions and connectivity in three-dimensional vortex equilibria.* PhD thesis, UC Berkeley, 1994.

[3] J. Akao. Scaling laws for fractal objects, 1994, Manuscript.

[4] A. S. Almgren, T. Buttke, and P. Colella. A fast adaptive vortex method in three dimensions. *Journal of Computational Physics*, 113:177–200, 1994.

[5] R. J. Arms and F. R. Hama. Localized-induction concept on a curved vortex and motion of an elliptic vortex ring. *Physics of Fluids*, 8:553–559, 1965.

[6] K. R. Atkins. *Liquid helium.* Cambridge Unversity Press, 1959.

[7] K. R. Atkins. Third and fourth sound in liquid helium II. *Physical Review*, 113(4):962–965, 1959.

[8] C. F. Barenghi, R. J. Donnelly, and W. F. Vinen. Friction on quantized vortices in helium II. A review. *Journal of Low Temperature Physics*, 52:189–247, 1983.

[9] G. K. Batchelor. *An Introduction to Fluid Dynamics.* Cambridge University Press, 1967.

[10] J. T. Beale and A. Majda. Vortex methods I: Convergence in three dimensions. *Mathematics of Computation*, 39:1–27, 1982.

[11] J. T. Beale and A. Majda. Vortex methods II: High order accuracy in two and three dimensions. *Mathematics of Computation*, 39:29–52, 1982.

[12] J. T. Beale and A. Majda. High order accurate vortex methods with explicit velocity kernals. *Journal of Computational Physics*, 58:188–208, 1985.

[13] J. B. Bell and D. L. Marcus. Vorticity intensification and the transition to turbulence in the three-dimensional Euler equations. *Communications in Mathematical Physics*, 147:371–394, 1992.

[14] T. B. Benjamin and J. E. Feir. The disintegration of wave trains on deep water. *Journal of Fluid Mechanics*, 27:417–430, 1967.

[15] R. Betchov. On the curvature and torsion of an isolated vortex filament. *Journal of Fluid Mechanics*, 22:471–479, 1965.

[16] T. F. Buttke. *A numerical study of superfluid turbulence in the self-induction approximation.* PhD thesis, UC Berkeley, 1986.

[17] T. F. Buttke. Numerical study of superfluid turbulence in the self-induction approximation. *Journal of Computational Physics*, 76:301–326, 1988.

[18] T. F. Buttke. Turbulence and vortices in superfluid helium. In K. E. Gustafson and J. A. Sethian, editors, *Vortex Methods and Vortex Motion.* SIAM, 1991.

[19] A. J. Callegari and L. Ting. Motion of a curved vortex filament with decaying vortical core and axial velocity. *SIAM Journal of Applied Mathematics*, 35:148–175, 1978.

[20] E. A. Caponi, P. G. Saffman, and H. C. Yuen. Instability and confined chaos in a nonlinear dispersive wave system. *Phys. Fluids*, 25:2159–2166, 1982.

[21] A. J. Chorin. The evolution of a turbulent vortex. *Communications in Mathematical Physics*, 83:517–535, 1982.

[22] A. J. Chorin. Turbulence and vortex stretching on a lattice. *Communications on Pure and Applied Mathematics*, XXXIX:S47–S65, 1986.

[23] A. J. Chorin. Scaling laws in the vortex lattice model of turbulence. *Communications in Mathematical Physics*, 114:167–176, 1988.

[24] A. J. Chorin. Hairpin removal in vortex interactions. *Journal of Computational Physics*, 91:1–21, 1990.

[25] A. J. Chorin. Equilibrium statistics of a vortex filament with applications. *Communications in Mathematical Physics*, 141:619–631, 1991.

[26] A. J. Chorin. Vortices, turbulence and statistical mechanics. In K. E. Gustafson and J. A. Sethian, editors, *Vortex Methods and Vortex Motion*. SIAM, 1991.

[27] A. J. Chorin. Hairpin removal in vortex interactions II. *Journal of Computational Physics*, 107:1–9, 1993.

[28] A. J. Chorin. Vortex methods, 1993. Les Houches Summer School of Theoretical Physics.

[29] A. J. Chorin. *Vorticity and Turbulence*. Springer, 1993.

[30] A. J. Chorin. Vortex phase transitions in 2.5 dimensions. *Journal of Statistical Physics*, 76:835–856, 1994.

[31] A. J. Chorin and J. H. Akao. Vortex equilibria in turbulence theory and quantum analogues. *Physica D*, 52:403–414, 1991.

[32] A. J. Chorin and O. Hald. Analysis of Kosterlitz-Thouless transition models, 1995. Manuscript, Dept. of Math., UC Berkeley.

[33] A. J. Chorin and O. Hald. Vortex renormalization in three space dimensions. *Physical Review B*, 51(17):11969–11972, 1995.

[34] A. J. Chorin, T. Hughes, M. McCracken, and J. Marsden. Product formulas and numerical algorithms. *Communications on Pure and Applied Mathematics*, 31:205–256, 1978.

[35] A. J. Chorin and J. E. Marsden. *A Mathematical Introduction to Fluid Mechanics*. Springer, 1979.

[36] E. R. Dobbs. Superfluid helium three. *Contemporary Physics*, 24:389–413, 1983.

[37] R. J. Donnelly. *Quantized Vortices in Helium II*. Cambridge University Press, 1991.

[38] R. J. Donnelly. Quantized vortices and turbulence in helium II. *Annual Review of Fluid Mechanics*, 25:325–371, 1993.

[39] J. Epiney. 3D XY model near criticality, 1990. Diploma thesis, ETH, Zurich.

[40] P. P. Ewald. Ewald summation. *Ann. Physik*, 64:253–371, 1921.

[41] E. Fermi, S. Ulam, and J. Pasta. Studies of non linear problems. In E. Segré, editor, *Collected papers of Enrico Fermi II.* University of Chicago, 1965.

[42] R. P. Feynman. Application of quantum mechanics to liquid helium. In C. J. Gorter, editor, *Progress in low temperature physics.* North Holland, Amsterdam, 1955.

[43] V. L. Ginzburg and L. P. Pitaevskii. On the theory of superfluidity. *Soviet Physics JETP*, 34(7)(5):858–861, 1958.

[44] W. I. Glaberson and M. Steingart. Temperature dependence of the vortex-core parameter in he II. *Physical Review Letters*, 26:1423–1425, 1971.

[45] W. I. Glaberson, D. M. Strayer, and R. J. Donnelly. Model for the core of a quantized vortex line in helium II. *Physical Review Letters*, 21:1740–1744, 1968.

[46] R. Grauer and T. Sideris. Numerical computation of 3D incompressible ideal fluids with swirl. *Physical Review Letters*, 67(25):3511–3514, 1991.

[47] E. Hairer, S. P. Norsett, and G. Wanner. *Solving ordinary differential equations I.* Springer, 1987.

[48] O. H. Hald. Convergence of vortex methods for Euler's equations III. *SIAM Journal on Numerical Analysis*, 24:538–582, 1987.

[49] O. H. Hald. Convergence of vortex methods. In K. E. Gustafson and J. A. Sethian, editors, *Vortex Methods and Vortex Motion.* SIAM, 1991.

[50] H. E. Hall and W. F. Vinen. The rotation of liquid helium II **I.** Experiments on the propagation of second sound in uniformly rotating helium II. *Proceedings of The Royal Society of London, A*, 238:204–214, 1956.

[51] H. E. Hall and W. F. Vinen. The rotation of liquid helium II **II.** the theory of mutual friction in uniformly rotating helium II. *Proceedings of The Royal Society of London, A*, 238:215–234, 1956.

[52] H. Hasimoto. A soliton on a vortex filament. *Journal of Fluid Mechanics*, 51:477–485, 1972.

[53] J. Heiserman, J. P. Hulin, J. Maynard, and I. Rudnick. Precision sound-velocity measurements in helium II. *Physical Review B*, 14:3862–3867, 1976.

[54] E. Infeld and G. Rowlands. *Nonlinear waves,solitons and chaos.* Cambridge University Press, 1990.

[55] A. Van Itterberk, G. Forrez, and M. Teirlinck. Measurements on the velocity of ultrasonic waves in liquid helium. *Physica*, 23:905–906, 1957.

[56] E. A. Jackson. *Perspectives of nonlinear dynamics.* Cambridge University Press, 1989.

[57] C. Kittel. *Introduction to solid state physics.* Wiley, New York, seond edition, 1956. Appendix A.

[58] R. Klein and O. M. Knio. Asymptotic vorticity structure and numerical simulation of slender vortex filaments. *Journal of Fluid Mechanics*, 284:275–321, 1995.

[59] R. Klein and A. Majda. Self-stretching of a perturbed vortex filament I: The asymptotic equation for derivation from a straight line. *Physica D*, 49:323–352, 1991.

[60] R. Klein and A. Majda. Self-stretching of perturbed vortex filaments II: Structure of solutions. *Physica D*, 53:267–297, 1991.

[61] R. Klein and A. Majda. An asymptotic theory for the nonlinear instability of antiparallel pairs of vortex filaments. *The Physics of Fluids A*, 5:369–379, 1993.

[62] R. Klein, A. Majda, and R. McLaughlin. Asymptotic equations for the stretching of vortex filaments in a background flow field. *The Physics of Fluids A*, 4:2271–2281, 1992.

[63] O. M. Knio and A. F. Ghoniem. Numerical study of a three-dimensional vortex method. *Journal of Computational Physics*, 86:75–106, 1990.

[64] G. Kohring and R. Shrock. Properties of generalized 3D O(2) model with suppression/enhancement of vortex strings. *Nuclear Physics B*, 288:397–418, 1987.

[65] H. Lamb. *Hydrodynamics.* Dover, 1932.

[66] L. D. Landau. The theory of superfluidity of helium II. *Journal of Physics (Moscow)*, 5:71–90, 1941.

[67] L. D. Landau and E. M. Lifshitz. *Fluid Mechanics*. Pergamon, London, 1959.

[68] A. Leonard. Review Vortex methods for flow simulation. *Journal Of Computational Physics*, 37:289–335, 1980.

[69] A. Leonard. Computing three-dimensional incompressible flows with vortex elements. *Annual Review of Fluid Mechanics*, 17:523–559, 1985.

[70] H. W. Liepmann and G. A. Laguna. Nonlinear interactions in the fluid mechanics of helium II. *Annual Review of Fluid Mechanics*, 16:139–177, 1984.

[71] O. V. Lounasmaa. The superfluid phases of liquid ^{3}He. *Contemporary Physics*, 15:353–374, 1974.

[72] J. Maynard. Determination of the thermodynamics of helium II from sound-velocity data. *Physical Review B*, 14:3868–3891, 1976.

[73] H. K. Moffatt. The degree of knottedness of tangled vortex lines. *Journal of Fluid Mechanics*, 35:117–129, 1969.

[74] H. K. Moffatt. On the existence of localized rotational disturbances which propagates without change of structure in an inviscid fluid. *Journal of Fluid Mechanics*, 173:289–302, 1986.

[75] D. M. Moody and B. Sturtevant. Shock waves in superfluid helium. *Physics of Fluids*, 27:1125–1137, 1984.

[76] John Neu. Vortices and sound, 1995. Preprint.

[77] A. Newell. *Solitons in Mathematics and Physics*. Society for Industrial and Applied Mathematics, 1985.

[78] L. Onsager. Discussione e osservazioni of "The two fluid model for helium II". *Nuovo Cimento Supplement*, 6:249–250, 1949.

[79] D. V. Osborne. The rotation of liquid helium II. *The Proceedings of the Physical Society, A*, 63:909–912, 1950.

[80] V. Peshkov. Determination of the velocity of propagation of the second sound in helium II. *Journal of Physics (Soviet)*, 10:389–398, 1946.

[81] V. P. Peshkov. Second sound in helium II. *Soviet Physics JETP*, 11(3):580–584, 1960.

[82] P. J. Prince and J. R. Dormand. High order embedded Runge-Kutta formulae. *Journal of Computational and Applied Mathematics*, 7:67–75, 1981.

[83] E. G. Puckett. Vortex methods: An introduction and survey of selected research topics. In M. D. Gunzburger and A. A. Nicolaides, editors, *Incompressible Computational Fluid Dynamics Trends and Advances*. Cambridge, 1993.

[84] A. Pumir and E. Siggia. Collapsing solutions to the 3-D Euler equations. *Physics of Fluids A*, 2(2):220–241, 1990.

[85] S. J. Putterman. *Superfluid Hydrodynamics*. North-Holland, Amsterdam, 1974.

[86] A. Qi. *Three dimensional vortex methods for the analysis of wave propagation on vortex filaments*. PhD thesis, UC Berkeley, 1991.

[87] G. Rajagopal and R. J. Needs. An optimized Ewald method for long-ranged potentials. *Journal of Computational Physics*, 115:399–405, 1994.

[88] G. W. Rayfield and F. Reif. Quantized vortex rings in superfluid helium. *Physical Review*, 136(5A):A1194–A1208, 1964.

[89] R. D. Richtmyer and K. W. Morton. *Difference methods for initial value problems*. Interscience Publishers, 1957.

[90] P. H. Roberts and R. J. Donnelly. Superfluid mechanics. *Annual Review of Fluid Mechanics*, 6:179–225, 1974.

[91] P. H. Roberts, R. N. Hills, and R. J. Donnelly. Calculation of the static healing length in helium II. *Physics Letters*, 70A:437–440, 1979.

[92] P. G. Saffman. *Vortex Dynamics*. Cambridge University Press, 1992.

[93] D. C. Samuels. *The sideband instability and recurrence of vortex waves in superfluid helium II*. PhD thesis, University of Oregon, 1990.

[94] D. C. Samuels and R. J. Donnelly. Sideband instability and recurrence of Kelvin waves on vortex core. *Physics Review Letters*, 64:1385–1388, 1990.

[95] K. W. Schwarz. Generation of superfluid turbulence deduced from simple dynamical rules. *Physics Review Letters*, 49:283–285, 1982.

[96] K. W. Schwarz. Three-dimensional vortex dynamics in superfluid ^{4}he : line-line and line-boundary interactions. *Physical Review B*, 31:5782–5804, 1985.

[97] J. A. Sethian. Turbulent combustion in open and closed vessels. *Journal of Computational Physics*, 54:425–456, 1984.

[98] J. A. Sethian. A brief overview of vortex methods. In K. E. Gustafson and J. A. Sethian, editors, *Vortex Methods and Vortex Motion*. SIAM, 1991.

[99] J. A. Sethian and A. F. Ghoniem. Validation study of vortex methods. *Journal of Computational Physics*, 74:283–317, 1988.

[100] R. S. Shapiro and I. Rudnick. Experimental determination of the fourth sound velocity in helium II. *Physical Review*, 137(5A):A1383–A1391, 1965.

[101] S. R. Shenoy. Vortex-loop scaling in the three-dimensional XY ferromagnet. *Physical Review B*, 40:5056–5068, 1989.

[102] E. D. Siggia. Collapse and amplification of a vortex filament. *Physics of Fluids*, 28:794–805, 1985.

[103] J. Strain. Fast potential theory. II. Layer potentials and discrete sums. *Journal of Computational Physics*, 99(2):251–270, 1992.

[104] G. Strang. Accurate partial difference methods I: Linear Cauchy problems. *Archive for rational mechanics and analysis*, 12(5):392–402, 1963.

[105] G. Strang. Accurate partial difference methods II: Non-linear problems. *Numerische Mathematik*, 6:37–46, 1964.

[106] D. J. Struik. *Lectures on classical differential geometry*. Addison-Wesley, 1957.

[107] D. R. Tilley and J. Tilley. *Superfluidity and Superconductivity*. Boston, 1986.

[108] L. Tisza. Transport phenomena in helium II. *Nature*, 141:913–913, 1938.

[109] J. R. Torczynski, D. Gerthsen, and T. Roesgen. Schlieren photography of second sound shock waves in superfluid helium. *Physics of Fluids*, 27:2418–2423, 1984.

[110] W. F. Vinen. Mutual friction in a heat current in liquid helium II: III. Theory of the mutual friction. *Proceedings of The Royal Society of London, A*, 242:493–515, 1957.

[111] W. F. Vinen. The detection of single quanta of circulation in liquid heliumII. *Proceedings of The Royal Society of London, A*, 260:218–236, 1961.

[112] J. C. Wheatley. Experimental properties of superfluid ^{3}He. *Reviews of Modern Physics*, 47(2):415–470, 1975.

[113] S. Widnall. The structure and dynamics of vortex filaments. *Annual Review of Fluid Mechanics*, 8:141–165, 1976.

[114] S. E. Widnall and J. P. Sullivan. On the stability of vortex rings. *Proceedings of the Royal Society of London, A*, 332:335–353, 1973.

[115] J. Wilks. *The properties of liquid and solid helium.* Oxford Unversity Press, 1967.

[116] G. S. Winckelmans and A. Leonard. Contributions to vortex particle methods for the computation of three-dimensional incompressible unsteady flows. *Journal of Computational Physics*, 109:247–273, 1993.

[117] H. C. Yuen and W. E. Ferguson. Relationship between Benjamin-Feir instability and recurrence in the nonlinear Schrödinger equation. *Physics of Fluids*, 21:1275–1278, 1978.

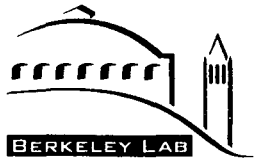

ERNEST ORLANDO LAWRENCE BERKELEY NATIONAL LABORATORY
TECHNICAL AND ELECTRONIC INFORMATION DEPARTMENT
UNIVERSITY OF CALIFORNIA | BERKELEY, CALIFORNIA 94720